Thermodynamic studies of oxygen vacancies in pure and doped SnO_2 surfaces

by

Nima Karimitari

(Under the Direction of Steven P. Lewis)

Abstract

One of the main metal-oxides that has been widely used in gas sensing and catalysis is SnO_2. To better understand the underlying physics behind the sensing mechanism, this study focuses on analysing oxygen vacancies and their determining factor at working sensor conditions. The highlight of this research is in using a combination of two different computational approaches, Monte Carlo (MC) and Density Functional Theory (DFT) to study the morphologies of vacancies at a given temperature and chemical potential of an oxygen reservoir. In brief, a model Hamiltonian is constructed from a set of DFT calculations. Then, once the quality of the parameters are found to be good enough, they are used in Monte Carlo simulations. This methodology is applied to three different scenarios: (101) surface, (110) surface and Pd-doped (101) surface. Investigations on (101) surface not only agrees with earlier studies, but also depicts a finer resolution of vacancy patterns. Applying the same approach to SnO_2 (110), shows novel patterns of vacancies not observed before. In the last part, applying it to the Pd-doped system, successfully shows the role of transition metals in expediting the formation of oxygen vacancies. The results provide a deeper understanding on how transition metals improve the sensing mechanism and how the model Hamiltonian approach has the potential to be used in wide range of interesting surface studies.

Index words: [SnO_2, gas sensing, metal-oxides, oxygen vacancies, dopants, transition metals]

Thermodynamic studies of oxygen vacancies in pure and doped SnO_2 surfaces

by

Nima Karimitari

B.S., Amirkabir University of Technology, Iran, 2015

A Dissertation Submitted to the Graduate Faculty of the

University of Georgia in Partial Fulfillment of the Requirements for the Degree

Doctor of Philosophy

Athens, Georgia

2022

Thermodynamic studies of oxygen vacancies in pure and doped SnO_2 surfaces

by

Nima Karimitari

Major Professor: Steven P. Lewis

Committee: David P. Landau

Tho Nguyen

Electronic Version Approved:

Ron Walcott

Vice Provost for Graduate Education and

Dean of the Graduate School

The University of Georgia

August 2022

Dedication

To my lovely wife, Mona.

Acknowledgments

All the calculations in this study were performed by the computer clusters provided by GACRC of the University of Georgia.

Contents

List of Figures

List of Tables

Chapter 1

Introduction

The structure and composition of metal oxides and their interaction with the environment has been investigated for various different applications. In particular, SnO_2 is among the transparent metal oxides with application in spintronics, gas sensing and catalysis. One of the interesting features of SnO_2 is the dual valency of Sn atom (+2 or +4) which allow the system to be in different charge states. When dealing with the surface termination of SnO_2, depending on the preparation conditions, different oxidization states of Sn are observed. With an emphasis on the gas sensing properties of SnO_2, this study focuses on surface composition of two important surface terminations (110) and (101), proposes a more complete approach to study the oxygen vacancies and provides a deeper understanding of the role oxygen vacancies in the gas sensing applications.

A detailed discussion of the common mechanism of gas sensors based on SnO_2 with discussion of every step is provided in chapter 2. It starts by showing the possible band bending that occurs at the interface between a reducing gas and an n-type gas sensor. The charge is transferred from the surface to the reducing gas leading to ionized molecules on the surface. The discussion follows by a brief history of experimental and theoretical studies that had investigated the defects that facilitate the charge transfer, with more emphasis on the role of oxygen vacancies in SnO_2. In the last part, some examples of previous studies on the role of transition metal dopants in metal oxides are reviewed. The main goal of chapter 2 is

to prepare the reader to understand the importance of oxygen vacancies and challenges in understanding their morphologies and composition in SnO_2.

In chapter 3 and 4, details of theoretical tools that my research utilized in studying the SnO_2 surfaces are discussed in detail. In particular, chapter 3 emphasizes the difficulty of solving the many body problem and how it can simplified to Density Functional Theory (DFT). I tried to highlight the main postulates, importance of Kohn-Sham equations and how it is applied in studying electronic properties. Later, some drawbacks and difficulties in DFT are mentioned. In chapter 4, my attention is on thermodynamic properties with some history of previous methods used in dealing with them. It begins with a discussion on *Ab-initio* Thermodynamics, some history of how it is applied in studying surface stability. Subsequently, the discussion would turn to a popular classical way of dealing with thermodynamic properties, called Monte Carlo simulation, with emphasis on the simplest importance sampling method of Metropolis et al. Lastly, the exact methodology used in this dissertation is discussed in detail. In brief, a model Hamiltonian is constructed from a set of configurations performed at the DFT level, then the model Hamiltonian is considered as an input Hamiltonian for a Monte Carlo simulation at a finite temperature and pressure of a reservoir in the grand canonical ensemble.

In chapter 5, the first part of the results for (101) surface termination of SnO_2 are shown. First, a model Hamiltonian is constructed from a set of DFT calculations. All the configurations considered for this surface are provided in appendix A. Then, the accuracy of the model Hamiltonian is tested by comparing the predicted energy values with the actual DFT values. Subsequently, Monte Carlo simulations are performed for oxygen chemical potentials ranging from -0.7 eV to -1.7 eV at fix temperatures of 400, 500 and 600 kelvin. According to the calculated results, vacancies start to form as rows of vacancies along [010] direction close to -1.15 eV. Then, in a range of chemical potential -1.16 to -1.30 eV they form a 2×1 pattern, where every other rows of vacancies cover the entire (101) surface. Such results are in great agreement with earlier experimental and theoretical studies. Going toward a more oxygen deficient environment, the surface further reduces to a fully reduced surface with no oxygen atom in the outermost layer at around -1.35 eV. To better check the reliability of the model Hamiltonian approach, these

results are compared with *Ab-initio* Thermodynamics for three most stable surface termination. Not only are the transitions the same in both approaches, but one can notice the advantage of the model Hamiltonian approach where one can have a finer resolution of vacancies that form on the surface. It should be mentioned that finite size effects and their influence on the results are also analyzed later in that chapter.

With the success of the model Hamiltonian approach in prediction of vacancies for the (101) surface, it is then applied to the more complicated surface (110) surface termination in chapter 6. As discussed in chapter 2, this surface has two types of oxygen vacancies, bridging and in-plane. Consequently, the model Hamiltonian would become a lot more complicated due to the presence of different types of interactions, in-plane/in-plane, bridging/bridging and bridging/in-plane interactions. Compared to (101) surface, a much larger set of DFT calculations were performed (Appendix B). Then a model Hamiltonian that has up to 16 parameters is fitted to the DFT structural calculations that did not undergo reconstructions. Details of how parameters are selected and what tests have been done are also provided in Appendix C. Performing Monte Carlo simulations with the model Hamiltonian results in surface patterns not observed before. In particular, vacancies tend to form as clusters of vacancies isolated and spread across the entire surface. As one goes toward a more negative chemical potential, these clusters become elongated along [001] direction and eventually cover the entire surface. There are both similarities and noticeable differences with previous *Ab-initio* Thermodynamics studies. For example, every other rows of bridging and in-plane vacancies can be seen to form along [001] direction. However, they first start to form as clusters which were not predicted before. Also, the grain boundary between two different region of the surface results in two new interesting patterns, not predicted in any other studies. The main difficulties in dealing with (110) surface were surface reconstructions at highly reduced surfaces. I discuss the approximation that we employed to ignore the reconstructions which will limit our study to surfaces which have vacancy concentration of at most 67 %. In reality, surfaces with higher concentration of vacancies are found to be less stable and are not in the scope of the model Hamiltonian approach.

Chapter 7 is about using the same methodology of model Hamiltonian in studying doped surfaces. Specifically, the last part of my research was on (101) doped with Palladium (Pd) and how vacancies are influenced by the presence of Pd. The reason for the selection of (101) surface was because oxygen vacancies are less costly to form on (101) and in presence of Pd can push the partial pressure of the reservoir to the sensor working conditions. It should be emphasized that some tests were performed on (110) surface termination but all resulted in less interesting response compared to (101). Similar to chapter 5 and 6, a model Hamiltonian is constructed from a set of DFT calculations. The difference here is that Pd concentration is also very important and can change based on the size of the surface cell. Given that most experimental studies have low concentration Pd dopants, only a single tin atom is substituted with a Pd for 3×2, 4×2 and 3×3 surface cells. In all our DFT calculations, the calculations show that Pd can only influence vacancies within a certain radius of it. Therefore, to account for regions of the surface that Pd atoms are not present, the model Hamiltonian is constructed from both the pure and doped surface calculations. In other words, if a vacancy is formed far from any Pd atom, it behaves as it would form on a pure surface SnO_2. Monte Carlo simulations show that vacancies are created in islands surrounding the Pd atoms. These islands grow larger in size as one goes toward more oxygen deficient environment. Detailed discussion is provided for different Pd concentration with comparisons between the morphologies of vacancies. At the end, further tests on the reliability of the results were made based on random fluctuations of the parameters and influence of the size of the system of the final outcome.

Chapter 8 of this dissertation presents a detailed discussion on the main advantages and disadvantages of using the Model Hamiltonian approach compared to the *Ab-initio* Thermodynamics. This is followed by a step-by-step recipe on how to construct a model Hamiltonian in studying other surfaces or structures and possible limitations and difficulties in doing so.

Chapter 2

Background information and previous studies

2.1 Tin-oxide and gas sensing

Tin-oxide (SnO_2) also known as Cassiterite, is a well-known semiconductor metal oxide (SMO) which has been widely used in industry for gas sensing [1]–[4], transparent semiconductor [5]–[8], and catalytic supporting materials [9]–[14]. With regard to gas sensing, SMOs can be divided into two groups based on the operating temperature, and their corresponding sensing mechanism: (1) materials that follow the conductance effects at the surface and operates at lower temperatures (600 K- 800 K), and (2) materials that follow the bulk conductance effects and operate at higher temperatures (> 900 K). SnO_2 belong to the former group, where the the change in conductance is believed to be due to the formation and removal of surface oxygen atoms [1].

The sensing mechanism at the surface level is determined by the charge transfer between the surface and the target gas, and eventually a change in the conductivity or resistivity of the SMO. Such sensors are also known as "resistive-type" sensors. There are many studies that have tried to analyze each step of the sensing process, but in general the exact mechanism is still controversial. The most commonly used mechanism is what is known as "ionosorption model". This model considers certain chemical reactions

between an adsorbed oxygen molecule and the "target" gas as the sole player in sensing. In particular, the first step of such mechanism is the adsorption of gaseous oxygen molecule on the surface. Given that O_2 is a reducing gas, when exposed to an n-type semiconductor, it accepts electrons from the surface of the semiconductor, as depicted in Fig. 2.1. The reason for this behavior lies in the fact that the Fermi level (E_f) in n-type SMOs, including SnO_2, is at a higher energy level compared to O_2. Therefore, to reach equilibrium, the electrons that excited to conduction bands at the working condition of the sensor, transfer to the adsorbed O_2, making it negatively charged and cause an upward band-bending. The region where the band-bending occurs (Δ_{air}) is refereed to as a "depletion" or "space-charge" region due to loss of electrons to the O_2 molecules. The upward band-bending causes the electrons to face upward-potential barrier in a given circuit, leading to a lower conductivity or higher resistivity. In the second step, O_2^- is believed to dissociate into atomic oxygen species O^-. This step is believed to occur at elevated temperatures (500-700 K) that can overcome the kinetic barrier of the O_2^-. This entire process can also be seen in Fig. 2.2, where nanostructures with depletion regions are depicted. The horizontal arrow shows the direction of current or "percolation path". One can clearly notice the band-bending caused by the adsorption and dissociation of O_2 molecules on the surface. Upon exposure to a possible target gas (CO), the charge on the oxygen atom is returned to the nanostructures, leading to smaller band bending and consequently, shorter depletion region. The change in the barrier affect the conductivity of the system and, therefore, can be attributed as the determining sign of the sensing toward a target gas.

While there are some experimental studies using electron paramagnetic resonance (EPR) [16]–[18] that confirm the existence of O^-, these are a bit controversial due to being too unstable at the surface and their fast reaction with any target gas. Most notably, Gurlo [4] argued that most evidences that consider the presence of O^- have high experimental uncertainty, making them unreliable. The third step of the ionosorption model, involves the reaction of highly active and sensitive O^- with a reducing target gas, including CO, NO, SO, etc. [19]–[23]. Such a reaction will lead to a less hazardous gaseous, including CO_2, NO_2, SO_2, desorption of these gaseous and eventually return of the excess negative charge back to

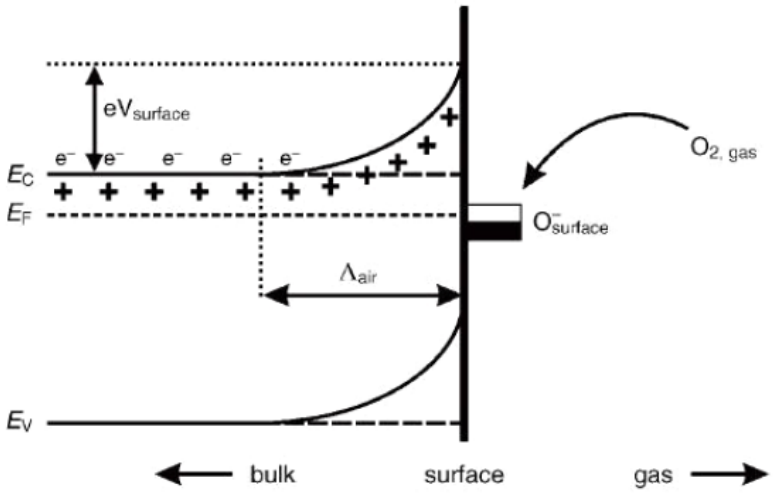

Figure 2.1: The band-bending at the interface of the SnO_2 and molecular O_2. The fermi level is set at an arbitrary value close to conduction band to show the n-type behavior of the system. [15]

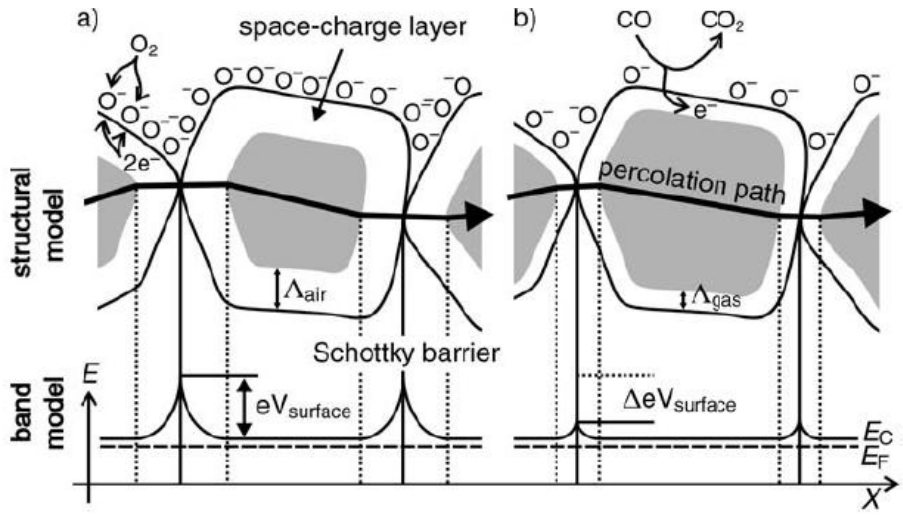

Figure 2.2: The depletion region in presence of the charged atomic O^- .(a) Charge transfer from the nanostructure to the atomic O and high potential barrier. (b) Formation of CO_2 molecule after the interaction of gaseous CO with the adsorbed O. Charge is transferred back to the nanostructure.[15]

the SMO surface. Therefore, during the sensing of the target gas, the conductivity increases and thereby, the system senses the target gas in the environment.

2.2 Role of defects

With regard to aforementioned mechanism, there have been numerous studies to investigate each of the steps mentioned above in SnO_2. One of the fundamental questions that became controversial was the source of the n-type behavior seen in SnO_2. [24] Earlier theoretical studies based on density functional theory, predicted that oxygen vacancies introduce the energy levels close to the conduction band, making the system an n-type semiconductor. However, with the advance of psuedopotentials and improvements made to improve the band-gap problem of DFT [25], it was found that oxygen vacancies are mostly at deep donor levels [26]. This means that under thermodynamic conditions of the working sensors, there are not enough excited conduction electrons to mediate the sensing, as was discussed step-by-step in the previous section. Later studies showed that hydrogen at interstitial sites or substituted for the oxygen atoms of the lattice are the main source of n-type behavior and completely ruled out the role of oxygen vacancies. However, the final chapter of such analysis was in 2011, [27] when it was shown that both oxygen vacancies and hydrogen interstitials need to be considered for the source of n-type character of SnO_2.

Visiting back to the ionosorption mechanism, the first step consisted of adsorption of O_2 on the surface of SnO_2. There are several theoretical studies that tried to consider simple cases of single-terminated surfaces of SnO_2 and find the relaxed geometry of the adsorbed molecule on the surface. It is found that adsorption of the molecule is largely endothermic. In particular, Oviedo [28] placed the molecule in different orientations, as shown in Fig. 2.3, found that all cases are endothermic. Therefore, the conclusion of these studies contradicts the prediction of the ionosorption model. Some studies then focused on surfaces with oxygen vacancies as potential candidates for molecular O_2 adsorption [29], [30]. There are several major problems with this assumption: (1) The reduced surface with oxygen vacancies needs to be carefully examined before studying the adsorption of molecules. In particular, vacancies can have

different patterns depending on the thermodynamic conditions. However, most studies consider the simplest possible configuration, a fully reduced surface, to lower computational cost. Such scenarios, as it is shown in the present study, are nonphysical and can hardly describe any physics of the surface used as a gas sensor. (2) One needs to be able to justify whether oxygen vacancies are stable or not. In other words, vacancies may get healed in the presence of enough oxygen atoms/molecules in the reservoir. This will question the reliability of the study of oxygen molecule adsorption on the reduced surface that is going to get healed by the molecules in the long term.

In addition to the previously mentioned analysis difficulties, there are several limitations at the theory level which may explain the disagreement. First, the theoretical studies are based on density functional theory, a zero temperature approximation which may neglect any entropic effects of molecular adsorption on the surface. Secondly, all these studies consider a pure oxidized surface with no defects at the surface. In reality, the surfaces of tin-oxide have noticeable defects that can influence the interaction with any adsorbed molecule. On an oxidized surface, the tin atoms are at their highest oxidization level and cannot create strong enough bonds to any target gas. Therefore, defects including oxygen vacancies, tin interstitials, or any transition metal dopants may play an important role in this process. Thirdly, one should always consider the fact that SnO_2 sensors are built from nanocrystalline particles of SnO_2, so the consideration of the pure surface termination at the DFT level is far from the exact geometry of the structure in the gas sensors. However, DFT calculations done at the most stable surface terminations of the SnO_2 can still be used to provide mostly qualitative results in agreement with the experimental studies.

2.3 Oxygen vacancies

We first briefly mention the previous studies on the simple (101) surface then move on to the more stable but complicated (110) surface. Batzill *et al* [31] prepared a reduced (101) surface by sputtering and annealing in the range of 600-1000 K and found a 1×1 pattern. Depending on the experimental conditions, they were able to detect 2×1 patterns in rare occasions which then transformed to 1×1 upon vacuum annealing. In the stoichiometric phase, all tin atoms share electrons with 5 oxygen atoms and are in +4 charge state,

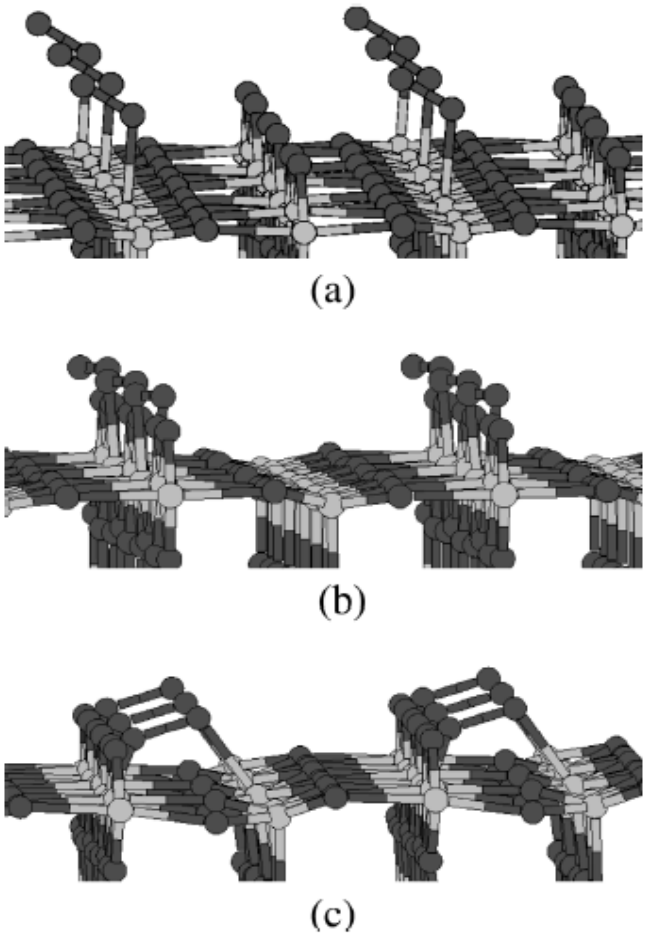

Figure 2.3: Different possible orientations of the oxygen molecules on the SnO_2(110) surface termination. The most stable scenarios is (c) which is still highly endothermic. [28]

but as the system reduces and loses oxygen atoms, they end sharing electrons with 3 oxygen atoms and are in +2 charge state. This is a direct consequence of transformation of SnO_2 to SnO at the surface. The 1×1 case was confirmed to be a fully reduced surface with all bridging oxygen atoms removed, while the 2×1 has every other row of them removed. In the latter scenario, half of the tin atoms are in +2 and the others in +4 state, while in the former case, all tin atoms are in +2 charge state . First-principles calculations using *Ab-initio* Thermodynamics for (101) surface predicted both 2×1 and 1×1 surfaces to be stable in a specific range of oxygen chemical potential, in good agreement with the experimental studies. Interestingly, the 2×1 surface was the more stable phase in a narrow range of chemical potential (0.3 eV), explaining the difficulty in preparing it experimentally.

For the (110) surface, depending on the preparation conditions and oxidation history, a number of different structures were found . A fully oxidized surface was achieved after exposing it to at least 1 torr oxygen partial pressure at 700 K. Cox *et al* [32] were the first to study the surface by using low energy He^+ ion scattering spectroscopy (LEID). Their measurements on the thoroughly oxidized samples show transition in the range of 440-520 K. They suggested that bridging oxygen atoms are the first to leave the surface, followed by in-plane oxygen atoms at higher temperatures. These results were later confirmed by [33] where they also observed same the range of temperatures for a possible transition. However, qualitative low energy electron diffraction (LEED) studies found no transition and only a 1×1 surface unit-cell. The surface retains the 1×1 pattern up to annealing close to 900 K. On the other hand, scanning tunneling microscopy (STM) studies exhibited non-flat terraces and some corrugation. In these studies only terraces of nanometers can be observed due to the samples' roughening. This made the 1×1 LEED pattern questionable as to whether it originated from the surface or the sub surface [31]. A 4×1 reconstruction was also formed after ion sputtering and vacuum annealing to 980 K. The origin of this reconstruction was under dispute until the recent work by Merte *et al.* [34] where they confirmed the role of interstitial tin and not in-plane vacancies in the reconstruction.

Regarding the theoretical works, Oveido *et al.* [35] were the first to study the vacancy formation energy for different surface configurations of the (110) surface using first-principle calculations. They calculated

the formation energy of bridging and in-plane vacancies, separately. At low concentration of vacancies, they found the bridging oxygen vacancies to form at -2.2 eV, about 0.8 eV lower in energy compared to in-plane vacancies. However, by increasing the concentration of vacancies, the formation energies of in-plane and bridging vacancies became almost the same, indicating the likelihood of simultaneous formation of in-plane and bridging vacancies. Later, Ab-initio Thermodynamics [36] studies showed the surface structure under reducing conditions have both bridging and in-plane oxygen vacancies [31], [37]. They found a transition from the stoichiometric surface to a reduced surface at about -2.4 eV oxygen chemical potential. The reduced surface has all bridging oxygen atoms removed, plus every other row of in-plane oxygen. These results shone light on the fact that the flat surface with only bridging oxygen vacancies, which was extensively used as the reduced surface [38]–[40], is not the thermodynamically stable surface. The same study calculated the band structure of the flat surface and found a large dispersion above the bulk valence band maximum (VCM) , a feature that they did not observe experimentally and another clue that the flat surface is not stable.

2.4 Transition metal dopants

There have been many studies on the role of transition metals in the sensing mechanism of the SnO_2. In particular, Ce, Ni, Al, Ru, Pd, Pt, In and Zn have all proven to improve the sensitivity and selectivity of metal oxide gas sensors [41]–[47]. Typically, two main concepts are behind the sensing performance [48]: The electronic mechanism points to the the change in the depletion area surrounding the nanoparticles, as shown earlier in section 1.1. The change in the oxidization state of the transition metal and stronger charge transfer from the dopants to the adsorbed molecules are the backbones of this mechanism. However, the kinetics and temperature dependence of the sensors cannot be solely described by it. Therefore, the second mechanism known as "chemical" argues that the transition metals facilitate the dissociation of oxygen molecules. The atomic products of this process then diffuse to the rest of the surface and heal some of oxygen vacancies of the surface. At the same time, the atomic oxygen is highly unstable and can react with a target gas. The radius to which the molecular atomic products diffuse is called the "spillover

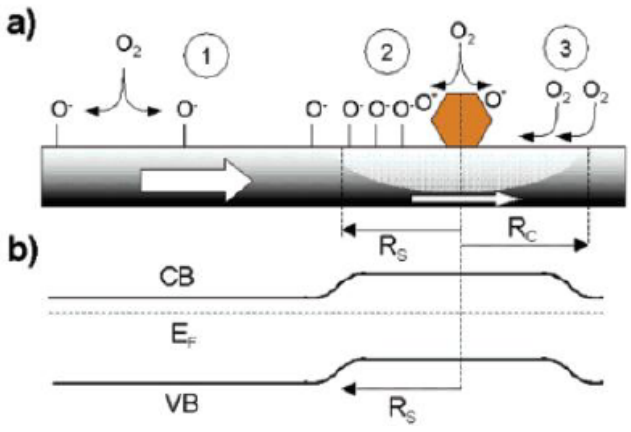

Figure 2.4: Three different mechanisms that can occur at a typical metal-oxide sensor: (a) Dissociation of the molecular oxygen on the pure surface, (b) spillover effect where oxygen molecules are disscoated within an effective radius of R_s (c) Back spillover effect where adsorbed molecules are attracted toward the dopant in a radius of R_c[48].

zone" [14] which can be from 10 nm to μm depending on the preparation of the experimental sample. Similarly, molecules adsorbed on the surface can be attracted to the Pd cluster to within a radius that is called "capture radius". In this case, molecules reside briefly on the surface before diffusing toward the dopants. A qualitative drawing of both mechanisms are illustrated in Fig. 2.4.

Deposition of Pd clusters on SnO_2 nanowires shows an order of magnitude increase in the conductivity of the nanowire when exposed to the target gas as compared to the pure surface. Other experimental studies also confirm that Pt-load tin-oxide has orders of magnitude higher sensitivity toward vapor ethanol up to sub-ppm levels [49]. Similarly, other experimental studies regarding the sensing of CO and O_2 [50] found that small percentages of Pd or Pt dopant can affect the sensitivity by orders of magnitude.

Theoretical studies have also shown that transition metals in interstitial position or substituted for Sn atom can decrease the formation energy of oxygen vacancies and enhance the bonding with reducing gases . In the case of Ru [46], two different sites of surface, 5-fold and 6-fold tin were considered for the substitution of the Ru dopants, where 6-fold site were found to be more stable by 0.4 eV. Adsorption of an oxygen molecule becomes exothermic at -0.61 eV, noticeably different than the endothermic adsorption

of the molecule on the pure surface. Further analysis revealed that 5-fold sites lower the final energy of a possible dissociation of oxygen molecule to peroxide ions. Similar to the previous study, Pt can also be substituted with 5-fold or 6-fold tin atoms [51]. Different surface coverages were considered. Pt prefers to substitute for the 6-fold site. Similarly, Ti and Ru both prefer the high-coordinated Sn atom because of having the same crystalline structure for TiO_2 and RuO_2. Formation energies of oxygen vacancies using *Ab-initio* thermodynamics were analyzed for bridging and in-plane vacancies. Then analysis of CO interaction with the surface was done for two different scenarios, (1) interaction of CO with the lattice oxygen and formation of CO_2, (2) interaction of CO with the adsorbed O_2 molecules and formation of CO_2. In both cases, the adsorption of CO was enhanced by the presence of Pt, with barrier for the dissociation becoming smaller in magnitude compared to the pure surface. Indium is another transition metal that has been used to improve sensing of CO. [44] This study focused on highly doped surface unit-cell with both 5 and 6-coordinated Sn atoms substituted with In atoms. While this study focused on the role of CO oxidization on the surface, the surprising high concentration of In dopants questions the physical interpretation of the energy barrier estimation.

Regarding the Pd atoms, there are several different theoretical studies that aimed to understand the structural changes in the system . In the first work by Maki-Jaskari, [52] the authors considered substitution of Pd with both Sn and O atoms for three surface terminations (110), (101) and (001). As expected, replacing oxygen atoms with Pd resulted in highly deformed surfaces, but less changes were found when substituting with Sn atoms. The authors then found that the most stable surface, in terms of surface energy, is when Pd substitute for the in-plane oxygen atoms. However, such a scenario is highly unrealistic due to significant difference in the oxidization of the atoms with oxygen at -2 and Pd at +4/+3. The study by Tang, [53] followed the same approach most studies followed, which is substitution with either 5-fold or 6-fold tin and only considering the formation of oxygen vacancies in the smallest surface uni-cell (1×1). The latest study in 2015, [54] considered a single Pd atom adsorbed on the (110) surface. They found the most stable configuration of the surface by placing Pd atom at different possible sites. Then it was found that the

adsorption of CO molecule is stable by more than -1.5 eV with the presence of Pd compared to the pure surface.

Chapter 3

First-Principles Calculations

3.1 The many-body problem

In general, a piece of matter is considered to be made of a collection of interacting atoms that have a number of electrons and nuclei. The ensemble of these atoms can be in a solid, liquid or amorphous phase, either homogeneous or heterogeneous (molecules in solution, interfaces, adsorbates on surfaces). In all these scenarios, the total Hamiltonian of the system can be written can be written in terms of kinetic energy ($\hat{T}$), ion-ion interaction ($\hat{V}_{\text{ii}}$), electron-ion interactions ($\hat{V}_{\text{ie}}$), and electron-electron interactions ($\hat{U}_{\text{ee}}$) as following,

$$\hat{\mathscr{H}} = \hat{T} + \hat{V}_{\text{ii}} + \hat{U}_{\text{ee}} + \hat{V}_{\text{ie}} \tag{3.1}$$

With the consideration that there are N electrons and P ions, Eq. 3.1 can be written as,

$$\begin{aligned} \hat{\mathscr{H}} = &- \sum_{I=1}^{P} \frac{\hbar^2}{2M_I} \nabla_I^2 - \sum_{i=1}^{N} \frac{\hbar^2}{2m} \nabla_i^2 + \frac{e^2}{2} \sum_{I=1}^{P} \sum_{J \neq I}^{P} \frac{Z_I Z_J}{|\mathbf{R}_I - \mathbf{R}_J|} \\ &+ \frac{e^2}{2} \sum_{i=1}^{N} \sum_{j \neq i}^{N} \frac{1}{|\mathbf{r}_i - \mathbf{r}_j|} - e^2 \sum_{I=1}^{P} \sum_{i=1}^{N} \frac{Z_I}{|\mathbf{R}_I - \mathbf{r}_i|} \end{aligned} \tag{3.2}$$

where R_I is the coordinate of the ions at site I, r_i is the coordinate of the electron i, Z_I are ion charges, and M_I are the nuclear masses, respectively. In principle, properties of the system in the ground state can be

solved by an eigenvalue problem, also known as Schroedinger equation,

$$\mathscr{H}\Psi_n(\mathbf{R},\mathbf{r}) = \mathscr{E}_n\Psi_n(\mathbf{R},\mathbf{r}) \tag{3.3}$$

where Ψ_i and ε_i are the energies (eigenvalue) and stationary states (eigenfunctions) of the Schroedinger equation. Given that electrons are fermions, the wavefunction is anti-symmetric with respect to the electronic coordinates ($\mathbf{r}$). An ion can be either fermions or bosons; therefore, the wavefunction would be either symmetric or anti-symmetric with respect to the ionic coordinates ($\mathbf{R}$) . In reality, materials are made of about 10^{18} atoms or more, each having multiple electrons, which means the Schroedinger equation is impossible to be solved. Exact numerical estimation are available for very small systems, including a hydrogen atom (H), $H_2{}^+$. Furthermore numerical estimation of the Eq. 3.3 is also limited to very small systems. There are several contributing factors that make this problem difficult, but the most notable ones are due to the many-body nature of electrons and the two-body Coulomb interaction which makes it impossible to decouple Eq. 3.2. As a result, there would be coupled 3(N+P) equations that needs to be solved.

In the past century, there have been many efforts by prominent physicists to tackle this problem and reduce it to a form that can be applied to larger systems. In particular, the most basic approach might be to consider the total wavefunction as the product of the single electron wavefunctions. With the assumption of the *exchange* interaction, meaning that every electron occupies a single energy state (fermion distribution), this can be written in form of the Slatter determinant asinn Eq. ,

$$\frac{1}{\sqrt{N!}}\begin{vmatrix} \varphi_1(1) & \varphi_2(1) & \cdots & \varphi_N(1) \\ \varphi_1(2) & \varphi_2(2) & \cdots & \varphi_N(2) \\ \vdots & \vdots & \ddots & \vdots \\ \varphi_1(N) & \varphi_2(N) & \cdots & \varphi_N(N) \end{vmatrix} \tag{3.4}$$

However, this form assumes that an electron at r_1 does not influence the electron at r_2. In another words, the wavefunctions of each electron is considered to be independent of the rest of the electrons, or more physically, the probability of finding electrons at an specific location in the space is independent of the location of the rest of the electrons in the system. Given that electrons are negatively charged, they repel each other due to the Coulomb force. Therefore, the Slater determinant is at odds with the repulsive electron-electron interactions. In reality, a single electron is influenced by all the other electrons in the system. This phenomenon is called *correlation*. In general, both "*exchange*" and "*correlation*" are proved to have signigicant influence on the physical properties of the system, yet they are the most challenging effects to compute. In the following sections, I focus on one of the common methods used in studying solid state systems, also known as Density Functional theory (DFT), and how it works [55].

3.2 Density Functional Theory

3.2.1 Thomas-Fermi-Dirac theory

One of the major lines of thought on solving Eq. 3.2 or the many-body problem, is to use the electronic density as opposed to the wave function as the primary quantity to be solved for. This was first developed by Thomas and Fermi independently in the late 1920s. The idea was to write each energy term in Eq. 3.1 in form of a functional of density as follows,

$$E_\alpha[\rho] = \int \rho(\mathbf{r})\varepsilon_\alpha[\rho(\mathbf{r})]\mathrm{d}\mathbf{r} \tag{3.5}$$

where $E_\alpha[\rho]$ is the energy functional of the electron density, dependent on the electron distribution, and $\varepsilon_\alpha[\rho]$ is the corresponding energy density which can be estimated separately for each term in Eq. 3.1. In the simplest approximation, the kinetic term can be approximated to follow the behavior of a homogeneous electron gas. The exact analytical solution for such a simplified case was derived and discussed in detail in many introductory solid state books [56], [57] and can be written as,

$$\varepsilon_T[\rho] = \frac{3}{5}\frac{\hbar^2}{2m}\left(3\pi^2\right)^{2/3}\rho^{2/3}. \tag{3.6}$$

Therefore, the kinetic term can be written as,

$$T_{\mathrm{TF}} = C_{\mathrm{k}}\int \rho(\mathbf{r})^{5/3}\,\mathrm{d}\mathbf{r} \tag{3.7}$$

Similarly all other terms including the exchange energy (E_X), correlation energy (E_C) were estimated to be,

$$E_{\mathrm{X}}[\rho] = -C_{\mathrm{X}}\int \rho(\mathbf{r})^{4/3}\,\mathrm{d}\mathbf{r} \tag{3.8}$$

$$E_{\mathrm{C}}[\rho] = -0.056\int \frac{\rho(\mathbf{r})^{4/3}}{0.079+\rho(\mathbf{r})^{1/3}}\,\mathrm{d}\mathbf{r}. \tag{3.9}$$

Together, Eq. 3.7 to Eq. 3.8 can be replaced with the original terms in Eq. 3.1 and final expression can be written as,

$$E_{\mathrm{TF}}[n] = C_1\int \mathrm{d}^3 r n(\mathbf{r})^{(5/3)} + \int \mathrm{d}^3 r v_{\mathrm{ext}}(\mathbf{r})n(\mathbf{r}) + C_2\int \mathrm{d}^3 r n(\mathbf{r})^{4/3} + \frac{1}{2}\int \mathrm{d}^3 r\,\mathrm{d}^3 r' \frac{n(\mathbf{r})n(\mathbf{r}')}{|\mathbf{r}-\mathbf{r}'|} \tag{3.10}$$

where $v_{\mathrm{ext}}(\mathbf{r})$ is the interaction potential between the ions and the electrons, and all the numbers are in the units of Ry. It can be seen that E_{TF} is only dependent on the electron density. Based on the variational principle, minimization of E_{TF} with respect to $\rho(r)$ in the three dimensional space, such that energy is stationary with any deviations in the density can lead to the ground state density. With the constraint that the total number of electrons is constant, ($\int \rho(\mathbf{r})\mathrm{d}\mathbf{r} = N$), this can be solved using the Lagrange multipliers. Variation with respect to density results in,

$$\mu = \frac{5}{3}C_{\mathrm{k}}\rho(\mathbf{r})^{2/3} + v_{\mathrm{ext}}(\mathbf{r}) + \int \frac{\rho(\mathbf{r}')}{|\mathbf{r}-\mathbf{r}'|}\mathrm{d}\mathbf{r} - \frac{4}{3}C_{\mathrm{X}}\rho(\mathbf{r})^{1/3} + \mu_{\mathrm{c}}[\rho(\mathbf{r})] \tag{3.11}$$

where $\mu_{\mathrm{c}}[\rho(\mathbf{r})]$ is the exchange-correlation potential, and μ is the chemical potential. The importance of this expression is that one can find the electron density as a function of the external potential. This

problem can be solved iteratively, where one starts with a guess for the external potential, then finds the electron density from Eq. 3.11, then finds the new external potential and consequently new electron density. Note that the external potential is the only term in the original Hamiltonian where the exact dependence on the electron density is known. The iterative cycle continues until one finds no (or negligible) changes in the density. The main limitation of this model is the assumption that the system can be reduced to a homogeneous electron gas locally. This means that the kinetic term in Eq. 3.7 is locally homogeneous, which is a crude approximation especially for atomic or molecular systems.

3.2.2 The Hohenberg-Kohn Theorem

It took more than 30 years until a solid proof by Hohengerg and Kohn [58] showed that the energy can be written exclusively in terms of the electron density. The two main theorems that are the backbones of DFT calculations are discussed in this section.

Theorem 1: The external potential can be uniquely determined from the electron density. This means that the external potential is a unique functional of the electron density. To prove this theorem, one starts with the opposite assumption, i.e. the external potential is not uniquely defined by the electron density. Consider E_0 and ψ_0 to be the ground start energy and wave function of the Hamiltonian $H = T + V_{ext} + U_{ee}$. Let E_0' and ψ_0' to be the ground start energy and wave function of the Hamiltonian $H' = T + V_{ext}' + U_{ee}$. According to the variational principle, the ground state energy is lower than expectation energy of any other wavefunction other than the ground state wave function,

$$\begin{aligned} E_0 < \langle \Phi' | \hat{H} | \Phi' \rangle &= \langle \Phi' | \hat{H}' | \Phi' \rangle + \langle \Phi' | \hat{H} - \hat{H}' | \Phi' \rangle \\ &= E_0' + \int \rho(\mathbf{r}) \left[v_{\text{ext}}(\mathbf{r}) - v_{\text{ext}}'(\mathbf{r}) \right] \mathrm{d}\mathbf{r}. \end{aligned} \tag{3.12}$$

If we perform the same thing to the $\psi\prime$ and its ground state,

$$\begin{aligned} E_0' < \langle \Phi | \hat{H}' | \Phi \rangle &= \langle \Phi | \hat{H} | \Phi \rangle + \langle \Phi | \hat{H}' - \hat{H} | \Phi \rangle \\ &= E_0 - \int \rho(\mathbf{r}) \left[v_{\text{ext}}(\mathbf{r}) - v_{\text{ext}}'(\mathbf{r}) \right] \mathrm{d}\mathbf{r}. \end{aligned} \tag{3.13}$$

One can notice that the second term on the right hand side of the Eq. 3.12 is written with the assumption of having a single density $\rho(r)$. If we add the Eq 3.12 and Eq. 3.13,

$$E_0 + E_0' < E_0' + E_0 \tag{3.14}$$

which is absurd. Therefore, there cannot be two different external potentials v_{ext} and v'_{ext} that correspond to the same electron density. Since $\rho(\mathbf{r})$ uniquely determines v_{ext}, the ground state wavefunction can be obtained by solving the full many-body Schroedinger equation from the electron density.

Theorem 2: The electron density that minimizes the energy functional is the true ground state density of the system. To prove this theorem one can assume the functional of energy for a given density $\tilde{\rho}$, written as,

$$E_{\mathrm{v}}[\tilde{\rho}] = F[\tilde{\rho}] + \int \tilde{\rho}(\mathbf{r}) v_{\mathrm{ext}}(\mathbf{r}) d\mathbf{r} \tag{3.15}$$

where the first term is the universal function,

$$F[\tilde{\rho}] = \left\langle \Phi[\tilde{\rho}] \left| \hat{T} + \hat{U}_{\mathrm{ee}} \right| \Phi[\tilde{\rho}] \right\rangle \tag{3.16}$$

and the second term is written based on the first theorem asserted earlier. According to the variational principle, the total energy is minimum only for the true ground state wavefunction,

$$E_0 = E_{\mathrm{v}}[\rho]. \tag{3.17}$$

Therefore, for any $\rho \neq \tilde{\rho}$,

$$E_0 < E_{\mathrm{v}}[\tilde{\rho}]. \tag{3.18}$$

Consequently, the minimization of the energy function with respect to density can yield the ground state energy and density of the system,

$$\delta\left\{E_{\mathrm{v}}[\rho]-\mu\left(\int\rho(\mathbf{r})\mathrm{d}\mathbf{r}-N\right)\right\}=0 \tag{3.19}$$

$$\mu=\frac{\delta E_{\mathrm{v}}[\rho]}{\delta\rho}=v_{\mathrm{ext}}(\mathbf{r})+\frac{\delta F[\rho]}{\delta\rho}. \tag{3.20}$$

Note that Eq. 3.20 is the generalized form of the Thomas-Fermi-Dirac equation, discussed in the precious section. It is important to understand that $F[\rho]$ only depends on the electron density and is not explicitly dependent on the external potential. Thus, knowing $F[\rho]$ implies the knowledge of the full many-body equation.

In the aforementioned theorems, the only constraint in the system was the conservation of electrons, i.e. total number of electrons remain invariant. However, it is also required that the electron density corresponds to some ground state antisymmetric wave function. In the variational search mechanism, trial densities that are unacceptable may be obtained. Levy [59] reformulated DFT in a way that antisymmetric origin of the wave function is guaranteed. This means that the search is constrained to the subspace of all antisymmetric wavefunctions that yield the same density ρ written as,

$$F[\rho]=\min_{\Phi\to\rho}\left\{\left\langle\Phi\left|\hat{T}+\hat{U}_{\mathrm{ee}}\right|\Phi\right\rangle\right\}. \tag{3.21}$$

3.2.3 Kohn-Sham Equations

As discussed earlier, the most challenging part of the Hamiltonian is the electron-electron interaction term U_{ee}. The best strategy to deal with this term is to separate it and write it in terms of the classical electrostatic term (Hartree) and exchange-correlation terms. This is practically useful because the unknown electron-electron interaction can now be written in terms of their importance: The Hartree term or the mean-field electrostatic interaction, which has the largest contribution, is known exactly. The next largest contribution comes from the exchange term, which can be estimated exactly as in the Hartree-Fock

method that uses Slater determinants. In practice, exact calculation of the exchange term is computationally costly and, unless not required for a particular reason, it is approximated. The most challenging part of the Hamiltonian is the correlation interaction, which usually has the smallest contribution to the Hamiltonian. The correlation interaction reflects the fact that an electron repels the other electrons around it, thus improving on the Hartree approximation of a stationary, mean-field electron distribution. Different types of approximations in defining the correlation potential has been used (LDA, GGA, etc.), and we refer the reader to a more generalized text book on the various exchange-correlation potentials that are dealt with for more in-depth discussion [55], [60].

Excluding the electron-electron interaction, the main problem in the Thomas-Fermi-Dirac approximation is the kinetic energy term. According to Eq. 3.2, the exact expression requires knowing second spatial derivative of the electron density matrix, which cannot be easily determined in terms of the density. The reason that the Thomas-Fermi-Dirac approximation is far from correct is due to this inherent non-locality of the kinetic operator. Numerical estimation of a Laplacian of a function at site r not only depends on the function at r but also to within a certain range of the function $F(\mathbf{r}+\delta)$.

In 1965, Kohn and Sham [61], proposed a more generalized approach to deal with the kinetic energy estimation. For a system of non-interacting electrons, the wavefunction that describes the system is in form of Slater determinant, i.e. an antisymmetric combination of products of one-electron wavefunctions ($\phi_i(\mathbf{r})$) that are anti-symmetric. The electron density matrix in the ground state can then be written as,

$$\rho_1\left(\mathbf{r},\mathbf{r}'\right)=\sum_{i=1}^{\infty} f_i\varphi_i(\mathbf{r})\varphi_i^*\left(\mathbf{r}'\right) \tag{3.22}$$

where f_i is the occupation number of electrons in state i. Then, the exact expression for the kinetic energy can be written as,

$$T=-\frac{\hbar^2}{2m}\sum_{i=1}^{\infty} f_i\left\langle\varphi_i\left|\nabla^2\right|\varphi_i\right\rangle. \tag{3.23}$$

If one can find a system of non-interacting electrons with the same electron density as in the interacting system, then the kinetic energy of the system can be well approximated by Eq. 3.23. This obviously is not

the exact kinetic energy of the interacting system, because the Slater determinant is not the true solution of the many-body wavefunction. Specifically, the missing fraction is from electron correlation, and is typically treated by adding it to the total correlation energy of the system.

We assume a system of non-interacting electrons where the electron density $\rho(\mathbf{r})$ coincides with that of the interacting electron system. The Hamiltonian that can describe the system can be written as,

$$\hat{\mathscr{H}}_{\mathrm{R}} = \sum_{i=1}^{N} \left[-\frac{\hbar^2}{2m} \nabla_i^2 + v_{\mathrm{R}}(\mathbf{r}_i) \right] \tag{3.24}$$

where the potential v_R is called the reference potential, such that the ground state density of $\hat{\mathscr{H}}_{\mathrm{R}}$ equals $\rho(\mathbf{r})$. According to the Hohenberg-Kohn theorems, the ground state energy of the non-interacting system would then equal the ground state energy of the interacting system.

Assuming that the electrons occupy doubly degenerate states, the electron density can be written as,

$$\rho(\mathbf{r}) = 2 \sum_{i=1}^{N_{\mathrm{s}}} |\varphi_i(\mathbf{r})|^2 \tag{3.25}$$

where $N_s = N/2$ and N is the total number of electrons. Then the kinetic energy can be written as,

$$T_{\mathrm{R}}[\rho] = -\frac{\hbar^2}{m} \sum_{i=1}^{N_{\mathrm{s}}} \left\langle \varphi_i \left| \nabla^2 \right| \varphi_i \right\rangle \tag{3.26}$$

where ϕ_i are the single electron wavefunctions that are the solution of the one-electron non-interacting Hamiltonian:

$$\hat{H}_{\mathrm{KS}} = -\frac{\hbar^2}{2m} \nabla^2 + v_{\mathrm{R}}(\mathbf{r}) \tag{3.27}$$

and are obtained by solving the Schroedinger equation,

$$\hat{H}_{\mathrm{KS}} \varphi_i(\mathbf{r}) = \varepsilon_i \varphi_i(\mathbf{r}) \tag{3.28}$$

The Hamiltonian of the interacting system in Eq. 3.21, using the new estimation of kinetic energy from the non-interaction system yields,

$$F[\rho] = T_{\mathrm{R}}[\rho] + \frac{1}{2}\iint \frac{\rho(\mathbf{r})\rho(\mathbf{r}')}{|\mathbf{r}-\mathbf{r}'|}\mathrm{d}\mathbf{r}\mathrm{d}\mathbf{r}' + \tilde{E}_{\mathrm{XC}}[\rho] \tag{3.29}$$

where $\tilde{E}_{\mathrm{XC}}[\rho]$ is the modified exchange-correlation term to correct the correlation contribution of the kinetic energy of the interacting system. The total energy functional can be written as,

$$E_{\mathrm{KS}}[\rho] = T_{\mathrm{R}}[\rho] + \int \rho(\mathbf{r}) v_{\mathrm{ext}}(\mathbf{r})\mathrm{d}\mathbf{r} + \frac{1}{2}\iint \frac{\rho(\mathbf{r})\rho(\mathbf{r}')}{|\mathbf{r}-\mathbf{r}'|}\mathrm{d}\mathbf{r}\mathrm{d}\mathbf{r}' + \tilde{E}_{\mathrm{XC}}[\rho]. \tag{3.30}$$

where $E_{KS}[\rho]$is the energy functional constructed from the electron density of the non-interacting wavefunctions or "Kohn-Sham" orbitals. Without going into more detail, it is crucial to know that KS wavefunctions are different from the true many-body wavefunction of the system. It was shown by Gorling [62] that they are not at all meaningless though and can be considered as the zeroth order approximation of the true wavefunction of the system.

The remaining task in finding the non-interacting electron density is to determine what the reference potential v_R is. To estimate it, one can use the variational principle for Eq. 3.30 with the usual constraint that total number of electrons are constant,

$$\frac{\delta}{\delta\rho(\mathbf{r})}\left(E_{\mathrm{KS}}[\rho] - \mu\int \rho(\mathbf{r})\mathrm{d}\mathbf{r}\right) = 0 \tag{3.31}$$

which yields the expression for the electronic chemical potential:

$$\mu = \frac{\delta T_{\mathrm{R}}[\rho]}{\delta\rho(\mathbf{r})} + v_{\mathrm{ext}}(\mathbf{r}) + \int \frac{\rho(\mathbf{r}')}{|\mathbf{r}-\mathbf{r}'|}\mathrm{d}\mathbf{r}' + \frac{\delta\tilde{E}_{\mathrm{XC}}[\rho]}{\delta\rho(\mathbf{r})} \tag{3.32}$$

Similarly for the non-interaction system exposed to v_R, the variational principle and consequently the functional derivative can be written as,

$$\frac{\delta T_{\mathrm{R}}[\rho]}{\delta \rho(\mathbf{r})} + v_{\mathrm{R}}(\mathbf{r}) = \mu_{\mathrm{R}} \tag{3.33}$$

where μ_R is the chemical potential of the non-interacting system. In reality, if the non-interacting system is representing the interaction system, when these two system are brought into contact, there should be zero charge flow from one to the other (i.e., equilibrium). Therefore, the chemical potential of the interaction and non-interacting systems should be the same. Comparing Eq. 3.33 and Eq. 3.32, the $v_{\mathrm{R}}(\mathbf{r})$ can then be estimated as,

$$v_{\mathrm{R}}(\mathbf{r}) = v_{\mathrm{ext}}(\mathbf{r}) + \int \frac{\rho\left(\mathbf{r}'\right)}{|\mathbf{r} - \mathbf{r}'|} \mathrm{d}\mathbf{r}' + \mu_{\mathrm{XC}}[\rho](\mathbf{r}) \tag{3.34}$$

All the right hand side terms are now functionals of electron density. The following steps needs to be taken in order to apply the KS equation for a many-body system:

(1) Start with an initial guess for the KS wavefunctions. These can be constructed from the atomic orbitals of the system under study. Then construct the initial density according to Eq. 3.25

(2) Find the reference potential according to the Eq. 3.34 and kinetic contribution according to Eq. 3.26

(3) Solve the non-interacting system of electrons in presence of the reference potential

(4) Find the new KS wavefunctions and electron density

(5) Compare the new electron density to the old guess of the electron density.

If the difference between them is negligible (determined externally with a threshold), the solution of the KS wavefunction can yield the true ground state of the system. If the difference is not negligible, we then assign the new density as the initial density and perform steps (1) to (4) again. This cycle continues until reaching convergence. In reality, instead of using the exact final density of one cycle as the initial density of the next cycle, both the initial and final densities are combined using a ratio called the "mixing factor" before the start of the new cycle.

3.3 Details of DFT in this study

Going further into the mathematical details of the derivations of DFT is beyond the scope of this dissertation. Therefore, I refer an interested reader to study the books by Martin [60] or Kohanoff [55] where many additional details of the methods, especially on using pseudopotentials, are provided. In this section, the details of parameters that are used for all the DFT calculations carried out in this dissertation are discussed.

The computer code Quantum Espresso [63], an open-source code that has been widely used in many different fields of physics and chemistry, was used in the research presented in this dissertation. The code uses plane-waves as the basis-set for the construction of KS wavefunction and electron density. The exchange-correlation potential ($\mu_c[\rho(\mathbf{r})]$) were calculated in the framework of the generalized-gradient approximation(GGA) [64]. This approximation adds the non-homogeneity of the true electron density by expanding the energy density in terms of electron density and the gradients of the electron density. The exact form of the functional in the present study is PBEsol [65] (revised version of PBE [66] for solids). The cost of calculations were reduced significantly reduced by using ultrasoft pseudopotential [67] that requires lower cutoff energy for the plane-wave basis set. For integrations in the Brillouin zone, the Monkhorst-Pack [68] scheme was used to create a uniform grid of k-points.

The structure of the bulk SnO_2 is tetragonal with lattice parameters of 'a' and 'c' and internal parameter 'u' as can be seen in Fig. 3.1. Using converged values of 55 Ry for kinetic-cutoff energy and $4\times4\times4$ for k-point mesh grid, I calculated 4.76 Å, 3.21 Å, and 0.306 for a,c and u respectively. These are in great agreement with experimental values of 4.737 , 3.19 and previous DFT studies [20] . Such high accuracy is mainly due to using PBEsol, which is known to improve lattice structure predictions over the conventional PBE functional [65].

The (101) and (110) surface terminations are constructed from the converged values of lattice parameters of the bulk of SnO_2. The stability of the surface was determined by two factors: the vertical vacuum thickness of the simulation box, and the thickness of the slab. In the former case, a vacuum thickness of

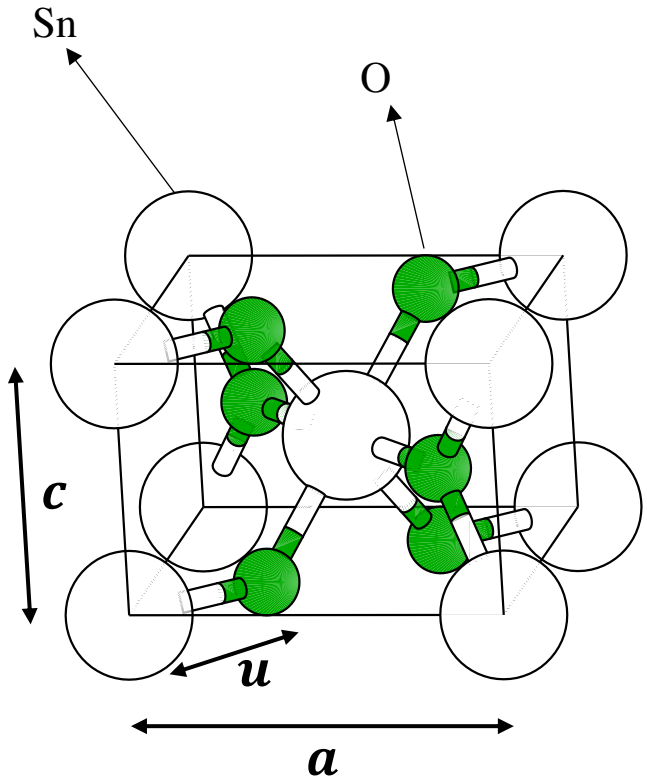

Figure 3.1: The tetragonal bulk structure of SnO_2 with lattice parameters of '*a*' and '*c*' and internal parameter '*u*'. Oxygen and tin atoms are shown with green and white circles, respectively.

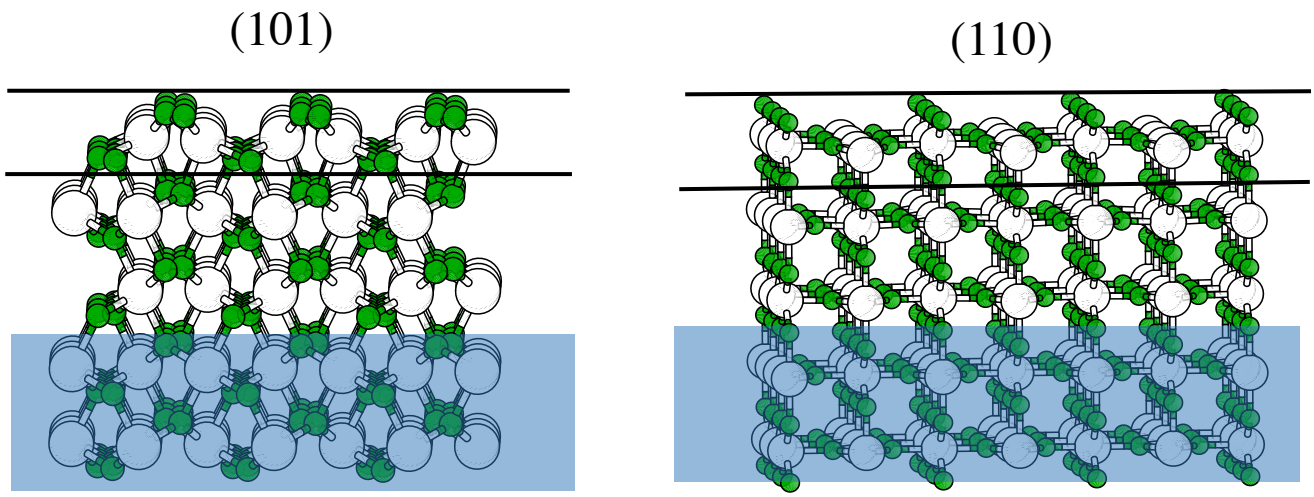

Figure 3.2: The side-view of the relaxed slabs of the (101) and (110) surface terminations. In both cases, the solid black lines at the top shows a trilayer. The blue-shaded area are to indicate that the bottom two trilayers are fixed.

15Åwas found to be large enough to avoid any interaction between the slab with its periodic images. Then, at a fixed vacuum depth of 15Å, we tested different thickness of the slabs of SnO_2 as shown in Fig. 3.2. In case of (101) surface, a 'trilayer' of slab is defined as a layer of Sn atoms sandwiched by layers of oxygen above and below. Similarly, for (110) surface, a trilayer refers to O-Sn_2O_2-O units. The goal is to find the optimum thickness such that close to the center of the slab, the interlayer spacing between trilayers is identical to the bulk structure values. Our analysis show that for both terminations, the atoms belonging to the third trilayer undergo relaxation less than 0.01 Å. Therefore, for all the surface calculations, surfaces made of 5 trilayers with two bottom trilayers fixed for both (101) and (110) are good enough to represent an oxidized (stoichiometric) semi-infinite surfaces.

Relaxation of the surface is performed until the forces on the atoms are less than $10^{-4} Ry/a.u.$ In total, a set of 30 distinct defective configurations for the (101) surface and 75 for (110) surface was calculated. To estimate the isolated vacancy energy formation, or scenarios with just one type of two-body interactions surface unit-cells of 3×3 and 4×2 were used. Once the surface energies for all these configurations are

calculated, the best fit model Hamiltonian, as discussed in the earlier section, can be fitted to the set. Any parameter that is less 10^{-2} eV, i.e. about two order of magnitude smaller than the largest parameter, is ignored. It should be emphasized that a small number of the configurations in the DFT relaxations underwent surface reconstruction (particularly at the (110) surface), distorting the trilayer significantly so that it is no longer similar to the oxidized structure. This is particularly true when there is a high density of vacancies at the surface. Such scenarios cannot be described by the model Hamiltonian and are entirely omitted.

Chapter 4

Thermodynamics of Oxygen Vacancies

One of the main limitations of DFT calculations is that it is limited to a closed system and can only predict the ground state, or zero temperature structure of the system. Typically, this approximation can be expanded to finite temperature if the system does not undergo a phase transition. In this chapter, I will first introduce the *Ab-initio* thermodynamics, a known method that has been used in the past two decades in studying the thermodynamic properties at finite temperature using a selection of DFT calculations. Then, I will move on to Monte Carlo simulations and how they can be combined with DFT.

4.1 Abinitio-Thermodynamics

One of the useful methods in studying the thermodynamics of solid surfaces, is known as atomistic-thermodynamics or *Ab-initio* thermodynamics. In 2001, in a study by Reuter [36] on the adsorption of O_2 and CO on RuO_2, they were able to predict the most stable surface composition of the (110) surface termination, in great quantitative agreements with experimental studies. This was based on the assumption that the surface is in thermal equilibrium with a reservoir of O_2 and CO, at a temperature of T. The most stable surface of the system is the one that minimizes the surface free energy,

$$\gamma(T,p) = \frac{1}{2A}\left[G^{\text{slab}}\left(T,p,N_{\text{Ru}},N_{\text{O}}\right) - N_{\text{Ru}}\mu_{\text{Ru}}(T,p) - N_{\text{O}}\mu_{\text{O}}(T,p)\right] \tag{4.1}$$

where G is the Gibbs free energy, the appropriate thermodynamic potential to describe the system, and μ_i and N_i are the chemical potential and total number of species i of the system. Note that γ is normalized with respect to the surface area of the system. If the species in the reservoir are not necessarily in the gas phase, then further thermodynamic consideration needs to be applied. For example, in the case of SnO_2, the Eq. 4.1 can be written as,

$$\gamma(T,p) = \frac{1}{2A}\left[G^{\text{slab}}\left(T,p,N_{\text{Sn}},N_{\text{O}}\right) - N_{\text{Sn}}\mu_{\text{Sn}}(T,p) - N_{\text{O}}\mu_{\text{O}}(T,p)\right]. \tag{4.2}$$

However, if there is enough bulk material to act as a reservoir, the chemical potentials are no longer independent can be related by the Gibbs-Durham formula,

$$\mu_{\text{Sn}}(T,p) + 2\mu_{\text{O}}(T,p) = g^{\text{bulk}}_{\text{SnO}_2}(T,p) \tag{4.3}$$

where g is the Gibbs free energy of the unit-cell of SnO_2. Replacing the μ_{Sn} in Eq. leads to,

$$\begin{aligned}\gamma(T,p) = \frac{1}{2A}\Big[&G^{\text{slab}}\left(T,p,N_{\text{Sn}},N_{\text{O}}\right) - N_{\text{Ru}}g^{\text{bulk}}_{\text{SnO}_2}(T,p) \\ &+ \left(2N_{\text{Sn}} - N_{\text{O}}\right)\mu_{\text{O}}(T,p)\Big].\end{aligned} \tag{4.4}$$

In reality, the Gibbs energies are also temperature dependent. However, if we want to make use of DFT calculations, G can be assumed to be the DFT energy estimation of the surface and g as the DFT estimation of bulk SnO_2. With this approximation, only the chemical potential of oxygen depends on the temperature and partial pressure.

The physically relevant values of oxygen chemical potential can be estimated from the Eq. 4.3. In particular, if the system is in an oxygen poor environment, or in other words, when μ_O is minimum, the μ_{Sn} is maximum or the system is in a tin rich environment. In that case, Sn would form in its bulk lattice Sn structure. Therefore, with a DFT estimation of the bulk energy of Sn, the maximum relevant oxygen

chemical potential can found as,

$$\max\left[\mu_{\mathrm{Sn}}(T,p)\right] = g^{\mathrm{bulk}}_{\mathrm{Sn}}(T,p). \tag{4.5}$$

On the other hand, in an oxygen rich environment, the most stable phase of oxygen would be its gaseous form (liquid or solid phases are at typically very low temperature). This means the lower limit of μ_O can be written as,

$$\min\left[\mu_{\mathrm{O}}(T,p)\right] = \frac{1}{2}\left[g^{\mathrm{bulk}}_{\mathrm{SnO_2}}(0,0) - g^{\mathrm{bulk}}_{\mathrm{Sn}}(0,0)\right]. \tag{4.6}$$

Therefore, the range of μ_O that is of interest to us can be written as,

$$\frac{1}{2}\Delta G_f(0,0) < \mu_{\mathrm{O}}(T,p) - \frac{1}{2}E^{\mathrm{total}}_{\mathrm{O_2}} < 0. \tag{4.7}$$

It should also be mentioned that oxygen chemical potential can be directly written in terms of temperature and pressure using,

$$\mu_{\mathrm{O}}(T,p) = \mu_{\mathrm{O}}\left(T,p^{\circ}\right) + 1/2kT\ln\left(\frac{p}{p^{\circ}}\right) \tag{4.8}$$

where we used the assumption that O_2 gas is dilute enough such that it can be considered as an ideal gas in the reservoir. Also, $\mu_{\mathrm{O}}\left(T,p^{\circ}\right)$ is a reference potential at p° which is typically taken from the thermodynamic tables.

With the aforementioned discussion on the theory of the *Ab-initio* Thermodynamics, one can use the methodology in studying the adsorption of molecules and atoms on the surface [36], [69]–[73]. Just to show an example one can interpret the results, an example from the Ref. [71] is adopted here. The problem of understanding the adsorption of O and CO on the (110) surface of RuO_2 can be dealt with in several steps: (1) Perform DFT calculation on a set of different configurations of the surface, each having distinct pattern of O and CO adsorbed on the surface. These are guesses based on the available information and physical intuition of the system under study. (2) Calculate Eq. 4.1 with an additional

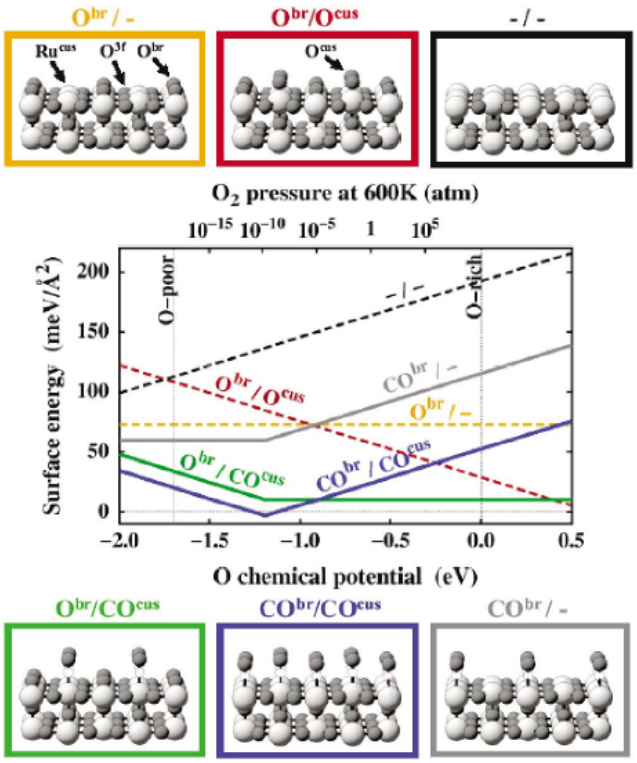

Figure 4.1: Surface energy evaluation based on *Ab-initio* Thermodynamics for six different configurations of the surface. All the configurations are shown with a distinct color and small sub-figures at the top and bottom of the main figure shows the atomic arrangement for each configuration.

term corresponding to a reservoir of CO also present in the system. (3) Plot the surface free energies as a function of chemical potential of either O_2 or CO or both (depending on the questions one is seeking to answer) for all the distinct configurations. An example of a typical plot for six different configurations is shown in Fig. 4.1. The most stable surface configuration would be the one with the minimum surface free energy in the given range of chemical potential. For example, in Fig. 4.1, for $\mu_O > -0.8$ the structure labeled as O^{br}/CO^{cus}, shown as a green line in the plot has the lowest energy and therefore is the most stable surface configuration. On the other hand, CO^{br}/CO^{cus} (shown in dark blue) is the most stable configuration for $\mu_O < -0.8$. All other configurations have higher surface free energies in the entire range

of μ_O of interest. So in all the cases, the question is which structure has the lowest surface free energy at a fixed chemical potential.

4.2 Model Hamiltonian

Ab-initio Thermodynamics depends heavily on the DFT calculations that were performed for each different configurations. In the cases shown in Fig. 4.1, DFT calculations were done for each configuration and then plots are depicted according to Eq. 4.1. One major difficulty that one may face is the estimation of the surface energy for configurations that require larger surface area. The DFT calculations can become demanding, and this method loses its efficiency in predicting the most stable surface configurations. One possible remedy to this problem is to use simplified models that can estimate the energy of the surface without doing the exact calculations at the DFT level: In other words, mathematical models that can be well fitted to some of the available DFT calculations and are able to predict surface energies for configurations that are computationally costly to do at the DFT level. One of the simplest and most robust models is called "lattice gas model" [74] which has been used in wide range of problems, from alloys in bulk structures to adsorption of atoms and molecules on surfaces and more recently combined with kinetic MC simulations [75]–[80]. This model is based on the assumption that molecules/atoms/vacancies are occupying different sites of a lattice (which can be any dimensional lattice). The interaction among the sites of the lattice can be written in a general form of:

$$H_{int} = \sum_{k} a(\alpha_k)\sigma_k + \frac{1}{2}\sum_{k,l} b(\beta_{kl})\sigma_k\sigma_l + \frac{1}{6}\sum_{k,l,m} c(\gamma_{klm})\sigma_k\sigma_l\sigma_m + ... \tag{4.9}$$

The binary value variables, σ_k, is defined to be 1 if the corresponding site, k, is occupied , otherwise 0. The coefficients a, b and c correspond to on-site (i.e. one-body), two-body and three-body interaction magnitudes among the sites. The α_k, β_{kl} and γ_{klm} indicate the type of site clusters; for example a two-body interaction can be between the nearest neighbor sites or second-nearest neighbors sites, etc. To have a better idea of how Eq. 4.9 is applied to different system, here an example of the system studied in this

dissertation is provided. Consider that oxygen vacancies are the elements that we are trying to find their energetic and interactions. The first term in Eq. 4.9 corresponds to having isolated vacancies in the system. Depending on the type of vacancies (bridging or in-plane), α_k can have different values and consequently different energy contribution to the total energy. Similarly, for two-body and three-body interactions, β_{kl} can correspond to nearest neighbor in-plane/in-plane vacancy interaction or bridging/bridging second-nearest interaction. For three-body interactions, γ_{klm}, can refer ti a particular 3-body shape (e.g. L-shape). All these different types of interaction are counted and then the total energy correspond to the surface energy of a vacancy pattern. The main task is to find the best a, b and c values that can fit Eq. 4.9 to the exact results and have the predictive power of estimating the total energies of unknown surface structure patterns.

To find the parameters in the model Hamiltonian (i.e. lattice gas model), one needs a training set of samples. This means a set of different surface configurations where the exact value of total energy is available. Then by fitting Eq. 4.9 to the training set, all the interactions and their magnitudes can be determined. In this study, the exact energies are calculated using DFT for relatively small surface cells (up to 9 times of the unit-cell). Oxygen vacancy formation energy $E_{surface}$ can be estimated as,

$$E_{surface} = E_{def} + \frac{1}{2} n E_{O_2} - E_{st} \tag{4.10}$$

where E_{def} correspond to the energy of the surface with oxygen vacancies and E_{st} correspond to the stoichiometric surface energy, respectively. E_{O_2} refers to the energy of an oxygen molecule in its triplet state and n is the total number of missing oxygen atoms, or vacancies. The calculations of E_{O_2} were done in a periodic cell of length 15 Å, sufficient to avoid image-image interaction in DFT calculations that are based on a plain-wave basis set. Note that E_{st} and E_{O_2} are constant values and determined only once, while E_{def} can heavily change depending on the types of vacancies, their concentration, radial distribution, and surface relaxations. Calculating $E_{surface}$ for a set of distinct defective surface configurations is necessary to understand the interactions among vacancies. Defective configurations that are equivalent by the

symmetries of the surface have identical energies, and thus provide no additional information and are not included in the training set.

There remain some important details for the construction of the model Hamiltonian that need to be answered. Specifically, the total number of parameters in the system, the convergence of the model Hamiltonian, the type of interactions between the vacancies and the predictive power of the model Hamiltonian all need to be carefully analyzed before having any physical analysis of the system under study. As one might expect, the answer to all the mentioned difficulties depends heavily on the complexity of the surface. For example, in our studies on the SnO_2(101) surface, there needs to be at least 9 parameters to predict surface energies in order to have errors less than one percent of DFT calculations. Such a surface would only have one type of element (bridging oxygen vacancy) and the morphology of the surface does not require having more than 1 four-body interaction. However, the more complex (110) surface, with both bridging and in-plane vacancies, requires at least 16 parameters and required multiple three-body interactions and four-body interactions. Moreover, the range of pairwise interactions can be different for each surface termination. For example, at (101), pairwise bridging/bridging interactions need to be included up to 6th nearest neighbor of a bridging site, while at (110), only up to 2nd nearest neighbor for the same interaction is necessary. Therefore, there cannot be certain presumption of how many parameters and what type of parameters need to be there. One can only answer these question after running several DFT calculations, calculating surface free energies and finding the most important interactions among the vacancies. The main goal is to have the fewest number of parameters such the the model Hamiltonian has a great predictive power in studying scenarios that are not included in the construction of the model Hamiltonian. This means that one should reserve some DFT calculations for testing the model Hamiltonian. If the percent error between them is larger than a selected criteria (for example 2 percent), there is either a missing parameter in the model Hamiltonian or a reconstruction at the DFT level. Further details on the implementation of the model Hamiltonian are discussed in chapters 5-8.

The model Hamiltonian in Eq. 4.9 is appropriate in a canonical ensemble. However, the surface in this study is in thermal and chemical equilibrium with an O_2 reservoir; therefore, a grand canonical

ensemble needs to be used to consider the variation of the number of vacancies at the surfaces. Such calculations can be performed as,

$$H = H_{int} - \mu_O(T,P)N \tag{4.11}$$

where N is the total number of oxygen atoms at the surface, and μ_O, the oxygen chemical potential, which depends on temperature and pressure, is an independent variable. This Hamiltonian allows the prediction of the total energy change when removing or adding oxygen vacancies to the system.

4.3 Monte Carlo simulations

With the Hamiltonian defined in Eq. 4.11, the next step is to find the most stable surface configuration. One of the popular and powerful methods in studying the thermodynamics and statistics in the past 7 decades is Monte Carlo simulations [81], [82]. As the name suggests, it depends on generation of random number numbers and stochastic simulations, unlike the previously discussed DFT calculations. This means that every time a simulation runs with a different set of random numbers, the final results would be different to within a certain statistical error. This study focuses on using Monte Carlo simulations in studying systems in equilibrium, where the energy of the system is determined by the model Hamiltonian Eq. 4.9 and the grand canonical potential Eq. 4.11. In the following subsections, I will briefly review the basic physics behind the Monte Carlo method [83], then narrow down to the specific scenarios that were tackled in this study.

4.3.1 Thermal Averages

To understand the equilibrium properties of a many-body system, the goal is to find thermal averages including average energy, heat capacity etc. This can be achieved by either time average integrations or phase-space integrations. The former scenario corresponds to simulations that are based on real-time relaxations of the system and is called the Molecular Dynamics (MD) [84] method. By using classical

methods including the Newton's second law, one can estimate the projected state of the system by solving the equations of motion numerically at real physical time. Such method has been largely used in dealing with any phases of the system (solid/liquid/gas) with more focus on the dynamics of the system under study. In the latter scenario, simulations are based on accessing all possible states that a system can reside in; in other words, all possible momentum and position (phase-space) values that the entire system can achieve. Such simulations do not depend on physical time, rather a non-physical time that determines how long it takes to cover all (or rather a majority) of phase-space. Monte Carlo (MC) simulations are numerical methods to achieve this.

The two mentioned methods, MD and MC should in theory, provide the exact same thermal averages when done correctly. In reality, one should have some physical intuition of the system and understanding of the important parameters, and difficulties in MD or MC before tackling a problem. For example, the MD simulations are performed at the time-scale of femto second (10^{-13} s). If a simulation requires much larger time-scale to reach equilibrium, such as microseconds, then the computational cost of the simulations would be overwhelmingly high.

With regard to the present study, we chose Monte Carlo simulations to study the systems. The main reason is the physical time to reach equilibrium. In particular, a surface that is exposed to a heat-bath with the transfer of some atoms to or from the surface can takes hours or even days to reach equilibrium in experimental studies. In particular, under reduced conditions of UHV, previous studies have shown that for a monolayer of oxygen to reach the surface, it may not take days but months. Such large time-scales are not feasible to study using MD. Also, hopping of oxygen atoms from one vacancy to another, which has been done extensively on different surfaces, happens on a relatively large time scales.

4.3.2 Equilibrium

Monte Carlo simulations are done stochastically, hence the system can be in any possible state S_i at a given time t with a probability $P(S_i, t)$. If one considers the conditional probability, S_i depends on the

preceding states S_{i-1}, S_{i-2}, ... at times t_{i-1}, t_{i-2}, ... as follows,

$$P\left(X_{t_n} = S_{i_n} \mid X_{t_{n-1}} = S_{i_{n-1}}, X_{t_{n-2}} = S_{i_{n-2}}, \ldots, X_{t_1} = S_{i_1}\right). \tag{4.12}$$

The simplest scenario of Eq. 4.12 is the assumption that any state only depends on the immediate preceding step, i.e. $P = P\left(X_{t_n} = S_{i_n} \mid X_{t_{n-1}} = S_{i_{n-1}}\right)$, then such process is called a Markov chain [85]. The sequence of the states that the system can reside in is called a Markov chain.

To simplify the discussion on Markov chains, we note that the conditional probability that a system goes to a new state j for a system that is in state i, can be referred to as a transition probability W_{ij},

$$W_{ij} = W\left(S_i \to S_j\right) = P\left(X_{t_n} = S_j \mid X_{t_{n-1}} = S_i\right). \tag{4.13}$$

Then the probability $P(S_j, t)$ can be written as,

$$P(S_j, t) = P\left(X_{t_n} = S_j \mid X_{t_{n-1}} = S_i\right) P\left(X_{t_{n-1}} = S_i\right) = W_{ij} P\left(X_{t_{n-1}} = S_i\right). \tag{4.14}$$

The so called master equation determines the change in the probability of the system and can be written as,

$$\frac{dP\left(S_j, t\right)}{dt} = -\sum_i W_{ji} P\left(S_j, t\right) + \sum_i W_{ij} P\left(S_i, t\right). \tag{4.15}$$

where the $-W_{ji}P(S_j, t)$ corresponds to the transtion from state j to all other states i and is negative because it decreases the probablity of the system to be in state j. Similarly, $W_{ij}P(S_i, t)$ corresponds to the transition of a system being in state i to state j, therefore increasing the chance of finding the system in state j. Equation 4.15 is another form of a continuity equation with loss and gain processes. One of the interesting features of the Eq. 4.15 is that the rate of the probability change at a given time t only depends on the other states at the same time t, i.e knowledge of the state of the system at time t, determines the future progress of the system. Therefore, the information of the preceding steps, play no role in the evolution of the system.

For a system to be in steady state conditions, the probability of the system at given state should remain invariant; i.e Eq. 4.15 needs to be zero. This condition leads to,

$$\sum_i W_{ji} P\left(S_j, t\right) = \sum_i W_{ij} P\left(S_i, t\right) \tag{4.16}$$

where the sum of all probabilities to the state j from all other states i, is equal to the outgoing probabilities of system going from state j to all other states. A stronger assertion would be to assume,

$$W_{ji} P\left(S_j, t\right) = W_{ij} P\left(S_i, t\right) \tag{4.17}$$

where transition between any two states i and j remains the same in both directions. This is called 'detailed balance' and is one of the main necessities of the system in thermal equilibrium.

4.3.3 Metropolis sampling

For a given ensemble of particles, the probability of the system to be in state i at time t can be evaluated using statistical physics as,

$$P_n(t) = e^{-H/k_B T}/Z \tag{4.18}$$

where H is the Hamiltonian of the system, k_B is the Boltzmann constant, and Z is the partition function of the system. The general form of Z for a classical system can be written as,

$$Z = \sum_{\text{all states}} e^{-H/k_B T}. \tag{4.19}$$

Physically, if one can find Z, then all thermal properties of the system including free energy, internal energy, entropy etc. can be calculated. However, this requires knowing all the possible states that the system can adopt, which is typically a gigantic value difficult to calculate. Instead of dealing with Z, one can use the

ratio of probabilities according to the Eq. 4.18,

$$P_n(t)/P_m(t) = \exp\left(-\Delta E/k_{\mathrm{B}}T\right) \tag{4.20}$$

where ΔE is the difference of the energy between the states n and m. Then the transition rate only depends of the exponential factor and no longer on Z. In theory, any transition rate that satisfies the detailed balance condition in Eq. 4.17 can be used in a Monte Carlo simulation. The first method was introduced by Metropolis et al. in 1953 and similar to the analogy in Eq. 4.20, it was calculated as,

$$\begin{aligned} W_{i\to j} &= \tau_0^{-1}\exp\left(-\Delta E/k_{\mathrm{B}}T\right), && \Delta E > 0 \\ &= \tau_0^{-1}, && \Delta E < 0 \end{aligned} \tag{4.21}$$

where τ_0 is the time to attempt the transition from state i to j, which is a constant and often set equal to unity. The Metropolis algorithm works in the following way,

(1) Start from a randomly generated initial state.

(2) Propose a move and consequently a transition in the system from one state to another.

(3) Calculate the energy change in the system ΔE

(4) If ΔE is negative, accept the change and let the system go toward the lower energy state.

(5) If ΔE is positive, accept the change with the probability of $\exp(-\Delta E/k_B T)$. In practice, if $\exp(-\Delta E/k_B T)$ is smaller than a randomly generated number r the move is accepted, otherwise rejected.

By performing these 5 steps multiples times, the system tries to find the majority of the phase space, by what is called importance sampling. Rather than randomly looking for possible states that the system can reside in, Eq. 4.21 leads the system toward the states that play the critical role in determining the thermodynamic properties.

4.3.4 Errors and possible problems

The main difficulty of the Monte Carlo simulations is to find the optimum way that system can reach equilibrium. The particular task of defining 'moves' plays an important role in whether the system can reach equilibrium or not. As mentioned earlier, a move can be defined as any change that leads to the transfer of the system from one state to another state. Moves should be carefully defined such that the system can visit all possible states of the system under study. If the system is not ergodic, then the calculated thermal averages will have systematic deviations from the correct values.

Another important factor is the number of times the moves are attempted. When performing a move, any site can be randomly picked and one of the moves, decided randomly are performed. For a given system of size $N \times M$, performing Monte Carlo moves $N \times M$ times is called one Monte Carlo step (MCS). This means that for a simulation that takes 1000 MCS, a majority of the sites are selected about 1000 times. Clearly, as the system size becomes larger, each MCS takes longer to perform. One needs to check the minimum number of MCS necessary to reach equilibrium at a given size. The total MCS depends on the complexity of the system and also the types of MC moves defined. Once it is confirmed that the system is in equilibrium, then thermal averages can be estimated. To have a correct assessment of thermal averages, the states where the averages are calculated must be uncorrelated. This means there should either be enough MCS difference between two states, that are kept for averages, to eliminate the correlation, or the averages are done on independent calculations with a different sequence of random numbers to avoid any correlation.

All simulations need to be carried out in finite size lattices. One important question that needs to be answered is the treatment of the boundary of the lattice. To avoid edge effects, I have adopted periodic boundary conditions (PBC), by wrapping the n-dimensional space to a torus of (n+1)-dimensional space. This means the first site in a row sees the last site in the row as a nearest neighbor site. The same is true for the top and bottom of a column or any other direction of an n-dimensional lattice. However, such approximation is subject to its own drawbacks and errors. This can be better understood with an example: if one attempts a change on the right-most side of the system, then not only the left most layer

but also further layers away from the boundary may be affected by the proposed change. In reality, even if interactions are short-ranged, after some MCS, the influence of a move on the boundary can reach the same site from the opposite side. This is what is called a finite size effect, and it can lower the accuracy and increase the error bars of the calculated thermal averages. To deal with finite size effects, one needs to check different system size cells , starting with a relatively small cell. Then increase the cell size and perform the same calculations and find the same thermal properties. This needs to be repeated until there is negligible difference between two different cell sizes. Ultimately, the goal is to have smallest possible cell (to reduce computational cost) that can capture the correct thermodynamic properties with no, or negligible, finite size effects.

Chapter 5

Oxygen vacancies on $SnO_2(101)$

5.1 Model Hamiltonian

The atomistic picture of the stoichiometric surface can be seen in Fig. 5.1, with one on-site, six two-body, one three-body and one four-body interactions with their magnitudes shown in Table 5.1. The interactions are labeled as $b(ij)$, $c(ijk)$ and $d(ijkl)$ referring to two-body, three-body and four-body interactions, respectively. The numbers in parenthesis correspond to the type of interactions as shown in Fig. 5.1. For example, $b(12)$ refers to the two-body interaction between two nearest vacancies along [010]. The most dominant term is the on-site at $+1.94$ eV, which is equivalent to the energy cost of forming an isolated oxygen vacancy and is endothermic. Among the two-body interactions, $b(12)$ and $b(13)$, which are along the [010] direction, are -0.79 and -0.31 implying the lower energy cost of forming vacancy pairs in the [010] direction compared to two isolated vacancies. On the other hand, three vacancies in the [010] direction has a repulsive interaction $+0.31$. The two-body interactions between the vacancies in the $[10\bar{1}]$ direction are repulsive, with the dominant case being the diagonal pair $b(15)$ at $+0.25$ eV and to a lesser extent $b(14)$ and $b(16)$ at $+0.08$ eV and $+0.07$ eV, respectively. However, in the presence of 4 vacancies in the form of a parallelogram (vacancies at 1,2,5,4), an additional four-body, strongly attractive term $d(1245)$ needs to be included in the model Hamiltonian. Clearly, isolated vacancies tend to be highly endothermic but one can see that multiple vacancies, depending on how they are distributed, can

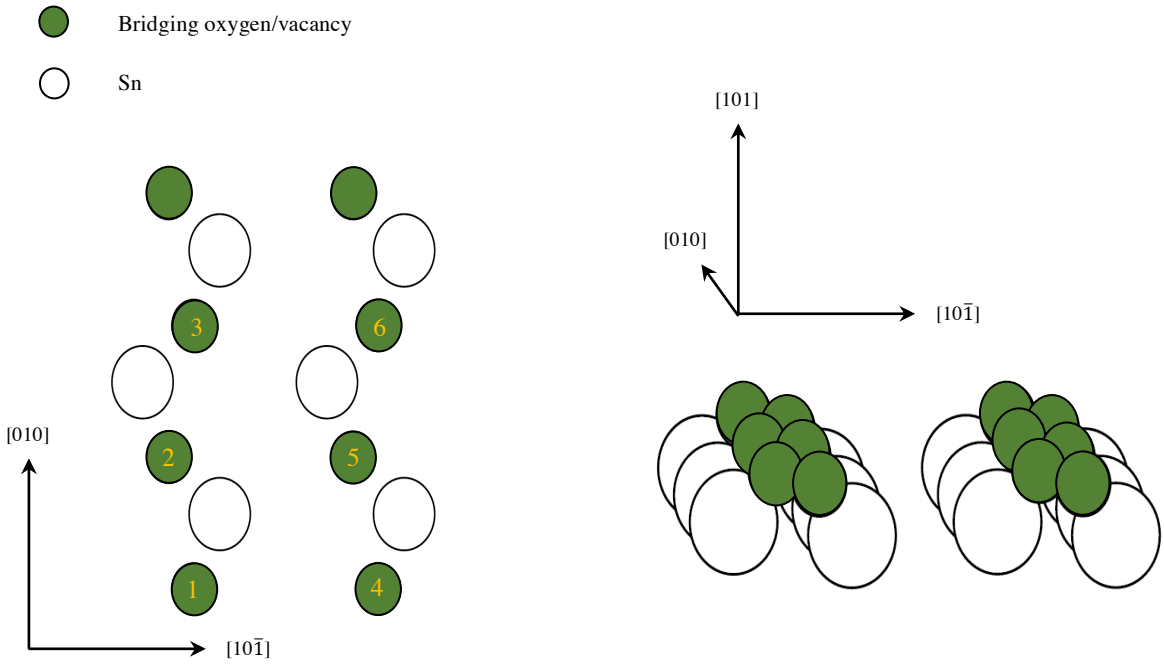

Figure 5.1: The top view and side view of $SnO_2(101)$ surface. The bridging oxygen atoms/vacancies are depicted as green, and tin atoms as white circles, respectively. The numbered bridging sites are shown to better understand the interactions as mentioned in Table. 5.1 of the system. For example, $c(123)$ corresponds to a 3-body interaction between vacancies created at sites 1,2 and 3.

either lower or raise the surface free energy. To test the accuracy of the model Hamiltonian with respect to the DFT calculations, a comparison between the two methods is shown in Fig. 5.2. The slope of the fitted line to the data points is 0.998, close to the exact answer of unity.

5.2 Vacancy Patterns

In order to obtain a reliable understanding of how vacancies form on the surface, we performed the MC simulations with the aforementioned model Hamiltonian. The concentration of vacancies start to in-

Table 5.1: The vacancy-vacancy interaction coefficients at the (101) surface of SnO_2. For higher order interactions, the coefficients are referred to as $b(ij)$, $c(ijk)$ and $d(ijkl)$ where i ,j, k and l refers to the numbered sites in Fig. 2.1. All interaction are in units of eV.

On-site	Interaction Energy (eV)
a	+1.94
Two-body	
$b(12)$	−0.79
$b(13)$	−0.31
$b(14)$	+0.08
$b(15)$	+0.25
$b(16)$	+0.07
Three-body	
$c(123)$	+0.30
Four-body	
$d(1254)$	−0.62

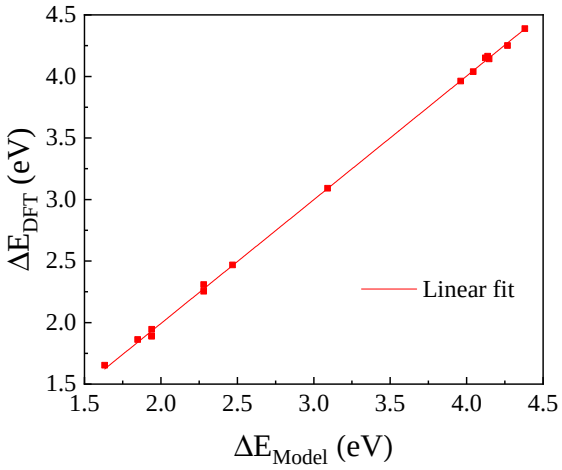

Figure 5.2: DFT calculations are compared with the model Hamiltonian predictions. The fitted line has a slope of 0.998, close to the exact value of unity.

crease with decreasing oxygen chemical potential at -1.14 eV, as shown in Fig. 5.3. This chemical potential is lower in magnitude than the cost to form isolated vacancies (-1.94 eV) which signals that multiple vacancies are easier to form than isolated ones. To see how the vacancies are formed at the surface, we depicted one example of a 40×30 unit-cell system after reaching equilibrium in MC in Fig. 5.4 (top view). One can notice that vacancies (orange squares) are formed in rows along [010], and the rows are mostly isolated. Going from -1.15 eV to -1.35 eV, the concentration of vacancies then increases slowly from 0.45 to 0.55. As shown in Fig. 5.4b, vacancies are at every other rows in the [010] direction. The fact that the system does not get fully reduced is due to the repulsion between rows of vacancies as mentioned earlier in Table. 5.1. The Sn atoms that are underneath the oxygen atoms are still in the $+4$ charge state but those underneath the rows of vacancies are in the $+2$ charge states, where they share electrons with 3 sub-atomic oxygen atoms. However, at -1.35, the chemical potential can overcome the repulsive terms in the model Hamiltonian and become fully reduced with all Sn atoms are in $+2$ charge state. According to Fig. 5.4c, vacancies cover the majority of the surface with a handful of isolated rows of oxygen atoms, in opposite to the behavior at -1.15 eV Fig. 5.4a, with isolated rows of vacancies. To test the reliability of these results, we performed an *Ab-initio* Thermodynamics analysis for three terminations, stoichiometric, partially reduced 2×1 and fully reduced 1×1 surface. The transition to the partially reduced and fully reduced surfaces are at -1.15 eV and -1.34 eV, respectively, in excellent agreement with -1.14 eV and -1.35 eV of model Hamiltonian prediction. However, the concentration level in the model Hamiltonian analysis for the partially reduced surface is not exactly 0.5 with 2×1 periodicity. It changes from 0.45 to 0.55, implying that in some regions of the surface, there are either two neighboring rows of bridging oxygen (0.45) or bridging vacancies (0.55). These situations can be viewed as defects relative to the pure 2×1 system studied with *Ab-initio* Thermodynamics.

Comparing with earlier theoretical works, Ab-initio Thermodynamics studies [33] found the 2×1 surface to be stable in a small region of chemical potential, from -1.7 eV to -2.0 eV [31], [37]. The width of this region is in good agreement with the width of our results, both Ab-initio Thermodynamics and model Hamiltonian. However, there is noticeable difference between the chemical potentials where transition

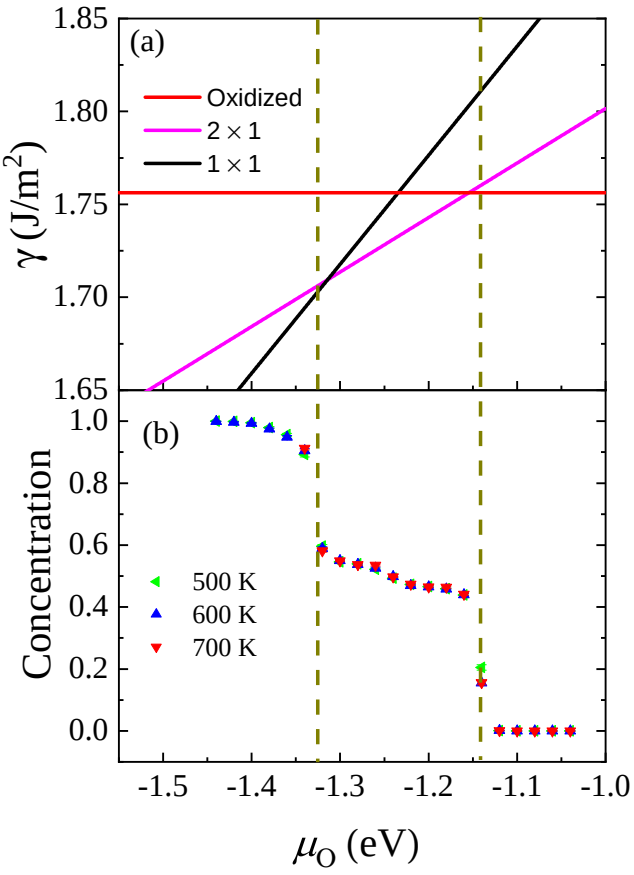

Figure 5.3: (a) Surface energy vs. oxygen chemical potential of three distinct surface are compared using *Ab-initio* Thermodynamics where the transition to 2×1 (half-reduced) and 1×1 (fully-reduced) surfaces occur at −1.14 eV and −1.32 eV, respectively. (b) Equilibrium concentration of vacancies at three different temperatures are shown as a function of chemical potential. There are two transitions at −1.15 eV and −1.35 eV. In the region between these two transitions, the concentration changes steadily, indicating that it is not a perfect 2×1 structure.

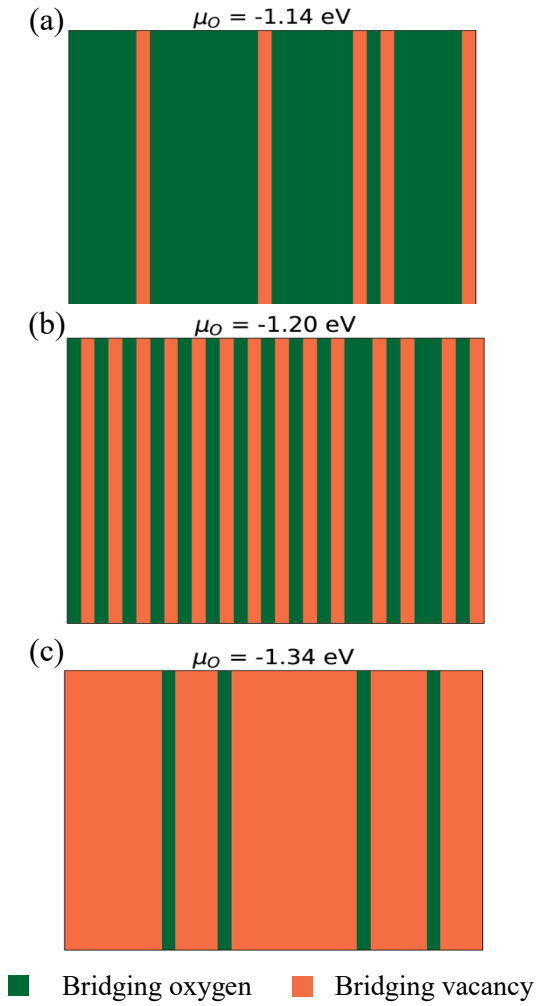

Figure 5.4: Bridging oxygen vacancies (orange) and atoms (green) are shown as a square for a supercell of 40×30 surface of (101). The pictures are top-view and are depicted as in Fig. 5.1, but without the tin atoms. Three scenarios are shown: (a) Transition to partially reduced surface with the creation of a small number of rows of bridging vacancies along [010].(b) Rows of vacancies appear one after another, but not perfectly uniformly. There are two adjacent rows of bridging oxygen atoms in the right region of the surface. (c) the transition to fully reduced surface is occurring with bridging vacancies covering most of the surface region. A few rows of oxygen atoms remain at this potential. All these pictures are a single shot taken after reaching equilibrium in MC simulations at 600 K.

occur ($\Delta\mu = 0.55$ eV). While there are several factors in DFT calculations that can contribute to this difference, the main reason lies in the type of exchange-correlation functional used. The previous authors performed all their calculations with PBE which tends to overestimate the formation energy.

Regarding the experiments done at the reduced (101) surface, it was reported that a 2×1 surface is harder to achieve, and the process is sometimes irreversible. Such a difficulty [31] can be related to the narrow chemical potential range where 2×1 is stable, which confirms our results.

5.3 System size

Periodic boundary conditions (PBC) at the edges of the system can lead to noticeable deviation from a correct estimation of an infinite surface. However, as the system size increases, the artificial influence of PBC will diminish. To better illustrate the importance of system cell size, a plot of vacancy concentration for four different cell sizes, 10×10, 20×20, 40×30 and 50×50 is shown in Fig. 5.5. For the smallest cell size of 10×10, even at chemical potentials as low as -1.5 eV, the vacancy concentration does not go above 0.88, severely underestimating the fully reduced surface. Moreover, the transition between the fully oxidized surface to the partially reduced surface is much smoother than the results discussed in earlier sections. The transition from the partially reduced surface to the fully reduced surface become so vague that it is hard to distinguish these two phases. Increasing the system size to 20×20 improve the estimations for the entire chemical potential range. However, there are still noticeable differences with respect to 40×30, especially in the region where the transition to the fully reduced surface occurs. Going beyond 40×30 does not significantly affect any features of the plot. Therefore, the 40×30 can be assumed as a safe estimate for an infinitely large surface area.

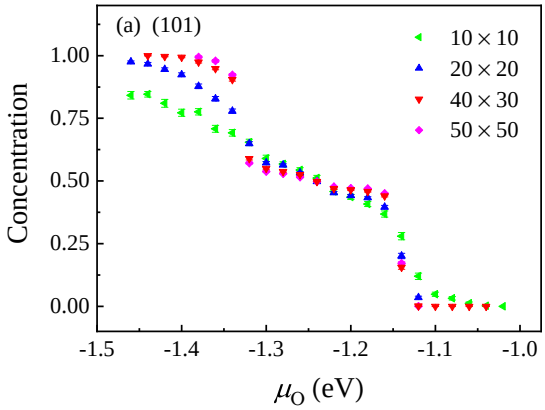

Figure 5.5: The vacancy concentration as a function of chemical potential for different surface sizes. The difference between the 40×30 and 50×50 is negligible, and the 40×30 system size can capture the properties of an infinitely large surface area.

Chapter 6

Oxygen vacancies on SnO_2(110)

6.1 Model Hamiltonian

A top view and sideview of the (110) surface termination in Fig. 6.1 shows that there can be two distinct types of vacancies, in-plane and bridging. After performing DFT calculations for a set vacancy configurations, one needs to compare the vacancy formation energy with earlier studies. In particular, isolated vacancies can be formed at +2.56 eV and +3.46 eV at bridging and in-plane sites, respectively. This is in good agreement with the corresponding values reported by Oveido *et al* [35] at +2.29 and +3.1, respectively. For systems with multiple vacancies, a scenario with every other row of in-plane vacancies has +2.61 eV formation energy per vacancy which is in agreement with the reported 2.27 eV. The systematic overestimation by 0.3 eV is due to comparing two studies with different exchange-correlation functional. The model Hamiltonian can be determined from the calculated DFT calculations, with the best-fit model coefficients shown in Table. 6.1. Similar to the discussion on the (101) surface, the type of interactions is shown as numbers in Table. 6.1 and Fig. 6.1. For the on-site interactions, one can see that bridging vacancies can form at +2.59 eV, significantly smaller than in-plane ones at +3.46. This implies that creating isolated bridging vacancies is considerably less costly that in-plane ones. However, accumulation of vacancies makes the prediction of the vacancy formation very complicated. Starting with the two-body interactions among the bridging vacancies, the nearest neighbor interaction along [001],

$b(12)$, lowers the energy by -0.21 and second nearest neighbor interaction, $b(13)$, increases the formation energy by $+0.08$. This means that bridging vacancies can form with lower formation energy along [001]. The remaining bridging/bridging interactions are less than 0.01 eV, meaning the interactions along bridging rows are relatively short range. On the other hand, the two-body interactions among in-plane vacancies are both stronger and extend further on the surface. In particular, there is a large attractive interaction between nearest neighbor (NN) in-plane vacancies ($b(47)$) at -1.57 and 2nd NN ($b(45)$) at -0.16. Moreover, the presence of three in-plane vacancies in the [001] direction adds another attractive interaction, c_{123} at -0.58. Similar to bridging vacancies, these interactions suggest that in-plane vacancies tend to form at much lower energy cost along [001] rows than in isolated form. The repulsive interaction between vacancies in diagonals ($b(48)$) at $+0.42$ and across the tin atom ($b(79)$) show the repulsion between rows of vacancies that are formed next to each other. Also, due to the complexity of arrangement of tin and oxygen atoms, one many notice that magnitude of interaction cannot be predicted based on the distance between them. In fact, $b(49)$ which is the seventh nearest neighbor interaction between the in-plane sites, is stronger in magnitude than 5th and 6th nearest neighbor (smaller than 0.01 and are not included in the model Hamiltonian). The remaining significant interaction are between in-plane and bridging vacancies. In sparticular, the two-body interaction $b(14)$ is repulsive at $+0.53$ but with the presence of third vacancy, a three-body interaction $c(124)$, is attractive at -0.62. The aforementioned parameters in the model Hamiltonian can predict the surface energies to within less than 2 percent of the DFT energies.

So far, the main difference between the (101) and (110) surfaces is in the number of types of interactions in the model Hamiltonian. According to the interaction parameters in Table. 6.1 , most of the higher order interactions are attractive, especially the nearest neighbor in-plane/in-plane interactions. Running the simulation with this Hamiltonian, we find that the surface abruptly reduces to a fully reduced surface at $\mu = -1.9$ eV, where all bridging and in-plane oxygen atoms are removed. Such a surface consists of only metallic tin atoms. While there is a small discussion of such a possibility [31] at temperatures higher

Table 6.1: The vacancy-vacancy interaction at the (110) surface of SnO_2. Higher order interactions are referred to as $b(ij)$, $c(ijk)$ and $d(ijkl)$ where i ,j, k and l refer to the numbered sites in Fig. 6.1. Note that there are three types of two-body interactions.

On-site	Interaction Energy (eV)
Bridging	+2.59
In-plane	+3.46
Two-body	
Bridging/Bridging	
$b(12)$	−0.21
$b(13)$	+0.08
In-plane/In-plane	
$b(47)$	−1.57
$b(45)$	−0.16
$b(48)$	+0.42
$b(79)$	+0.53
$b(49)$	−0.05
Bridging/In-plane	
$b(14)$	+0.53
$b(17)$	−0.05
Three-body	
$c(124)$	−0.62
$c(127)$	−0.07
$c(278)$	−0.08
$c(456)$	−0.58

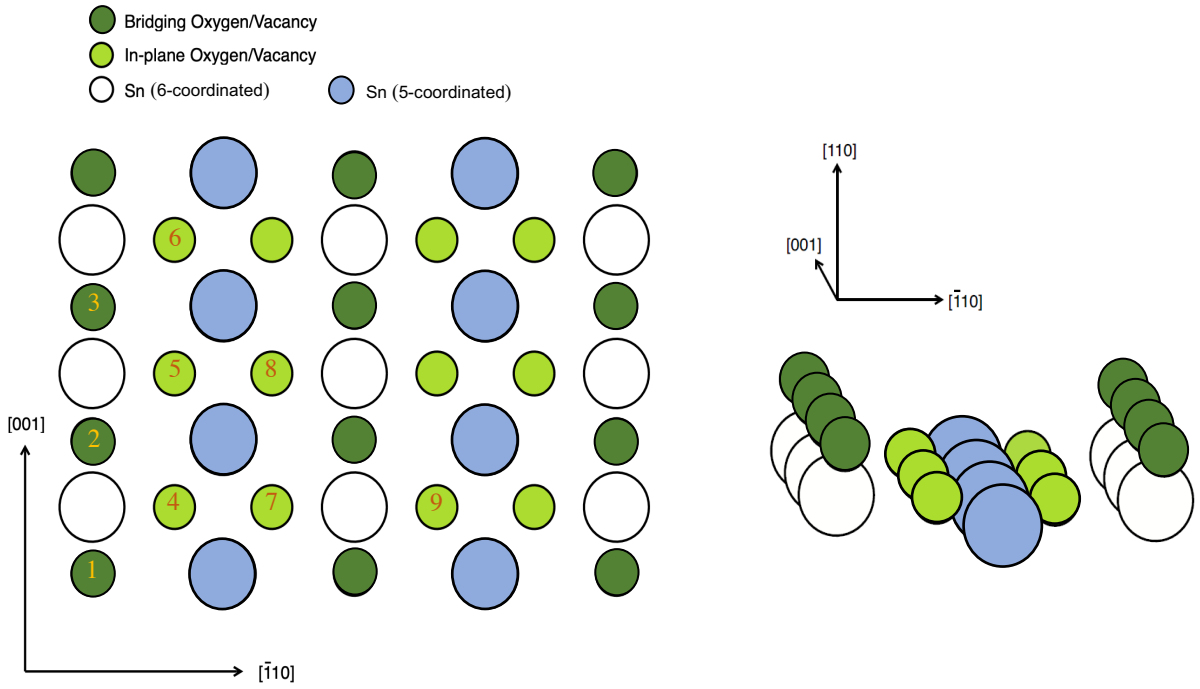

Figure 6.1: The SnO_2 (110) surface is depicted in top-view and side-view. Bridging oxygen/vacancy, in-plane oxygen/vacancy, 5-coordinated tin and 6-coordinated tins are shown in light and dark green, blue and white circles, respectively. The numbers on some bridging/in-plane sites are shown to better understand the higher order interactions mentioned in Table. 6.1.

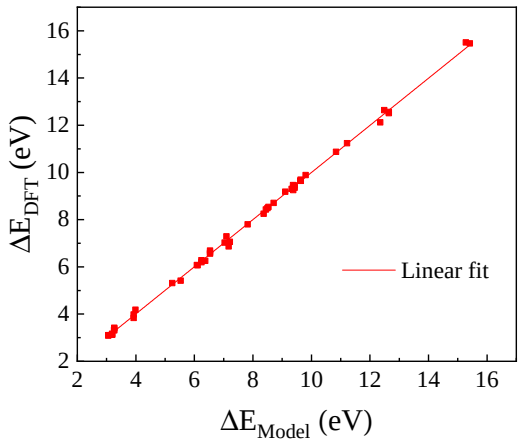

Figure 6.2: The DFT calculations are compared with the model Hamiltonian predictions for the (110) surface termination. The fitted line has a slope of 0.98 implying an accurate prediction of the model Hamiltonian.

than 900 K, there is no evidence of seeing a metallic surface at milder temperatures. Reconstructions at high temperatures have been observed by other studies, and the current model, with the consideration of only oxygen vacancies, cannot predict scenarios with interstitial tin atoms. Therefore, the main focus of the present study would be on the temperature ranges where reconstructions are unlikely to occur (400 K - 700 K). To restrict the system from turning into a metallic tin or undergoing major reconstruction, changes need to be applied to the model Hamiltonian. To gain insight into the main precursors of the reconstructions, we performed additional DFT calculations with relatively high vacancy concentration (>0.6). Of all the configurations considered, in the majority of cases, when all four in-plane vacancies surrounding five-coordinated Sn (shown in Fig. 6.1) are present, significant reconstructions appear. For example, bridging oxygen atoms (if present) bend toward the in-plane vacancies and become stable in interstitial positions that are neither in-plane nor bridging sites. Also, the five-coordinated tin atoms are single coordinated to a sub-bridging oxygen atom, meaning that it is in +2/3 charge state. Such a charge state is much smaller than stable tin atom dual vacancy charge states +4 or +2 and is the main reason that the surface undergoes reconstructions. Thus, by defining a four-body highly repulsive interaction between the in-plane vacancies labeled as 4, 5, 7, 8 in Fig. 6.1, the majority of reconstruction cases can be avoided. Consequently, during MC simulations, the system will never visit such a highly repulsive scenario, and as it is shown later, a fully reduced surface with metallic tin cannot be achieved. Note that this 4-body interaction is fictitious, and its magnitude is an arbitrary value, large enough to avoid the formation of such configuration in the desired range of chemical potential.

To check the accuracy of the model Hamiltonian with respect to the DFT calculations, a comparison between the two methods is shown in Fig. 6.2. The slope of the fitted line to the data points is 0.98, close to the exact value of unity. The atomistic picture of each of these configurations are provided in Appendix B.

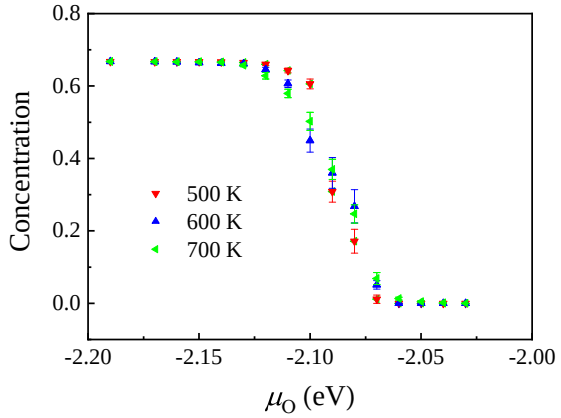

Figure 6.3: The concentration of vacancies at three different temperatures are shown as a function of the chemical potential. There is a single transition from the oxidized to the reduced surface at around -2.1. Details of vacancy morphologies are detailed in Fig. 6.4

6.2 Vacancy Patterns

The plot of the vacancy concentration level as a function of oxygen chemical potential, in Fig. 6.3, shows a single transition from the fully oxidized surface to the reduced surface at around -2.1 eV. This is in direct contrast to the (101) surface where three regions of reduced surfaces were observed. Three examples of surface configuration for a system size of 40×30 are depicted in Fig. 6.4. At $\mu = -2.07$ eV, vacancies tend to form as cluster of in-plane and bridging vacancies. This means that even in the beginning of the surface reduction, in-plane and bridging vacancies are likely to form together. At the transition level ($\mu = -2.09$ eV) the same cluster patterns become elongated in the [001] direction. As the reservoir goes toward to a more oxygen deficient conditions (i.e. lower chemical potential), the vacancy concentrations reach a relatively constant values of 0.66. with one example illustrated at $\mu = -2.15$ eV in Fig. 6.4c .

Fig. 6.5 shows an enlarged view of configurations in Fig. 6.4c. It highlights four different types of vacancy patterns that constitutes the most region of vacancies in Fig. 6.4. In case (1), every other row of in-plane vacancies are formed to the right side of bridging vacancies. Using mirror plane symmetry along [001] results in the case (2) where in-plane vacancies are formed to the left of bridging vacancies. These

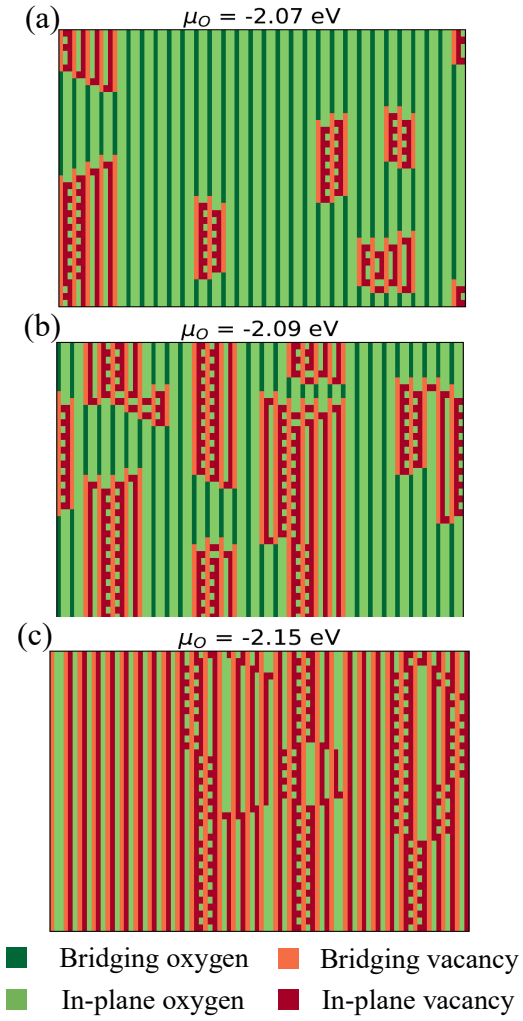

Figure 6.4: Bridging and in-plane oxygen vacancies and atoms are shown for a supercell of 40×30 surface of (110). Similar to (101) termination, these are single shot pictures of the surface in equilibrium and large scale depiction of Fig. 6.1. Three scenarios are shown: (a) the start of vacancy formation with the creation of clusters of vacancies consisting of both bridging and in-plane vacancies at $\mu = -2.07$ eV, (b) at the transition with clusters spanning vertically across the surface ([001]) at $\mu = -2.09$ eV, (c) the reduced surface after the transition at $\mu = -2.15$ eV. The number of vacancies remains the same for any lower chemical potential as shown in Fig. 6.3.

are exactly what other theoretical studies predicted for the (110) surface vacancies in equilibrium [33]. One main reason for observing cases 1 and 2 is because 5-coordinated and 6-coordinated tin atoms are share electrons with only 3 oxygen atoms in these scenarios; therefore, the tin atoms are in the +2 charge state. There would be no difference between cases (1) and (2) if the surface is made up of only one of them but not both. The main advantage of the model Hamiltonian approach is that one can study a large enough surface with both case (1) and (2) present in different regions of the surface. The grain boundary between them results in case (3) and case (4). Case (3) is when rows of in-plane vacancies are facing each other as if case (1) is to the left of case (2). On the other hand, case (4) is when in-plane vacancies are facing each other as if case (2) is to the left of case (1). So, the way that case (1) and case (2) approach each other determine whether case (3) or case (4) is created. Physically, the formation of case (3) is the direct consequence of two-body interaction $b(79)$ where two rows of in-plane vacancies are too costly to form across the rows of six-coordinated Sn atoms. Similarly, the zipper pattern in case (4) is again due to $b(79)$ across the bridging vacancies, together with strongly attractive $b(47)$. This pattern has some similarities with some earlier experimental works on this surface. It should be mentioned that rarely, isolated cases with in-plane vacancies on both sides of bridging vacancy appear but they are too energetically costly ($b(79)$) to cover a significant portion of the surface. The rest of the patterns not discussed in detail covers only a small region of the surface at all chemical potentials and some are due to the stochastic nature of the simulations.

6.3 Stability of the Patterns

Given that there is atomistic experimental pictures to compare the results, one may question the stability of surface energy at large scale. Especially case 4 may be attributed to the presence of the fictitious four-body interaction that we discussed earlier, or in another words, it may be an artifact of the model Hamiltonian. To see how such patterns behave at the DFT level, we performed a DFT calculation on a 2×4 unit-cell consisting of both cases 3 and 4 as shown in Fig. 6.6. This is the smallest unit-cell that can have all four cases at the same time. Not only there was no reconstruction during the relaxation in the DFT calculation, but the calculated surface energy matched the prediction of the model Hamiltonian to within less than

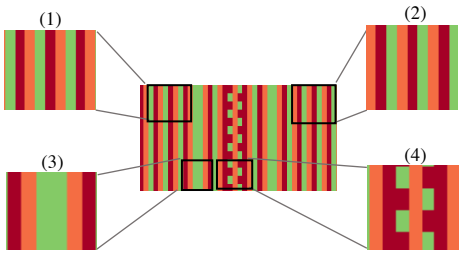

Figure 6.5: Enlarged reduced surface of (110) termination is made up of four different patterns labeled as 1 to 4. The cases 1 and 2 are identical under mirror plane symmetry along [001] but can create two types of grain boundaries depending on how they approach each other. When case 1 is to the left of case 2 (1-2), case 3 is created and if case 2 is to the left of the case 1 (2-1), case 4 is created.

0.5 percent. Such great agreement suggests that both cases 3 and 4 are real and are likely to be present at the surface. Also, the coexistence of 4 different patterns at the surface at low chemical potential shows the complexity of the surface and might give us more hints into why a fully reduced surface is difficult to achieve at (110) termination.

6.4 System size

Similar to the case of (101) surface, tests should be made on different lattice sizes to ensure that finite size effects are not influencing the interpretation of the results. A plot of vacancy concentration for three different cell sizes, $10 \times 10, 20 \times 20, 40 \times 30$ is shown in Fig. 6.7. For the smallest cell size of 10×10, the transition from the oxidized surface to the reduced surface is unrealistically smooth, such that vacancies start at higher chemical potentials (2.02 eV) and it takes noticeably lower chemical potential to reach the 66 % reduced surface (2.17 eV) when compared to larger sizes. Moreover, the error bars are much larger in size implying lower precision in the results. Increasing the system size to 20×20 improves the estimations for the entire chemical potential range. However, the difference between 20×20 and 40×30

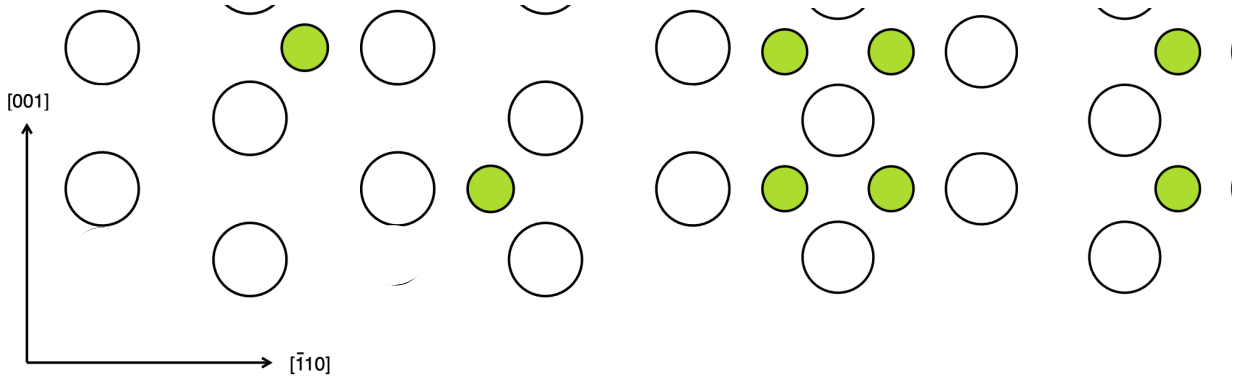

Figure 6.6: A 2×4 unit-cell consisting of both cases 3 and 4 as shown in Fig. 6.6. All bridging oxygen atoms are removed and only a handful of in-plane oxygen atoms are remained at the the surface.

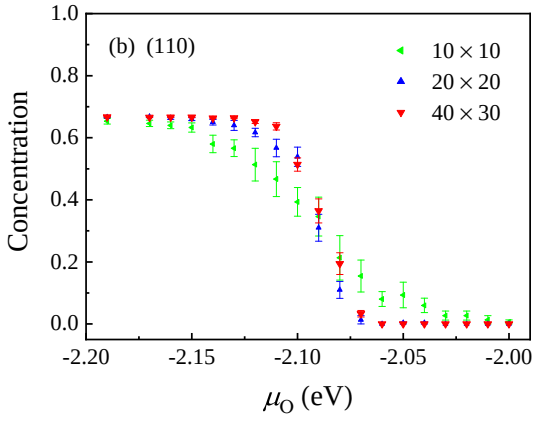

Figure 6.7: The vacancy concentration as a function of chemical potential for different surface sizes. The difference between 20×20 and 40×30 is small and for the safety of the analysis, 40×30 system was used throughout this chapter.

sized system is only evident at the transition but it can still be regarded as negligible, when compared to the behavior of the 10×10 cell. Therefore, in all the results mentioned in earlier figures, simulations were done with system size of 40×30 to minimize any finite size effects in the results.

Chapter 7

Oxygen vacancies on Pd-doped $SnO_2(101)$

7.1 Model Hamiltonian

Having studied vacancy interactions on pure SnO_2 surfaces, we now turn our attention to the (101) surface with Pd dopants. The top-view and side-view atomistic picture of this surface can be seen in Fig. 7.1. Given that we are only interested in the bridging oxygen vacancies, only the outermost layer of the surface is depicted. A Pd atom (black circle) is substituted for a Sn (white) with negligible changes in the surface relaxations. Some oxygen/vacancy sites are numbered to better understand the possible type of two-body, three-body or four-body interactions. In a pure system with no dopants (chapter 5), it was shown that 8 parameters, including a single on-site, 5 two-body, one three-body and one four-body interaction are enough to estimate the vacancy formation energy with high accuracy. These parameters are listed in Table. 7.1. One can notice a strong attractive interaction along [010] with **b(12)** $= -0.623$ and **b(15)** $= -0.169$. On the other hand, there is a general trend of repulsive interaction between rows of [010] along $[10\bar{1}]$, with the most dominant one being the diagonal interaction **b(14)** $= +0.175$. These values are in accordance with our earlier study on the pure SnO_2. The main reason we have slightly different results

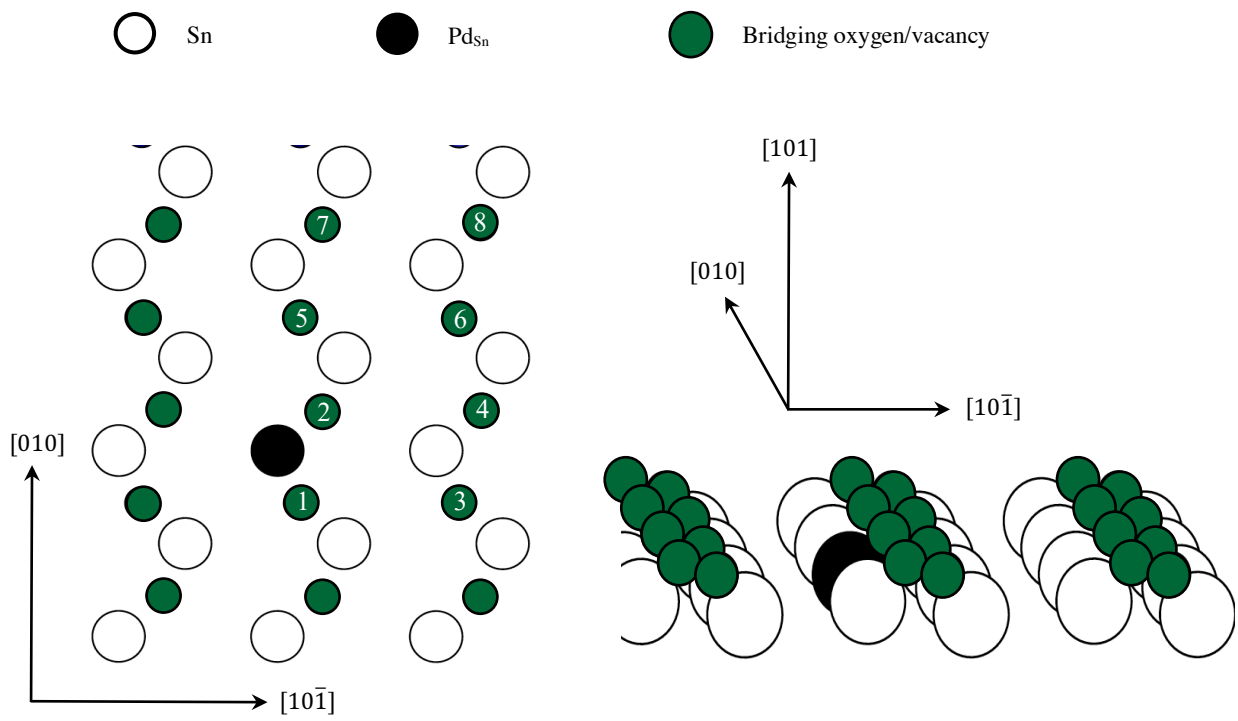

Figure 7.1: Top view and side view of the Pd-doped SnO_2(101) surface. The bridging oxygen atoms/vacancies are depicted as green, tin atoms as white circles, and Pd atom as black circle, respectively. The numbered bridging sites are shown to better understand the interactions as mentioned in Table. 7.1 of the system. For example, $c(123)$ corresponds to a 3-body interaction between vacancies created at sites 1,2 and 3.

for the pure system in the present study is due to having a larger set of DFT configurations (both doped and pure system) in determining the parameters.

By substituting one Sn atom for a Pd atom, 10 additional interactions are added to the model Hamiltonian; their best fit values are shown in italic and with prime, in Table. 7.1. With regard to the on-site term, creating a vacancy at either sites 1 or 2 in Fig. 7.1 lowers the formation energy by 0.459 eV. This means isolated vacancies can be formed easier in the presence of Pd. However, the major influence of Pd can only be captured with higher order interactions. Most of the corrections for two-body interactions correspond to the identical type of interactions in the pure system. For example, in a pure system, the first NN vacancy-vacancy interaction **b(12)** is identical to **b(25)** or **b(34)** (see Fig. 7.1). However, on the

Table 7.1: The vacancy-vacancy interaction of the Pd-doped (101) surface of SnO_2. The higher order interactions are referred to as $b(ij)$, $c(ijk)$ and $d(ijkl)$ where i,j, k and l refers to the numbered sites in Fig. 2.1. The interactions that belong to the pure system are shown in bold, the Pd influenced terms are shown in italic with a prime. All interaction are in units of eV.

On-site	Interaction Energy (eV)
a	+1.925
a'	-0.459
Two-body	
b(12)	−0.623
b(13)	+0.086
b(14)	+0.175
b(15)	−0.179
b(16)	+0.027
$b'(12)$	−0.731
$b'(25)$	−0.169
$b'(14)$	−0.662
$b'(26)$	−0.256
$b'(45)$	−0.053
$b'(58)$	−0.128
$b'(76)$	−0.033
$b'(43)$	−0.156
Three-body	
c(123)	+0.045
$c'(123)$	+0.531
Four-body	
d(1234)	−0.424

Pd-doped surface, as can be seen in Table. 7.1, these three interaction are significantly different due to the anisotropic influence of Pd. In particular, $b'(12)$ at -0.731 eV is more than 4 times attractive than $b'(25)$ at -0.169 eV. Likewise, there are 5 distinct diagonal interactions that were degenerate on the pure surface (**b(14)**). Depending on the geometrical position of Pd with respect to these diagonal interactions, the corrected diagonal interaction can be highly attractive as in $b'(14)$ at -0.662 eV or almost negligible far from the Pd as in $b'(76)$ at -0.033 eV. However, it was found that many of the diagonal interactions, up to 10 away from the Pd, are influenced and should be taken into account in the model Hamiltonian.

After testing all types of distinct diagonal interactions, it is found that some have differences lower than 0.01 eV. For example, while the $1,4$ and $2,3$ pairs are positioned differently with respect to Pd, they are considered as the same type of interaction, corresponding to the average of their formation energies, since their interaction coefficients are nearly identical. We applied this type of approximation to most diagonal two-body interactions whenever the difference was less than 0.01 eV. Otherwise, there would have been 8 more interaction in the model Hamiltonian, deteriorating its predictive power with the fixed number of input configurations. Regarding the three-body interaction, $c'(125)$ is extremely repulsive in the doped system at $+0.5331$ eV. This interaction compensate the strong attractive two-body correction $b'(12)$ and $b'(25)$ along $[010]$. Other interactions, including the two-body **b(13)** and four-body **d(1243)** are found not to be influenced by the presence of the Pd or their influence is already captured in the rest of the corrected parameters.

In general, it can be seen that most of corrected terms in H_{Pd} are attractive, meaning that vacancies are easier to form with the presence of Pd. Also, at least 8 distinct DFT calculations were performed at relatively large 5×2 or 3×3 surface super-cell to find the farthest distance the Pd can influence the two-body interaction. All confirm that the diagonal interaction along $[010]$ have a longer range of influence than in $[10\bar{1}]$ direction. In particular, in Fig. 7.1, the diagonal interaction of site 4 with the neighboring site to the right (not shown in the figure) is negligible while $b'(76)$ is not. To have consistency in the creation of the model Hamiltonian, all those scenarios, even cases that Pd does not influence the vacancy formation

energy are included in the model Hamiltonian. In fact, this is the main reason why some interactions for the pure system are slightly different from our earlier study on the pure surface of (101).

To check the accuracy of the model Hamiltonian approach in predicting energies, the predicted energies are plotted together with the DFT predictions in Fig. 7.2 where each vacancy configuration is shown with a red square. The solid line corresponds to a linear fit to all the configurations with a slope of 0.998. This value is very close to the exact value of 1 (perfect fit of model Hamiltonian to DFT), confirming the accuracy of the model. One may notice that the majority of configurations in the training set for model are below 5 eV. This is mostly due to the fact that most configurations had either a single or double vacancies, resulting in relatively lower formation energy than cases with multiple vacancies. The problem with having multiple vacancies is the appearance of reconstructions. The unit-cells of 3×2 and 4×2, can accurately predict many of two or three vacancies, but going beyond 60 % vacancy concentration can accidentally put the system in an unstable state which results in reconstructions. Further discussion on the influence of the model Hamiltonian and its parameters on the physical outcome of the Monte Carlo simulations, and consequently our interpretation of the results, are provided later in chapter 8.

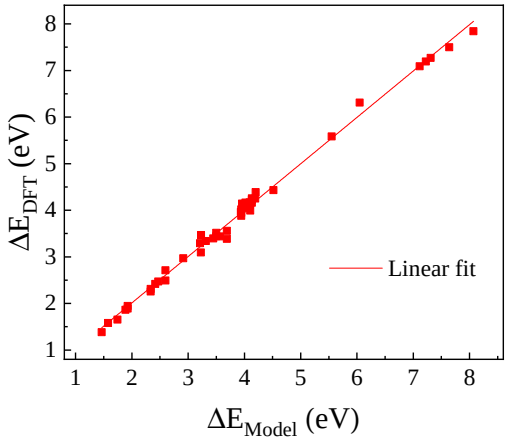

Figure 7.2: The DFT calculated energy as a function of model Hamiltonian prediction with parameters given in Table. 7.1. Each square point corresponds to a unique configuration of vacancies, performed at the DFT level. The solid line is the linear fit to all the square points with a slope of 0.998.

7.2 Vacancy patterns

Based on the many noticeable attractive interactions in the Pd-doped system in Table. 7.1, we anticipate that vacancies can be formed at higher chemical potentials. This hypothesis is systematically analyzed for a range of oxygen chemical potential and for different Pd dopant concentration in Fig. 7.3. For the pure surface (black squares), the system reduced at -1.15 eV, as expected and predicted in chapter 5. However, there are two major changes as the Pd concentration increases: (1) the vacancy concentration shifts toward higher values at almost all the chemical potential ranges, and (2) the maximum chemical potential necessary to have stable vacancies shifts toward less negative values. For example, even at the smallest Pd concentration of 0.5 %, vacancies can have a concentration of 10 % between -1 eV to -1.15 eV, a noticeable shift from zero concentration of the pure system. Also, vacancies can be formed at chemical potentials as high as -0.75 eV, about 0.4 eV higher than the maximum chemical potential value for the pure surface. To have better physical understanding of the these chemical potentials, the top axis shows the corresponding partial pressure of O_2 at a fixed temperature of 600 K. So -0.75 eV corresponds to approximately 0.1 atm, which means vacancies can be stable close to room pressure (≈ 0.2 atm).

To get an idea of the morphology of the vacancies in the presence of Pd, several regions of chemical potential, where noticeable changes in the vacancy concentration occurs, are investigated in Fig. 7.3 (dashed lines). The first corresponds to the early stages of vacancy creation around -0.9 eV to -1.1 eV. Several snapshots for a Pd concentration of 1.5 % are shown in Fig. 7.4. Each depicted pattern corresponds to individual simulations done at fixed concentration of Pd atoms, with the same distribution of Pd. At each chemical potential, the simulations were performed independently. To see the influence of the dopants, only the Pd doped sites (black squares), oxygen atoms (green square) or vacancies (orange square) are shown. The Sn atoms, located between the oxygen atoms/vacancies, are not shown to make the figure less crowded. The snapshots are examples of single MC simulations at equilibrium for a 30×30 system size. At a chemical potential of -0.9 eV, Fig. 7.4a shows that vacancies start to form as clusters surrounding the Pd atoms. This pattern is driven by the highly attractive $b'(12)$ and $b'(14)$ coefficients in Table 7.1.

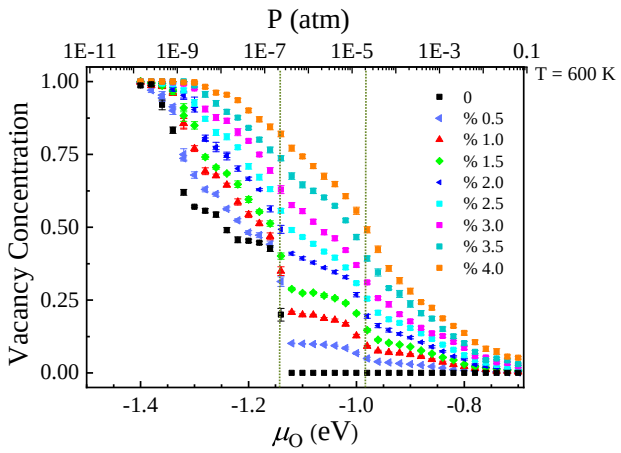

Figure 7.3: Oxygen vacancy concentration as a function of chemical potential at different Pd dopants concentrations. Every point in the figure is an independent MC calculation performed with different initial seed, at a fixed temperature of 600 K for 2000 MCS. The top horizontal axis is the equivalent pressure in atm at temperature of 600 K. The dotted vertical lines are at the transitions to a reduced surface, which are further discussed in the text.

As the chemical potential decreases and the reservoir becomes more oxygen deficient, clusters become larger and in some regions merge with other clusters. This is where other less attractive terms in the model Hamiltonian become favorable. Interestingly, this increase in the size of the clusters is also visible in Fig. 7.3 (vertical dashed line) as a shoulder appears around -1 eV. To understand this phenomenon, consider the total diagonal interactions including both the pure system interaction (**b(13)**) and corrected Pd-doped interactions. The shoulder appears when the system can overcome the barrier coming from the the repulsive diagonal terms of the pure system. In the absence of the Pd dopant, both the on-site term and the diagonal interaction are strongly repulsive (0.18 eV) such that no vacancies can appear at the surface.

The second region of interest is the appearance of a flat region from -1 eV to -1.15 eV at low concentration of Pd ($< 2\%$), where the population of vacancies is mostly unchanged. This can be explained by vacancy clusters reaching the maximum possible radius. In other words, Pd dopants can influence the creation of vacancies up to a certain radius of 10 Å.Therefore, at -1 eV, essentially all clusters of vacancies have reached that effective radius. This can be visualized in Fig. 7.4d, where in most cases, up to 3

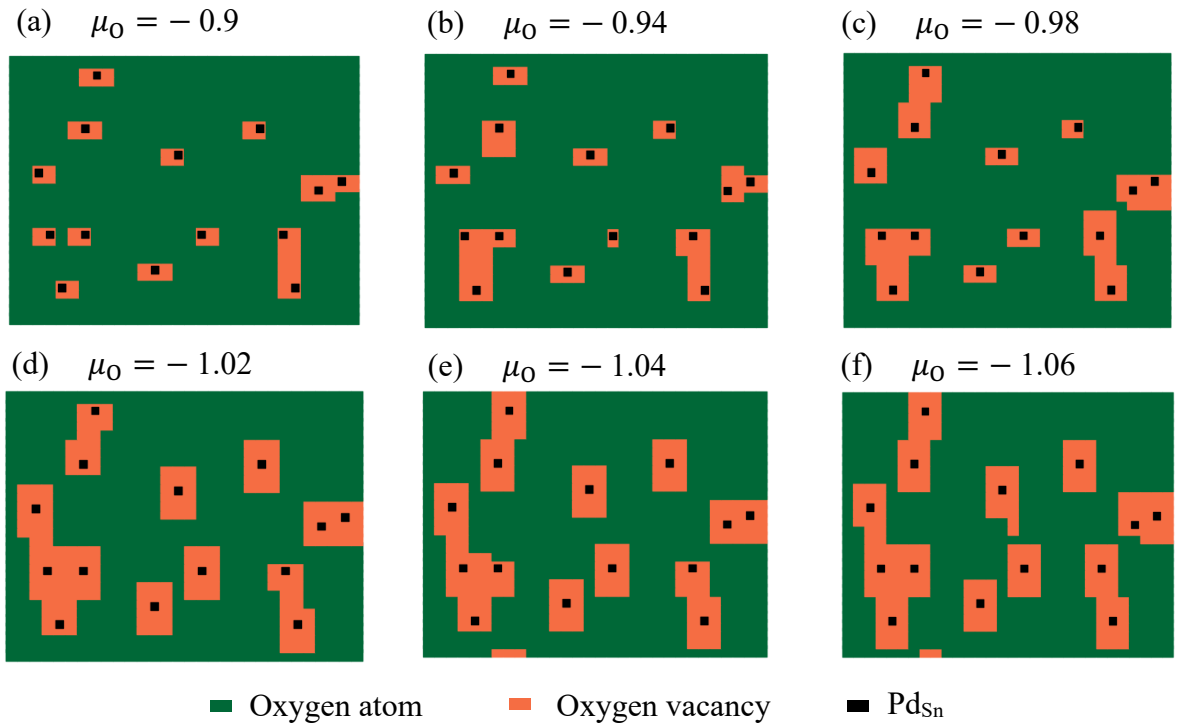

Figure 7.4: The top-view of the 30×30 surface with a fixed Pd concentration of 1 %. The oxygen atoms are shown as green squares, oxygen vacancies as orange squares, and the Pd dopants as black squares. From (a) to (f), the Pd distribution is kept constant while varying the oxygen chemical potential from -0.9 eV to -1.06 eV. Each snapshot is done independently with a different initial concentration of vacancies.

rows of vacancies are formed above and below the Pd atom for isolated clusters. The difference between Fig. 7.4d-f remains rather small. For higher concentration of Pd ($> 2\%$), the flat region no longer exist, a linear change of concentration appears in Fig. 7.3, with the incline becomes larger in magnitude as the Pd concentration increases. This can be explained by the fact that at low concentration, the Pd atoms are well separated from each other so that oxygen vacancies are created in form of islands around the Pd dopants. At higher concentration, due to the abundance of Pd atoms at the surface, islands of vacancies around each Pd atom overlap. There are examples of both isolated islands and overlapped cases in Fig. 7.4. At even higher concentration $> 3\%$, the majority of surface sites are within the effective interaction region of some Pd dopants and formation of vacancies become less energetically costly. It should be mentioned that 4% is already considered a noticeably high concentration of Pd, and going beyond that would make the system unrealistic and unreliable based on the design of the model Hamiltonian model. This is mainly due to the fact that experimental doping concentration is low (even less than 1%), and at high concentration of Pd, surface reconstructions may occur. Reconstructions, which typically involve atoms to be in interstitial sites, are not included in the model Hamiltonian, making the model mostly unreliable at unrealistically high concentration of Pd.

Another interest region of chemical potential is close to the transition for the pure surface. It can be seen that at -1.15 eV, there is clearly a sudden transition to a more reduced surface for Pd $< 2\%$. This can be understood from the intrinsic reduction behavior of the pure (101) surface, which was shown in our earlier studies to form vacancies at -1.15 eV. These vacancies were created in the form of rows along the [010] direction and cover almost every other row of the sites (defective 2×1 pattern) as shown in Fig. 5.4. Such patterns of vacancies can be explained by the highly attractive **b(12)** and **b(15)**. With the presence of Pd, clusters of vacancies appeared at lower chemical potential, mixed with the underlying pattern of vacancies, as shown in Fig. 7.5. At low Pd concentration of 0.5%, the dominant behavior of the surface is governed by the pure surface, with the appearance of the rows of vacancies along [010]. As Pd concentration increases, clusters become the dominant form of vacancies, and the intrinsic coverage is less clear. This results in a higher increase rate in the concentration of vacancies for the doped systems

in Fig. 7.3. An example of 4 % Pd shows the highly defective surface made of mostly clusters of vacancies, with some scarce patterns of the rows of vacancies appearing in some regions of the surface. The reason that rows of vacancies appear at the same chemical potential as in the pure system lies in the fact that vacancies that are not in the vicinity of the Pd atoms fully follow the intrinsic behavior of the pure system.

Reducing the chemical potential to more oxygen deficient conditions leads to another transition, close to -1.3, to a fully reduced surface. In this case, for the pure system, the surface is mostly covered by vacancies with a few rows of oxygen atoms. Therefore, the presence of Pd does not significantly change the behavior of vacancies, which have already covered the majority of the surface. Also, at such a high concentration of vacancies, the presence of Pd may lead to surface reconstructions or some long-range relaxations. Therefore, at these extremely low chemical potentials, surface morphologies should be taken with a grain of salt and further analysis/tools are required to provide a reliable picture

7.3 System size and temperature

Due to periodic boundary conditions in the MC simulations, finite size effects are present, and one needs to choose a large enough surface to exclude them. To investigate the influence of the system size, several different system sizes have been studied for a fixed Pd concentration of 1.5%. The vacancy concentration for each system size is plotted as a function of oxygen chemical potential in Fig. 7.6. This figure shows that the 20×20 system is noticeably different from the 30×30 and larger systems and has larger error bars. The negligible difference between the 40×40 and 50×50 system indicates that 40×40 is large enough to model an infinitely large surface of Pd-doped Sn (101).

The other main parameter in the MC simulations is the temperature which is set fixed at the beginning of the simulations. Theoretically, the overall behavior of the system depends on the chemical potential, which itself is a function of temperature and pressure. However, if one uses a different temperature for the simulations, the corresponding pressure would also change such that the chemical potential is unchanged. While the energy change is not related to the temperature, the Boltzmann factor in the Metropolis sampling is proportional to the exponential of the negative inverse of the temperature. This

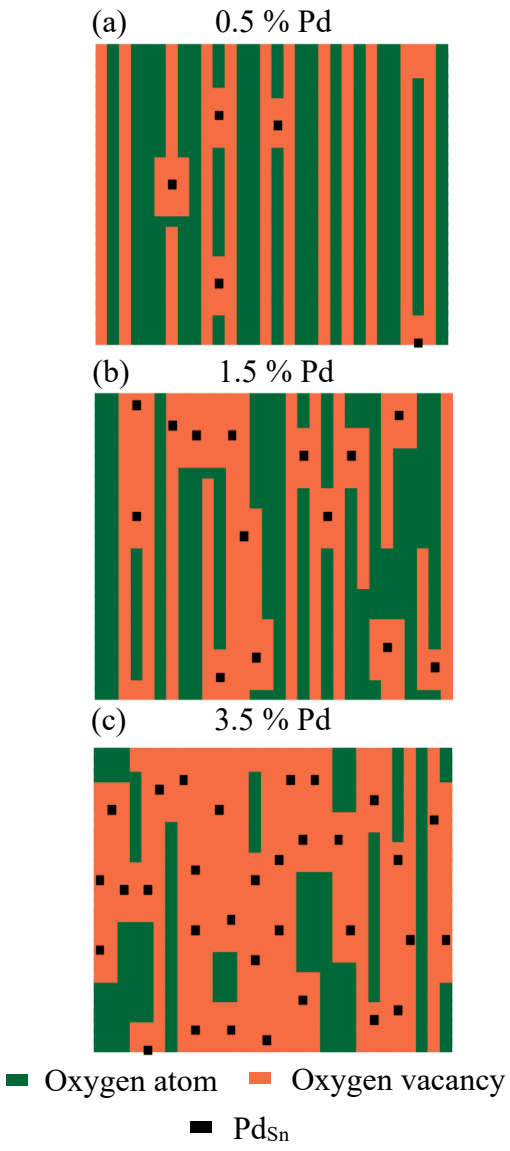

Figure 7.5: The top-view of the 30×30 surface with a fixed chemical potential of -1.15 eV at three different Pd concentration (a) 0.5%, (b) 1.5%, and (c) 3.5%. The oxygen atoms are shown as green squares, oxygen vacancies as green squares, and the Pd dopants as black squares, respectively.

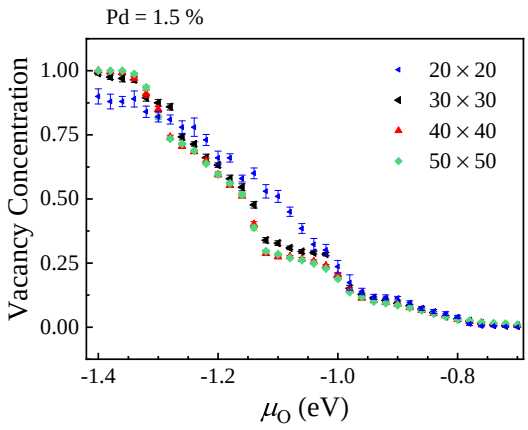

Figure 7.6: Oxygen vacancy concentrations vs. chemical potential at a fixed Pd concentration of 1.5% for varying super-cell sizes. Finite-size effects are present at the smallest system size of 20×20 but vanish at 40×40 cell size.

means that at low temperatures, MC moves are more likely to be rejected than at high temperatures. Our analysis in Fig. 7.7 shows that in all ranges of 400 K to 700 K, the results are within the errors of one another, and hence there is no systematic difference between the cases. For the lowest temperature, 400 K, the number of MC steps was three times greater than for the case of 700 K, to ensure the system reaches equilibrium.

7.4 Error in model Hamiltonian

There are certain limitations with the model Hamiltonian approach that needs to be addressed. In particular, the range of vacancy-vacancy interaction may go beyond $6th$ NN. By performing a DFT calculations for an isolated vacancy in a 5×2 supercell, it is found that the contribution of two-body interactions farther away is less than 0.01 eV, within the threshold of the present study. Another possibility would be the occurrence of reconstructions, as mentioned in the previous chapter, which can make the results unreliable. In all the test simulations of our DFT results, the relaxations of either Pd, Sn, or O atoms were less than 0.1 Å and no reconstructions were observed. The structures found from MC simulations are based

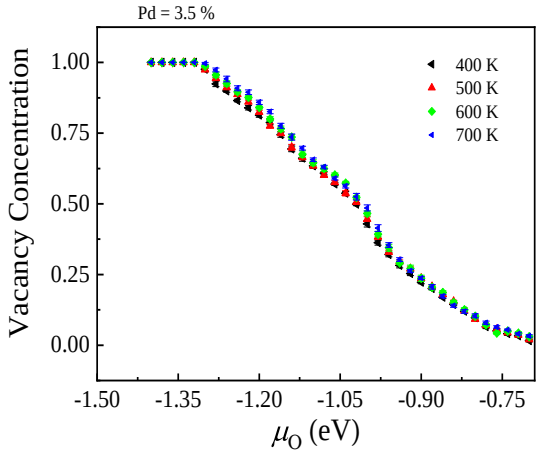

Figure 7.7: Oxygen vacancy concentrations at a fixed Pd concentration of 1.5 % at varying temperatures.

on the model Hamiltonian and cannot lead to any reconstructions. In reality, the possible reconstruction scenarios are more likely for high concentration of Pd, high concentration vacancies or when Pd atoms are highly concentrated in a specific region of space. In this study, the goal was to distribute them randomly, with enough distance to avoid reconstructions. Therefore, the results might be less reliable if a region of the surface has overwhelmingly high Pd concentration than the rest. Also, one should be cautions when comparing the the results for higher Pd concentrations (more than 2%) with experimental studies, given that experimentally, the Pd concentration is mostly less than 1% .

Another important factor in interpreting the results are parameters in the model Hamiltonian. To understand the sensitivity of the final results with respect to their values, we varied the parameters randomly by 10% of their magnitude, for 10 different simulations. The results are plotted in Fig. 7.8, where the results with the same colors are performed with the same parameters. It is evident that the overall trend of the plot remains unchanged in the entire range of the chemical potential. The major differences are at the transitions, -1 eV, -1.15 eV, and at -1.30 eV, where there is shift in the vacancy concentration. In the rest of the regions, the difference between vacancy concentrations is negligible. Therefore, uncertainties in

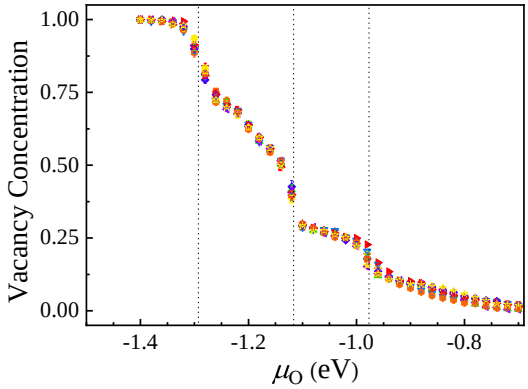

Figure 7.8: Oxygen vacancy concentrations vs. chemical potential at a fixed Pd concentration of 1.5% with variations in the parameters of the model Hamiltonian by 10% of the calculated magnitude. There are in total 15 different sets of parameters shown with different colors, with heavy overlapping make it harder to distinguish each set, especially away from the transition dotted lines.

the parameters, which can arise from the limited set of DFT calculations used to fit them or from ignoring higher order interactions, do not influence the trends for vacancy formation.

Chapter 8

Advantages and Disadvantages

The main focus of this chapter would be on the reliability of the model Hamiltonian approach, according to the results that were discussed in previous chapters, how to apply it to other systems. First, I present a fair comparison between the model Hamiltonian and the *Ab-initio* Thermodynamics methods, with some brief reminders on how they work, then they are compared against each other and eventually, there would discussion on the reasons why the model Hamiltonian method is generally preferred. In the last part, I discuss the possible difficulties and challenges when applying the model Hamiltonian approach. Based on the experiences gathered during my PhD studies, some solutions to common problems are provided.

8.1 The challenges in *Ab-initio* Thermodynamics

The main focus of this study was *not* on showing that the *Ab-initio* Thermodynamics is incorrect in predicting the thermodynamic properties of oxygen vacancies. It was about showing how the model Hamiltonian method can complete the picture *Ab-initio* Thermodynamics is used to provide and widen the horizon of questions we can answer.

Given a set of different configurations of oxygen vacancies, *Ab-initio* Thermodynamics can accurately determine which one would be the most stable configuration. However, one can see that it can only judge among the configurations that are selected beforehand. In other words, the mechanism behind

selecting the possible configurations is done independently. The problem with such a situation is that the study would be always biased toward the selected configurations. If the mechanism behind selecting those configurations is not well thought out, there is a high probability that some stable configurations were not included. If one reviews the previous studies that utilize *Ab-initio* Thermodynamics, most of them never explain how they choose some possible configurations. They are either based on some physical intuition— such as the assumption that bridging vacancies are the first to form on SnO_2 (110) surface—, or on some random configurations that looks interesting, for example a periodic diagonal pattern. The lack of general recipe in choosing the most stable structures is a severe limitation in understanding the most stable surface structure.

Another noticeable limitation is the surface cell size. Most studies have used the smallest possible surface unit-cell or at most up to 4 times of the smallest unit-cell, due to high computational cost of DFT calculations. This will seriously limit the number of distinct configurations one can consider and make some scenarios impossible to study. For example, as I showed in the results for the doped-Pd system, the vacancies tend to form as clusters surrounding the Pd atoms. It is close to impossible to do a DFT calculations for a surface with random clusters of vacancies scattered in the system. Similarly, for the case of the (110) surface, the combinations of patterns have low periodicity and cannot be modeled with small surface cells that are feasible at the DFT level. Even with the recent great advances in nano-electronics, the computational cost of DFT calculations, especially for large surfaces with low symmetries, remains high.

Aside from the limitation mentioned, *Ab-initio* Thermodynamics has been powerful in prediction of properties that agree with experimental studies. If one has a good understanding of the atomic elements involved in the system, with a wise choice of configurations based on earlier studies and physical properties of the system (for example oxidization number of atoms) and the complexity of the problem, it should provide an accurate estimation of the most stable surface configuration.

8.2 The advantages of model Hamiltonian approach

The first step in the model Hamiltonian approach is performing the DFT calculations on a set of distinct configurations. This is similar to *Ab-initio* Thermodynamics, with a difference that one can consider any possible configurations. For the case of vacancies on SnO_2 surfaces, all possible patterns that vacancies can form needs to be considered. As mentioned earlier, the number of configurations are still dependent on the surface-cell size at the DFT level. However, these configurations would not be compared with each other, but rather used in constructing a generalized model that can predict the energy of any vacancy pattern.

Once the model Hamiltonian is constructed from the DFT set of configurations, one can then proceeds to perform MC simulations to find the most stable surface configurations. This is the major difference between the model Hamiltonian approach and *Ab-initio* Thermodynamics. In the former case, the MC simulations start from a random state of the system— for the case of oxygen vacancies, a random number of vacancies distributed randomly all over the surface. In the latter, a direct comparison between DFT calculations determines which one of them is the most stable configuration. When both approaches are done carefully, then the MC simulations will provide finer resolution information than *Ab-initio* Thermodynamics. This was evident for the case of (101) surface, where I found the possible morphologies at the transition from the the oxidized surface to the reduced surface. Instead of a sudden transition predicted in *Ab-initio* Thermodynamics, one can see the intermediate step between the two phases. It should be mentioned that if one had been able to perform DFT for gigantic surface cell size ($e.g 40 \times 30$) then both methods should have given the same results, with *Ab-initio* Thermodynamics being the exact correct answer. Obviously, this is not the case now or in the near future, and the difference becomes more evident for the (110) surface. Creation of isolated clusters of bridging and in-plane vacancies is the first surprising result that could not be predicted at the DFT level. Even if one had a magically mysterious computer capable of doing DFT calculations for gigantic cell sizes, it is near impossible to imagine that a researcher coming up with such a configuration. In another words, due to the complexity of the

surface because of bridging and in-plane vacancies, it is very unlikely for even an expert in the field to guess such an input configuration for *Ab-initio* Thermodynamics. The other major outcome from the (110) surface calculations was the occurrence of grain boundaries. The surface under study was large enough to accommodate two different patterns, such that when they reach each other, new patters emerge. Even in the case of the clusters of vacancies for the Pd-doped system, the model Hamiltonian approach can tell us when and under what circumstances the clusters will overlap. These examples all show the near limitless power of Monte Carlo simulations that can answer questions that are impossible at the DFT level alone.

8.3 Challenges in the model Hamiltonian approach

8.3.1 Reconstructions

One major difficulty for the model Hamiltonian approach is the presence of reconstructions for some specific configurations. Any major relaxations that distort the structure noticeably are considered as reconstructions and should be avoided. It can be argued that reconstructions are due to surface-cell size at the DFT level. For example, when having more than 60 % of vacancies on SnO_2 (110), the vacancies have interaction that goes beyond their neighbor cells and extend far greater. Therefore, as shown in the appendices, most of scenarios that I considered for model Hamiltonian construction had vacancy concentration $\leq 50\%$. Even at lower concentration of vacancies, some specific arrangement of the vacancies are so unstable that either DFT calculations do not converge or a bridging vacancy turns into an in-plane vacancy. To deal with these scenarios, one usually increases the size of the surface cell to further isolate the vacancy patterns. Eventually, the model should be based on DFT calculations that have a finite range and magnitude of interactions. Adding more parameters in the model Hamiltonian may improve predictions for some reconstructions. However, this is typically not advisable, as reconstructions are mostly artifacts of the small surface unit-cell at the DFT level. For example, very high concentrations of vacancies on (110) are only stable at extreme temperatures ($> 1200K$). Therefore, even including such reconstructions does

not provide any meaningful results, due to the fact that DFT is a zero-temperature approximation and neglects any other entropic effects (diffusion of atoms, Sn interstitial etc.).

8.3.2 Number of parameters

Once a good number of different configurations are available, then one needs to find the most important interaction terms. The first important interaction that is easy to understand is the on-site (or one-body) interaction. For the case of oxygen vacancies, this corresponds to having isolated vacancies in a surface unit-cell. To check whether a single vacancy is sufficiently isolated or not, different cell sizes are compared (e.g. 2×2, 3×3, 4×2) and if one notices no significant changes when going to larger cell sizes, then it can be considered as an isolated vacancy. For a homogeneous surface, including pure (101) or (110) surfaces, all isolated vacancies are identical (or degenerate). However, in case of anisotropy in the system, as in the case of Pd-doped system, isolated vacancies need to be treated differently.

The next most important type of interactions are the pairwise, or two-body, interactions which are also heavily system dependent. The more symmetries a surface has, the fewer distinct two-body or higher order interactions present. One can generally start from the simplest nearest neighbor possibilities of the two-body interactions and then go toward more distant pairs. It is important to understand the limitation imposed by the size of the surface under study. In particular, if a two-body interaction is between two sites that are more than half of the distance of the cell away, then due to the periodicity of the system, their distance is closer in the opposite direction. Therefore, if one does not consider larger cell sizes, these is no way to distinguish these two types of interactions. Similarly, one cannot consider a two-body interaction between an element from one unit-cell with an element in any neighboring cell without having considered a larger cell size. One possible trick to check whether any of such redundant scenarios are not occurring is to compare the number of interactions for all the configurations. If one of the interactions is an integer multiple of another interaction, then they are redundant. For example, if the number of nearest neighbor two-body vacancy interactions are twice the number of third nearest neighbors for all the configurations,

then they are linearly dependent. An exact similar scenarios can also occur for three-body, four-body or any higher order interactions.

8.3.3 Over-fitting and under-fitting

There is always this question that one needs to answer: How many parameters are enough? Obviously, the answer to that question is completely system dependent and depends not only on the symmetry of the system, but also on the electronic properties. For the case of simple metal, a surface can be modeled with as few as 3 parameters to high accuracy. In this study, going from the (101) surface to the (110) surface, I had to add 8 more interaction terms to achieve the same level of accuracy. Starting with a single oxygen vacancy, when increasing the size of the system does not change the formation energy of the vacancy, it automatically corresponds to the upper limit of two-body interactions. Then one can start from nearest neighbor interactions and go up to the limit of an isolated vacancy. This procedure cannot be duplicated for higher order interactions, as they are more localized.

The general recipe for the prediction of the interaction parameters is as follows: Start with the fewest possible terms that provides a decent approximation (within 10%) with respect to the DFT calculations. If any configuration has energy estimation that is largely different from the DFT calculations, there are two possible scenarios: (1) Reconstructions at the DFT level cannot be predicted by the model Hamiltonian. If that is the case, then this configuration should be removed from the fitting set. (2) In absence of reconstructions at the DFT level, there must be missing termms in the model Hamiltonian. This can be either be two-body, three-body or even higher order term. It is better to start with the lower order types and then try higher order ones. If the model Hamiltonian becomes acceptable after adding any other parameters, then one faces a more generalized question. How many parameters is good enough? By adding more parameters, your estimation of the DFT set improves, however that comes at a cost of losing predictive power of the model Hamiltonian. Thus, there should be a balance between the accuracy with respect to the DFT results and statistical precision of the parameters in the model.

Another useful hint in constructing the model Hamiltonian is to define interaction terms that are more common in the configuration sets. If an L-shape three-body interaction occurs in several configurations, there would be a more precise estimate of that interaction compared to some unusual four-body interaction that can only be seen in a single configuration. Another possible way to evaluate the model Hamiltonian is to use it in predicting surface energies of a test set of configurations, not included in the fitting set. If there is a noticeable deviation between the predicti while such deviation was smaller for the fitting set (set of configuration that were used in the constructing of the model Hamiltonian) then we are over-fitting the model Hamiltonian. In this scenario, we need to reduce the types of interaction to those that are the most important ones.

8.3.4 Equilibrium in MC

With an accurate model Hamiltonian, one still cannot determine the most stable configuration. For a given surface, there are numerous possibilities of the vacancy patterns that can exist, and randomly looking at different states is both computationally expensive and highly unlikely to yield us the most stable state. The beauty of importance sampling, and in this study Metropolis sampling, is that the system systematically goes toward the most stable state, and the majority of phase space based on the Boltzmann distribution. With all the benefits that MC simulations have in predicting thermal properties, the results would only have physical meaning if the simulations are done carefully.

The main important check in MC simulations is whether the system is in equilibrium or not. One needs to test the convergence of the MC simulations with different types of MC moves in order to see whether the system reaches the same equilibrium state or not. If the simulations are long enough and if the basic necessary moves that enable the system to reach all possible states are defined, then the system will reach the equilibrium. The most basic moves are the swapping of the elements with their nearest neighbors. In the case of this study, an oxygen vacancy can swap with a nearest neighbor oxygen atom. Needless to say, the swapping between two identical vacancies (for example bridging vacancies) would not change any properties of the system and therefore are avoided. If a system is in a thermodynamic

equilibrium with a reservoir, then vacancies can be added or removed from the surface. So, without defining at least one type of move where vacancies can be created or annihilated, the concentration of vacancies would always remains the same, and only their distribution would change. In general, the total number of moves and simulation time to reach equilibrium depends heavily on the complexity of the system and needs to be checked independently for different systems. One can start with a few MC moves, run the simulation for a specific length (say 1000 MCS). Then increase the number of MCS to see if there is any change in the final properties of the system. Then add new moves and perform the simulation for enough MCS until system reaches equilibrium. If adding new moves does not yield any differences in the final results, then all the simulations are safe to be done with the previous number of MC moves.

Note that MC simulations are stochastic, and without having a set of uncorrelated data, the value of physical parameters cannot be trusted. This means, if one is interested in average energy, there are two ways to estimate the average energy: (1) Run a single simulation long enough to reach equilibrium, then calculated the average energy every S step such that each average energy value is not correlated to the other ones. S is a parameter that needs to be determined carefully and should be long enough to make two different states independent. (2) Perform several independent MC simulations and find the average energy when each of them reaches equilibrium. Then average over those energy values. In theory, both approaches should yield the same value given that each sample of energy is independent of the others. In this study, I only used the second approach where 20 different MC simulations were performed at the same time, with different initial distributions of vacancies.

It should be mentioned that doing accurate MC simulations does not guarantee a correct results. Every output of the MC simulations heavily depends on the input parameters determined by the model Hamiltonian and accuracy of the DFT calculations. Therefore, the patterns observed from the MC simulations should be justified by the parameters of the model Hamiltonian. This phenomenon is sometimes referred to as "garbage in, garbage out". A perfect MC simulation can provide the correct results with respect to the model Hamiltonian that is provided. If there are some missing parameters in the model Hamiltonian, MC simulations can result in completely different results and physical interpretations. Therefore, it is

always advised to check the sensitivity of the results with respect to the model Hamiltonian. Such an analysis was done for the Pd-doped surface, where I randomly varied the magnitude of the parameters by 10% of their magnitude. The mostly negligible changes that were observed indicates that one does not need necessarily a perfect model Hamiltonian that matches DFT energy estimations. Thus, rather than spending more time on improving the accuracy with respect to DFT calculations, one can first get a decent approximation for the model Hamiltonian, test the sensitivity of the model Hamiltonian and only then focuses on improving the model Hamiltonian if necessary.

Chapter 9

Conclusion

Understanding how oxygen vacancies are formed on SnO_2, their morphologies under different thermodynamic conditions and how transition metals like Pd can facilitate the formation of them were the main subjects of this dissertation. I believe that the results found in this dissertation can provide an improve picture of the role of oxygen vacancies in gas sensing. Moreover, the model Hamiltonian approach, which has been used before in tackling other types of problems, is shown to be a robust approach when dealing with oxygen vacancies. In this chapter, I briefly mention some highlights of the dissertation in the order of the chapters.

The importance of SnO_2 cannot be overstated as it has been widely used as a resistive-type gas sensors for the past few decades. With hundreds of papers already published about this material, it is still interesting to see how fundamental properties of SnO_2 can hardly be explained at the atomic level. Most notably, the dissociation of oxygen molecules on the surfaces of SnO_2 draws attention, as the exact morphology of the surfaces and energetics of adsorption and dissociation were not well understood. Experimental studies that tried to get an accurate estimation of the surface morphologies often have low resolution at the working condition of sensors: room pressure and $400 - 600$ K of temperature. For the case of the (110) surface, even available pictures of the surface at reducing conditions lack atomistic resolution at the mentioned temperatures. A clear over-layer was only visible at high temperatures (> 900 K). On the other hand, theoretical studies used the *Ab-initio* Thermodynamics approach to find the most stable surface

morphology. One difficulty in using that method, as mentioned in chapter 8 is to find the correct set of configurations that include the most stable configuration.

To improve the prediction of *Ab-initio* Thermodynamics and provide a more detailed picture of the surfaces, I used the model Hamiltonian method, combining two different methodologies: DFT calculations and MC simulations. This method has been used in other contexts but has never been applied in studying oxygen vacancies. In this method, a model Hamiltonian is fitted to a set of surface energies for different configurations done at DFT level. After several testings that yield good accuracy and robustness of the model Hamiltonian, it is then used in a classical MC simulations based on Metropolis importance sampling. I refer the reader to chapter 8 on how to use the methodology in applying to different problems.

The results are provided in three different chapters. Chapter 5 deals with the problem of oxygen vacancies on the (101) surface of SnO_2. This surface is simple to study due to having only bridging sites at the surface. Our analysis showed that the vacancies can be formed as rows of vacancies along the [010] direction due to the clear attractive interaction between the vacancies in that direction. At the same time, the repulsion between the vacancies of adjacent rows prevents them from fully covering the surface. Therefore, in a range of chemical potential -1.15 eV to -1.30 eV there is mostly a 2×1 patterns with alternating rows of vacancies. These results were compared with *Ab-initio* Thermodynamics, and great agreement was found for chemical potentials of the transitions to the reduced surfaces. Moreover, it could be seen that rows of vacancies are first isolated, before creating the 2×1 pattern. Eventually, the surface reach the fully reduced 1×1 surface. In the absence of MC simulations, such detailed pictures would require an unrealistically large surface cell of 40×1 for DFT calculations.

Similarly, analysis of the (110) surface reveals interesting morphologies when vacancies form. The surface was more complex due to the presence of two types of oxygen vacancies, bridging and in-plane. My tests on the model Hamiltonian reveal that in-plane vacancies tend to have stronger interactions than the bridging vacancies and have a higher range of two-body interactions. Also, the three-body interaction plays a significantly important role such than without them, it would have been impossible to have an acceptable approximation for the surface energy. However, the main challenging part was the fact that an

additional fictitious four-body interaction was necessary to be included in the model Hamiltonian. This was found after MC simulations resulted in a reduced surface with no oxygen atoms at the surface. Such a scenario corresponds to a metallic tin surface, which can only be stable under exceptionally reduced conditions, far from the working sensor conditions. The fictitious four-body interaction guaranteed that the surface will not reduce to such extreme scenarios in the MC simulations. With an accurate estimation of the model Hamiltonian, the MC simulations then resulted in morphologies that had similar patterns to those of the *Ab-initio* Thermodynamics. Specifically, rows of bridging and in-plane vacancies are formed along the [001] direction, with the same structure as the previously reported 1×1 pattern. However, they are formed as clusters scattered randomly on the surface. It is only after going toward a more oxygen deficient environment that they become elongated and cover the entire surface. Also, my research reveals two new patterns that arise from the grain boundaries between the two different patterns of the surface. The 1×1 pattern with its mirror symmetry meet at certain region of the surface, resulting in either a no in-plane vacancy region or the zipper pattern (discussed in chapter 6).

The last part of the results was meant to show another example of using the model Hamiltonian, that is both relevant to the applications of the SnO_2 gas sensors and also can be applied to a wide range other problems. Namely, the presence of a Pd dopant in the form of substitution with Sn atoms was studied using the model Hamiltonian method. In agreement with experimental studies, within a certain region of Pd atoms, the surface morphology is heavily influenced by the Pd atoms. Vacancies, present as clusters surrounding the Pd atoms, are stable at conditions close to room pressure and can now be regarded as active sites for sensing different gas species. The results of this chapter provide a deeper understanding on one of the main reasons that the transition metals play a vital role in improving the gas sensing capabilities of SnO_2. On pure surfaces, oxygen vacancies were only stable under extreme reducing conditions, especially for the (110) surface. However, even a percent of Pd atoms at the surface can significantly lower the energy cost of having oxygen vacancies.

The research discussed in this dissertation provided a new approach to a relatively old problem of oxygen vacancies on SnO_2 surfaces. Many of the patterns observed were partially achieved in *Ab-initio*

Thermodynamics, but lacked the detailed picture that could only be found using MC simulations. This method can be applied when studying different types of dopants in the system, and the output of the reduced surface Pd-doped (101) surface can be used for further investigation on molecular adsorption and dissociation. In addition, the model Hamiltonian approach has become more popular in recent years and is being used in other context, from studying the adsorption of molecules, to the stability of different transition metals in disordered rock salt (DRX) materials and Kinetic Monte Carlo simulations. This study was a successful attempt to show how a simple model can capture properties that look unfeasible and unrealistic to study in theory.

Bibliography

[1] C. Wang, L. Yin, L. Zhang, D. Xiang, and R. Gao, "Metal oxide gas sensors: Sensitivity and influencing factors", vol. 10, no. 3, pp. 2088–2106, Mar. 2010. DOI: 10.3390/s100302088. [Online]. Available: https://doi.org/10.33902Fs100302088.

[2] A. Dey, "Semiconductor metal oxide gas sensors: A review", *Materials Science and Engineering: B*, vol. 229, pp. 206–217, 2018, ISSN: 0921-5107. DOI: https://doi.org/10.1016/j.mseb.2017.12.036. [Online]. Available: https://www.sciencedirect.com/science/article/pii/S0921510717303574.

[3] T. Miller, S. Bakrania, C. Perez, and M. S. Wooldridge, "Nanostructured tin dioxide materials for gas sensor applications", 2006.

[4] A. Gurlo, "Interplay between O2 and SnO2: Oxygen ionosorption and spectroscopic evidence for adsorbed oxygen", *ChemPhysChem*, vol. 7, no. 10, pp. 2041–2052, 2006. DOI: https://doi.org/10.1002/cphc.200600292. eprint: https://chemistry-europe.onlinelibrary.wiley.com/doi/pdf/10.1002/cphc.200600292. [Online]. Available: https://chemistry-europe.onlinelibrary.wiley.com/doi/abs/10.1002/cphc.200600292.

[5] J. F. Wager, "Transparent electronics", *Science*, vol. 300, no. 5623, pp. 1245–1246, 2003. DOI: 10.1126/science.1085276. eprint: https://www.science.org/doi/pdf/10.1126/science.1085276. [Online]. Available: https://www.science.org/doi/abs/10.1126/science.1085276.

[6] R. L. Hoffman, B. J. Norris, and J. F. Wager, "Zno-based transparent thin-film transistors", *Applied Physics Letters*, vol. 82, no. 5, pp. 733–735, 2003. DOI: 10.1063/1.1542677. eprint: https://doi.org/10.1063/1.1542677. [Online]. Available: https://doi.org/10.1063/1.1542677.

[7] S. Masuda, K. Kitamura, Y. Okumura, S. Miyatake, H. Tabata, and T. Kawai, "Transparent thin film transistors using ZnO as an active channel layer and their electrical properties", *Journal of Applied Physics*, vol. 93, no. 3, pp. 1624–1630, 2003. DOI: 10.1063/1.1534627. eprint: https://doi.org/10.1063/1.1534627. [Online]. Available: https://doi.org/10.1063/1.1534627.

[8] R. E. Presley, C. L. Munsee, C.-H. Park, D. Hong, J. F. Wager, and D. A. Keszler, "Tin oxide transparent thin-film transistors", *Journal of Physics D: Applied Physics*, vol. 37, no. 20, pp. 2810–2813, Sep. 2004. DOI: 10.1088/0022-3727/37/20/006. [Online]. Available: https://doi.org/10.1088/0022-3727/37/20/006.

[9] M. Fuller and M. Warwick, "The catalytic oxidation of carbon monoxide on tin(iv) oxide", *Journal of Catalysis*, vol. 29, no. 3, pp. 441–450, 1973, ISSN: 0021-9517. DOI: https://doi.org/10.1016/0021-9517(73)90251-0. [Online]. Available: https://www.sciencedirect.com/science/article/pii/0021951773902510.

[10] ——, "The catalytic oxidation of carbon monoxide on SnO2-CuO gels", *Journal of Catalysis*, vol. 34, no. 3, pp. 445–453, 1974, ISSN: 0021-9517. DOI: https://doi.org/10.1016/0021-9517(74)90058-X. [Online]. Available: https://www.sciencedirect.com/science/article/pii/002195177490058X.

[11] F. Solymosi and J. Kiss, "Adsorption and reduction of no on tin(iv) oxide doped with chromium(iii) oxide", *Journal of Catalysis*, vol. 54, no. 1, pp. 42–51, 1978, ISSN: 0021-9517. DOI: https://doi.org/10.1016/0021-9517(78)90025-8. [Online]. Available: https://www.sciencedirect.com/science/article/pii/0021951778900258.

[12] P. G. Harrison, C. Bailey, and W. Azelee, "Modified tin(iv) oxide (m/sno2m=cr, la, pr, nd, sm, gd) catalysts for the oxidation of carbon monoxide and propane", *Journal of Catalysis*, vol. 186, no. 1, pp. 147–159, 1999, ISSN: 0021-9517. DOI: https://doi.org/10.1006/jcat.1999.2528. [Online]. Available: https://www.sciencedirect.com/science/article/pii/S0021951799925289.

[13] P. Park, H. Kung, D.-W. Kim, and M. Kung, "Characterization of SnO_2/Al_2O_3 lean nox catalysts", *Journal of Catalysis*, vol. 184, no. 2, pp. 440–454, 1999, ISSN: 0021-9517. DOI: https://doi.org/10.1006/jcat.1999.2459. [Online]. Available: https://www.sciencedirect.com/science/article/pii/S0021951799924594.

[14] G. C. Bond, L. R. Molloy, and M. J. Fuller, "Oxidation of carbon monoxide over palladium–tin(iv) oxide catalysts: An example of spillover catalysis", *J. Chem. Soc., Chem. Commun.*, pp. 796–797, 19 1975. DOI: 10.1039/C39750000796. [Online]. Available: http://dx.doi.org/10.1039/C39750000796.

[15] M. E. Franke, T. J. Koplin, and U. Simon, "Metal and metal oxide nanoparticles in chemiresistors: Does the nanoscale matter?", *Small*, vol. 2, no. 1, pp. 36–50, 2006. DOI: https://doi.org/10.1002/smll.200500261. eprint: https://onlinelibrary.wiley.com/doi/pdf/10.1002/smll.200500261. [Online]. Available: https://onlinelibrary.wiley.com/doi/abs/10.1002/smll.200500261.

[16] M. Chiesa, M. C. Paganini, E. Giamello, and D. M. Murphy, "O- radical ions on mgo: A tool for a structural description of the surface", *Research on Chemical Intermediates*, vol. 28, no. 2, pp. 205–214, 2002. DOI: 10.1163/156856702320267118. [Online]. Available: https://doi.org/10.1163/156856702320267118.

[17] M. Iwamoto, Y. Yoda, N. Yamazoe, and T. Seiyama, "Study of metal oxide catalysts by temperature programmed desorption. 4. oxygen adsorption on various metal oxides", *The Journal of Physical Chemistry*, vol. 82, no. 24, pp. 2564–2570, 1978. DOI: 10.1021/j100513a006. eprint: https:

//doi.org/10.1021/j100513a006. [Online]. Available: https://doi.org/10.1021/j100513a006.

[18] M. Che and A. Tench, "Characterization and reactivity of mononuclear oxygen species on oxide surfaces", in ser. Advances in Catalysis, D. Eley, H. Pines, and P. B. Weisz, Eds., vol. 31, Academic Press, 1982, pp. 77–133. DOI: https://doi.org/10.1016/S0360-0564(08)60453-8. [Online]. Available: https://www.sciencedirect.com/science/article/pii/S0360056408604538.

[19] I. Kocemba and J. M. Rynkowski, "The effect of oxygen adsorption on catalytic activity of SnO2 in co oxidation", *Catalysis Today*, vol. 169, no. 1, pp. 192–199, 2011, Jerzy Haber - a man who wanted to know and to understand. Sixty years of activity in the field of chemistry and catalysis, ISSN: 0920-5861. DOI: https://doi.org/10.1016/j.cattod.2010.09.015. [Online]. Available: https://www.sciencedirect.com/science/article/pii/S092058611000564X.

[20] W. Wei, Y. Dai, and B. Huang, "Role of cu doping in sno2 sensing properties toward h2s", *The Journal of Physical Chemistry C*, vol. 115, no. 38, pp. 18 597–18 602, 2011. DOI: 10.1021/jp204170j. eprint: https://doi.org/10.1021/jp204170j. [Online]. Available: https://doi.org/10.1021/jp204170j.

[21] S.-N. Hong, Y.-H. Kye, C.-J. Yu, *et al.*, "Ab initio thermodynamic study of the SnO2(110) surface in an O2 and no environment: A fundamental understanding of the gas sensing mechanism for no and NO2", *Phys. Chem. Chem. Phys.*, vol. 18, pp. 31 566–31 578, 46 2016. DOI: 10.1039/C6CP05433A. [Online]. Available: http://dx.doi.org/10.1039/C6CP05433A.

[22] M. Epifani, J. D. Prades, E. Comini, *et al.*, "The role of surface oxygen vacancies in the NO2 sensing properties of SnO2 nanocrystals", *The Journal of Physical Chemistry C*, vol. 112, no. 49, pp. 19 540–19 546, 2008. DOI: 10.1021/jp804916g. eprint: https://doi.org/10.1021/jp804916g. [Online]. Available: https://doi.org/10.1021/jp804916g.

[23] J. D. Prades, A. Cirera, and J. R. Morante, "First-principles study of NO[sub x] and SO[sub 2] adsorption onto SnO[sub 2](110)", vol. 154, no. 8, H675, 2007. DOI: 10.1149/1.2742295. [Online]. Available: https://doi.org/10.1149/1.2742295.

[24] A. K. Singh, A. Janotti, M. Scheffler, and C. G. Van de Walle, "Sources of electrical conductivity in SnO_2", *Phys. Rev. Lett.*, vol. 101, p. 055 502, 5 Jul. 2008. DOI: 10.1103/PhysRevLett.101.055502. [Online]. Available: https://link.aps.org/doi/10.1103/PhysRevLett.101.055502.

[25] S. Lany and A. Zunger, "Assessment of correction methods for the band-gap problem and for finite-size effects in supercell defect calculations: Case studies for ZnO and GaAs", *Phys. Rev. B*, vol. 78, p. 235 104, 23 Dec. 2008. DOI: 10.1103/PhysRevB.78.235104. [Online]. Available: https://link.aps.org/doi/10.1103/PhysRevB.78.235104.

[26] P. Ágoston, K. Albe, R. M. Nieminen, and M. J. Puska, "Intrinsic *n*-type behavior in transparent conducting oxides: A comparative hybrid-functional study of In_2O_3, SnO_2, and ZnO", *Phys. Rev. Lett.*, vol. 103, p. 245 501, 24 Dec. 2009. DOI: 10.1103/PhysRevLett.103.245501. [Online]. Available: https://link.aps.org/doi/10.1103/PhysRevLett.103.245501.

[27] P. D. C. King and T. D. Veal, "Conductivity in transparent oxide semiconductors", *Journal of Physics: Condensed Matter*, vol. 23, no. 33, p. 334 214, Aug. 2011. DOI: 10.1088/0953-8984/23/33/334214. [Online]. Available: https://doi.org/10.1088/0953-8984/23/33/334214.

[28] J. Oviedo and M. Gillan, "First-principles study of the interaction of oxygen with the sno2(110) surface", *Surface Science*, vol. 490, no. 3, pp. 221–236, 2001, ISSN: 0039-6028. DOI: https://doi.org/10.1016/S0039-6028(01)01372-3. [Online]. Available: https://www.sciencedirect.com/science/article/pii/S0039602801013723.

[29] M. Habgood and N. Harrison, "An ab initio study of oxygen adsorption on tin dioxide", *Surface Science*, vol. 602, no. 5, pp. 1072–1079, 2008, ISSN: 0039-6028. DOI: https://doi.org/10.

1016/j.susc.2008.01.017. [Online]. Available: https://www.sciencedirect.com/science/article/pii/S0039602808000095.

[30] V. Golovanov, V. Golovanova, and T. T. Rantala, "Thermal desorption of molecular oxygen from SnO2 (110) surface: Insights from first-principles calculations", *Journal of Physics and Chemistry of Solids*, vol. 89, pp. 15–22, 2016, ISSN: 0022-3697. DOI: https://doi.org/10.1016/j.jpcs.2015.10.010. [Online]. Available: https://www.sciencedirect.com/science/article/pii/S0022369715300780.

[31] M. Batzill, K. Katsiev, J. M. Burst, U. Diebold, A. M. Chaka, and B. Delley, "Gas-phase-dependent properties of SnO_2 (110), (100), and (101) single-crystal surfaces: Structure, composition, and electronic properties", *Phys. Rev. B*, vol. 72, p. 165 414, 16 Oct. 2005. DOI: 10.1103/PhysRevB.72.165414. [Online]. Available: https://link.aps.org/doi/10.1103/PhysRevB.72.165414.

[32] D. F. Cox, T. B. Fryberger, and S. Semancik, "Oxygen vacancies and defect electronic states on the SnO_2(110)-1×1 surface", *Phys. Rev. B*, vol. 38, pp. 2072–2083, 3 Jul. 1988. DOI: 10.1103/PhysRevB.38.2072. [Online]. Available: https://link.aps.org/doi/10.1103/PhysRevB.38.2072.

[33] M. Batzill and U. Diebold, "The surface and materials science of tin oxide", *Progress in Surface Science*, vol. 79, no. 2, pp. 47–154, 2005, ISSN: 0079-6816. DOI: https://doi.org/10.1016/j.progsurf.2005.09.002. [Online]. Available: https://www.sciencedirect.com/science/article/pii/S007968160500050X.

[34] L. R. Merte, M. S. Jørgensen, K. Pussi, *et al.*, "Structure of the $SnO_2(110)-(4\times1)$ surface", *Phys. Rev. Lett.*, vol. 119, p. 096 102, 9 Aug. 2017. DOI: 10.1103/PhysRevLett.119.096102. [Online]. Available: https://link.aps.org/doi/10.1103/PhysRevLett.119.096102.

[35] J. Oviedo and M. Gillan, "The energetics and structure of oxygen vacancies on the sno2(110) surface", *Surface Science*, vol. 467, no. 1, pp. 35–48, 2000, ISSN: 0039-6028. DOI: https://

doi.org/10.1016/S0039-6028(00)00776-7. [Online]. Available: https://www.sciencedirect.com/science/article/pii/S0039602800007767.

[36] K. Reuter and M. Scheffler, "Composition, structure, and stability of $RuO_2(110)$ as a function of oxygen pressure", *Phys. Rev. B*, vol. 65, p. 035 406, 3 Dec. 2001. DOI: 10.1103/PhysRevB.65.035406. [Online]. Available: https://link.aps.org/doi/10.1103/PhysRevB.65.035406.

[37] W. Bergermayer and I. Tanaka, "Reduced sno2 surfaces by first-principles calculations", *Applied Physics Letters*, vol. 84, no. 6, pp. 909–911, 2004. DOI: 10.1063/1.1646460. eprint: https://doi.org/10.1063/1.1646460. [Online]. Available: https://doi.org/10.1063/1.1646460.

[38] M. A. Mäki-Jaskari and T. T. Rantala, "Band structure and optical parameters of the $SnO_2(110)$ surface", *Phys. Rev. B*, vol. 64, p. 075 407, 7 Jul. 2001. DOI: 10.1103/PhysRevB.64.075407. [Online]. Available: https://link.aps.org/doi/10.1103/PhysRevB.64.075407.

[39] T. J. Godin and J. P. LaFemina, "Surface atomic and electronic structure of cassiterite SnO_2 (110)", *Phys. Rev. B*, vol. 47, pp. 6518–6523, 11 Mar. 1993. DOI: 10.1103/PhysRevB.47.6518. [Online]. Available: https://link.aps.org/doi/10.1103/PhysRevB.47.6518.

[40] I. Manassidis, J. Goniakowski, L. Kantorovich, and M. Gillan, "The structure of the stoichiometric and reduced SnO2(110) surface", *Surface Science*, vol. 339, no. 3, pp. 258–271, 1995, ISSN: 0039-6028. DOI: https://doi.org/10.1016/0039-6028(95)00677-X. [Online]. Available: https://www.sciencedirect.com/science/article/pii/003960289500677X.

[41] X. Xu, J. Sun, H. Zhang, *et al.*, "Effects of al doping on SnO2 nanofibers in hydrogen sensor", *Sensors and Actuators B: Chemical*, vol. 160, no. 1, pp. 858–863, 2011, ISSN: 0925-4005. DOI: https://doi.org/10.1016/j.snb.2011.08.072. [Online]. Available: https://www.sciencedirect.com/science/article/pii/S0925400511007957.

[42] P. Song, Q. Wang, and Z. Yang, "Preparation, characterization and acetone sensing properties of ce-doped sno2 hollow spheres", *Sensors and Actuators B: Chemical*, vol. 173, pp. 839–846, 2012, ISSN: 0925-4005. DOI: https://doi.org/10.1016/j.snb.2012.07.115. [Online]. Available: https://www.sciencedirect.com/science/article/pii/S092540051200809X.

[43] W. Wei, Y. Dai, and B. Huang, "Role of cu doping in SnO2 sensing properties toward h2s", *The Journal of Physical Chemistry C*, vol. 115, no. 38, pp. 18 597–18 602, 2011. DOI: 10.1021/jp204170j. eprint: https://doi.org/10.1021/jp204170j. [Online]. Available: https://doi.org/10.1021/jp204170j.

[44] W.-H. Yang, W.-C. Lu, X.-Y. Xue, and Q.-J. Zang, "A theoretical study on co sensing mechanism of in-doped sno2 (110) surface", *Computational and Theoretical Chemistry*, vol. 1069, pp. 119–124, 2015, ISSN: 2210-271X. DOI: https://doi.org/10.1016/j.comptc.2015.07.012. [Online]. Available: https://www.sciencedirect.com/science/article/pii/S2210271X15002923.

[45] K. Jain, R. Pant, and S. Lakshmikumar, "Effect of ni doping on thick film SnO2 gas sensor", *Sensors and Actuators B: Chemical*, vol. 113, no. 2, pp. 823–829, 2006, Special Issue - In honour of Professor Karl Cammann, ISSN: 0925-4005. DOI: https://doi.org/10.1016/j.snb.2005.03.104. [Online]. Available: https://www.sciencedirect.com/science/article/pii/S0925400505003527.

[46] Z. Zhu, R. C. Deka, A. Chutia, *et al.*, "Enhanced gas-sensing behaviour of ru-doped SnO2 surface: A periodic density functional approach", *Journal of Physics and Chemistry of Solids*, vol. 70, no. 9, pp. 1248–1255, 2009, ISSN: 0022-3697. DOI: https://doi.org/10.1016/j.jpcs.2009.07.012. [Online]. Available: https://www.sciencedirect.com/science/article/pii/S0022369709001693.

[47] J. H. Yu and G. M. Choi, "Selective co gas detection of CuO- and ZnO-doped SnO2 gas sensor", *Sensors and Actuators B: Chemical*, vol. 75, no. 1, pp. 56–61, 2001, ISSN: 0925-4005. DOI: https:

//doi.org/10.1016/S0925-4005(00)00742-5. [Online]. Available: https://www.sciencedirect.com/science/article/pii/S0925400500007425.

[48] A. Kolmakov, D. O. Klenov, Y. Lilach, S. Stemmer, and M. Moskovits, "Enhanced gas sensing by individual sno2 nanowires and nanobelts functionalized with pd catalyst particles", *Nano Letters*, vol. 5, no. 4, pp. 667–673, 2005, PMID: 15826106. DOI: 10.1021/nl050082v. eprint: https://doi.org/10.1021/nl050082v. [Online]. Available: https://doi.org/10.1021/nl050082v.

[49] C. Bittencourt, E. Llobet, P. Ivanov, *et al.*, "Influence of the doping method on the sensitivity of pt-doped screen-printed SnO2 sensors", *Sensors and Actuators B: Chemical*, vol. 97, no. 1, pp. 67–73, 2004, ISSN: 0925-4005. DOI: https://doi.org/10.1016/S0925-4005(03)00648-8. [Online]. Available: https://www.sciencedirect.com/science/article/pii/S0925400503006488.

[50] S. Hahn, N. Bârsan, U. Weimar, S. Ejakov, J. Visser, and R. Soltis, "Co sensing with SnO2 thick film sensors: Role of oxygen and water vapour", *Thin Solid Films*, vol. 436, no. 1, pp. 17–24, 2003, Papers from the 3rd International Seminar on Semiconductor Gas Sensors, ISSN: 0040-6090. DOI: https://doi.org/10.1016/S0040-6090(03)00520-0. [Online]. Available: https://www.sciencedirect.com/science/article/pii/S0040609003005200.

[51] S. Li, Z. Lu, Z. Yang, and X. Chu, "The sensing mechanism of pt-doped SnO2 surface toward co: A first-principle study", *Sensors and Actuators B: Chemical*, vol. 202, pp. 83–92, 2014, ISSN: 0925-4005. DOI: https://doi.org/10.1016/j.snb.2014.05.071. [Online]. Available: https://www.sciencedirect.com/science/article/pii/S0925400514006005.

[52] M. A. Mäki-Jaskari and T. T. Rantala, "Density functional study of pd adsorbates at SnO2(110) surfaces", *Surface Science*, vol. 537, no. 1, pp. 168–178, 2003, ISSN: 0039-6028. DOI: https://doi.org/10.1016/S0039-6028(03)00615-0. [Online]. Available: https://www.sciencedirect.com/science/article/pii/S0039602803006150.

[53] Y. Xue and Z. Tang, "Density functional study of the interaction of co with undoped and pd doped SnO2(110) surface", *Sensors and Actuators B: Chemical*, vol. 138, no. 1, pp. 108–112, 2009, ISSN: 0925-4005. DOI: https://doi.org/10.1016/j.snb.2009.02.030. [Online]. Available: https://www.sciencedirect.com/science/article/pii/S0925400509001506.

[54] P. Bechthold, M. E. Pronsato, and C. Pistonesi, "Dft study of co adsorption on pd-SnO2(110) surfaces", *Applied Surface Science*, vol. 347, pp. 291–298, 2015, ISSN: 0169-4332. DOI: https://doi.org/10.1016/j.apsusc.2015.03.149. [Online]. Available: https://www.sciencedirect.com/science/article/pii/S016943321500745X.

[55] J. Kohanoff, *Electronic Structure Calculations for Solids and Molecules: Theory and Computational Methods*. Cambridge University Press, 2006. DOI: 10.1017/CBO9780511755613.

[56] C. Kittel, *Introduction to Solid State Physics, 6th edition*. Wiley, New York, 1986.

[57] "The free fermi gas and single electron model", in *Condensed Matter Physics*. John Wiley Sons, Ltd, 2010, ch. 6, pp. 155–173, ISBN: 9780470949955. DOI: https://doi.org/10.1002/9780470949955.ch6. eprint: https://onlinelibrary.wiley.com/doi/pdf/10.1002/9780470949955.ch6. [Online]. Available: https://onlinelibrary.wiley.com/doi/abs/10.1002/9780470949955.ch6.

[58] P. Hohenberg and W. Kohn, "Inhomogeneous electron gas", *Phys. Rev.*, vol. 136, B864–B871, 3B Nov. 1964. DOI: 10.1103/PhysRev.136.B864. [Online]. Available: https://link.aps.org/doi/10.1103/PhysRev.136.B864.

[59] M. Levy, "Electron densities in search of hamiltonians", *Phys. Rev. A*, vol. 26, pp. 1200–1208, 3 Sep. 1982. DOI: 10.1103/PhysRevA.26.1200. [Online]. Available: https://link.aps.org/doi/10.1103/PhysRevA.26.1200.

[60] R. M. Martin, *Electronic Structure: Basic Theory and Practical Methods*. Cambridge University Press, 2004. DOI: 10.1017/CBO9780511805769.

[61] W. Kohn and L. J. Sham, "Self-consistent equations including exchange and correlation effects", *Phys. Rev.*, vol. 140, A1133–A1138, 4A Nov. 1965. DOI: 10.1103/PhysRev.140.A1133. [Online]. Available: https://link.aps.org/doi/10.1103/PhysRev.140.A1133.

[62] A. Görling, "Density-functional theory for excited states", *Phys. Rev. A*, vol. 54, pp. 3912–3915, 5 Nov. 1996. DOI: 10.1103/PhysRevA.54.3912. [Online]. Available: https://link.aps.org/doi/10.1103/PhysRevA.54.3912.

[63] P. Giannozzi, S. Baroni, N. Bonini, *et al.*, "QUANTUM ESPRESSO: A modular and open-source software project for quantum simulations of materials", *Journal of Physics: Condensed Matter*, vol. 21, no. 39, p. 395 502, Sep. 2009. DOI: 10.1088/0953-8984/21/39/395502.

[64] J. P. Perdew, K. Burke, and M. Ernzerhof, "Generalized gradient approximation made simple", *Phys. Rev. Lett.*, vol. 77, pp. 3865–3868, 18 Oct. 1996. DOI: 10.1103/PhysRevLett.77.3865. [Online]. Available: https://link.aps.org/doi/10.1103/PhysRevLett.77.3865.

[65] J. P. Perdew, A. Ruzsinszky, G. I. Csonka, *et al.*, "Restoring the density-gradient expansion for exchange in solids and surfaces", *Phys. Rev. Lett.*, vol. 100, p. 136 406, 13 Apr. 2008. DOI: 10.1103/PhysRevLett.100.136406. [Online]. Available: https://link.aps.org/doi/10.1103/PhysRevLett.100.136406.

[66] J. P. Perdew, K. Burke, and M. Ernzerhof, "Generalized gradient approximation made simple", *Phys. Rev. Lett.*, vol. 77, pp. 3865–3868, 18 Oct. 1996. DOI: 10.1103/PhysRevLett.77.3865. [Online]. Available: https://link.aps.org/doi/10.1103/PhysRevLett.77.3865.

[67] D. Vanderbilt, "Soft self-consistent pseudopotentials in a generalized eigenvalue formalism", *Phys. Rev. B*, vol. 41, pp. 7892–7895, 11 Apr. 1990. DOI: 10.1103/PhysRevB.41.7892. [Online]. Available: https://link.aps.org/doi/10.1103/PhysRevB.41.7892.

[68] H. J. Monkhorst and J. D. Pack, "Special points for brillouin-zone integrations", *Phys. Rev. B*, vol. 13, pp. 5188–5192, 12 Jun. 1976. DOI: 10.1103/PhysRevB.13.5188. [Online]. Available: https://link.aps.org/doi/10.1103/PhysRevB.13.5188.

[69] X.-G. Wang, A. Chaka, and M. Scheffler, "Effect of the environment on $\alpha - Al_2O_3$ (0001) surface structures", *Phys. Rev. Lett.*, vol. 84, pp. 3650–3653, 16 Apr. 2000. DOI: 10.1103/PhysRevLett.84.3650. [Online]. Available: https://link.aps.org/doi/10.1103/PhysRevLett.84.3650.

[70] Q. Sun, K. Reuter, and M. Scheffler, "Effect of a humid environment on the surface structure of $RuO_2(110)$", *Phys. Rev. B*, vol. 67, p. 205 424, 20 May 2003. DOI: 10.1103/PhysRevB.67.205424. [Online]. Available: https://link.aps.org/doi/10.1103/PhysRevB.67.205424.

[71] K. Reuter and M. Scheffler, "First-principles atomistic thermodynamics for oxidation catalysis: Surface phase diagrams and catalytically interesting regions", *Phys. Rev. Lett.*, vol. 90, p. 046 103, 4 Jan. 2003. DOI: 10.1103/PhysRevLett.90.046103. [Online]. Available: https://link.aps.org/doi/10.1103/PhysRevLett.90.046103.

[72] W.-X. Li, C. Stampfl, and M. Scheffler, "Insights into the function of silver as an oxidation catalyst by ab initio atomistic thermodynamics", *Phys. Rev. B*, vol. 68, p. 165 412, 16 Oct. 2003. DOI: 10.1103/PhysRevB.68.165412. [Online]. Available: https://link.aps.org/doi/10.1103/PhysRevB.68.165412.

[73] X.-G. Wang, W. Weiss, S. K. Shaikhutdinov, *et al.*, "The hematite (α- Fe_2O_3) (0001) surface: Evidence for domains of distinct chemistry", *Phys. Rev. Lett.*, vol. 81, pp. 1038–1041, 5 Aug. 1998. DOI: 10.1103/PhysRevLett.81.1038. [Online]. Available: https://link.aps.org/doi/10.1103/PhysRevLett.81.1038.

[74] J. Sanchez, F. Ducastelle, and D. Gratias, "Generalized cluster description of multicomponent systems", *Physica A: Statistical Mechanics and its Applications*, vol. 128, no. 1, pp. 334–350, 1984, ISSN: 0378-4371. DOI: https://doi.org/10.1016/0378-4371(84)90096-7. [Online]. Available: https://www.sciencedirect.com/science/article/pii/0378437184900967.

[75] C. Stampfl, H. J. Kreuzer, S. H. Payne, H. Pfnür, and M. Scheffler, "First-principles theory of surface thermodynamics and kinetics", *Phys. Rev. Lett.*, vol. 83, pp. 2993–2996, 15 Oct. 1999. DOI: 10.1103/PhysRevLett.83.2993. [Online]. Available: https://link.aps.org/doi/10.1103/PhysRevLett.83.2993.

[76] K. A. Fichthorn and M. Scheffler, "Island nucleation in thin-film epitaxy: A first-principles investigation", *Phys. Rev. Lett.*, vol. 84, pp. 5371–5374, 23 Jun. 2000. DOI: 10.1103/PhysRevLett.84.5371. [Online]. Available: https://link.aps.org/doi/10.1103/PhysRevLett.84.5371.

[77] Y. Zhang, V. Blum, and K. Reuter, "Accuracy of first-principles lateral interactions: Oxygen at pd(100)", *Phys. Rev. B*, vol. 75, p. 235 406, 23 Jun. 2007. DOI: 10.1103/PhysRevB.75.235406. [Online]. Available: https://link.aps.org/doi/10.1103/PhysRevB.75.235406.

[78] A. Bajpai, K. Frey, and W. F. Schneider, "Binary approach to ternary cluster expansions: No–o–vacancy system on pt(111)", *The Journal of Physical Chemistry C*, vol. 121, no. 13, pp. 7344–7354, 2017. DOI: 10.1021/acs.jpcc.7b00914. eprint: https://doi.org/10.1021/acs.jpcc.7b00914. [Online]. Available: https://doi.org/10.1021/acs.jpcc.7b00914.

[79] C. Wu, D. Schmidt, C. Wolverton, and W. Schneider, "Accurate coverage-dependence incorporated into first-principles kinetic models: Catalytic NO oxidation on Pt (111)", *Journal of Catalysis*, vol. 286, pp. 88–94, 2012, ISSN: 0021-9517. DOI: https://doi.org/10.1016/j.jcat.2011.10.020. [Online]. Available: https://www.sciencedirect.com/science/article/pii/S0021951711003551.

[80] A. J. R. Hensley, G. Collinge, Y. Wang, and J.-S. McEwen, "Coverage-dependent adsorption of hydrogen on fe(100): Determining catalytically relevant surface structures via lattice gas models", *The Journal of Physical Chemistry C*, vol. 124, no. 13, pp. 7254–7266, 2020. DOI: 10.1021/acs.jpcc.9b11945. eprint: https://doi.org/10.1021/acs.jpcc.9b11945. [Online]. Available: https://doi.org/10.1021/acs.jpcc.9b11945.

[81] N. Metropolis, A. W. Rosenbluth, M. N. Rosenbluth, A. H. Teller, and E. Teller, "Equation of state calculations by fast computing machines", *The Journal of Chemical Physics*, vol. 21, no. 6, pp. 1087–1092, 1953. DOI: 10.1063/1.1699114. eprint: https://doi.org/10.1063/1.1699114. [Online]. Available: https://doi.org/10.1063/1.1699114.

[82] W. K. Hastings, "Monte Carlo sampling methods using markov chains and their applications", *Biometrika*, vol. 57, no. 1, pp. 97–109, 1970, ISSN: 00063444. [Online]. Available: http://www.jstor.org/stable/2334940 (visited on 07/12/2022).

[83] D. P. Landau and K. Binder, *A Guide to Monte Carlo Simulations in Statistical Physics*, 5th ed. Cambridge University Press, 2021. DOI: 10.1017/CBO9781139696463.

[84] B. J. Alder and T. E. Wainwright, "Studies in molecular dynamics. i. general method", *The Journal of Chemical Physics*, vol. 31, no. 2, pp. 459–466, 1959. DOI: 10.1063/1.1730376. eprint: https://doi.org/10.1063/1.1730376. [Online]. Available: https://doi.org/10.1063/1.1730376.

[85] "Building the stochastic matrix", in *Markov Chains*. John Wiley Sons, Ltd, 2017, ch. 3, pp. 25–35, ISBN: 9781119387596. DOI: https://doi.org/10.1002/9781119387596.ch3. eprint: https://onlinelibrary.wiley.com/doi/pdf/10.1002/9781119387596.ch3. [Online]. Available: https://onlinelibrary.wiley.com/doi/abs/10.1002/9781119387596.ch3.

Appendix A

(101) Surface Configurations

The structures of the configurations used in constructing the model Hamiltonian, together with comparison between the prediction of DFT and model Hamiltonian are provided in the following. Note than all the colors are in accordance with the figures in the main chapters of the dissertation, where green, red, orange and black correspond to oxygen atom, in-plane vacancy, bridging vacancy and Pd dopant, respectively.

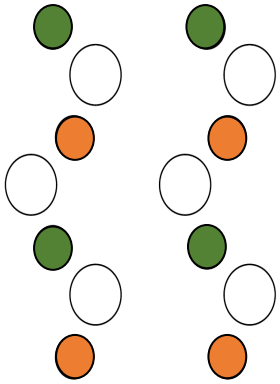

$E_{Model} = 7.396\ eV, \quad E_{DFT} = 7.447\ eV$

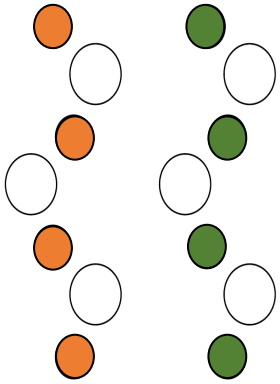

$E_{Model} = 4.562\ eV, \quad E_{DFT} = 4.617\ eV$

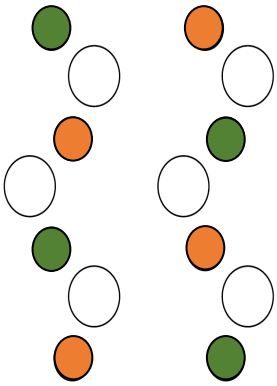

$E_{Model} = 8.534\ eV, \quad E_{DFT} = 8.500\ eV$

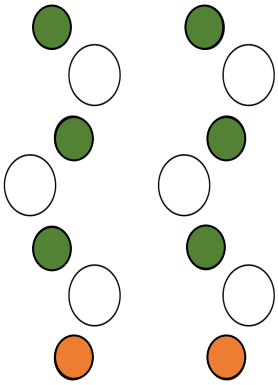

$E_{Model} = 8.088\ eV, \quad E_{DFT} = 8.074\ eV$

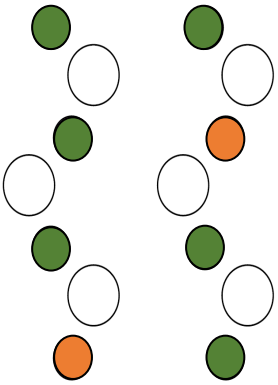

$E_{Model} = 8.296\ eV, \quad E_{DFT} = 8.282\ eV$

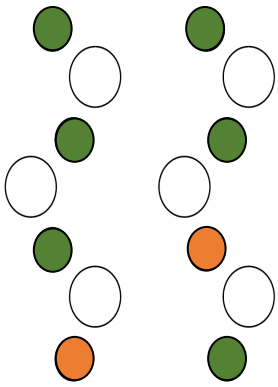

$E_{Model} = 8.760\ eV, \quad E_{DFT} = 8.774\ eV$

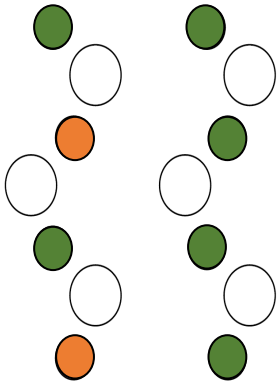

$E_{Model} = 3.265\ eV, \quad E_{DFT} = 3.306\ eV$

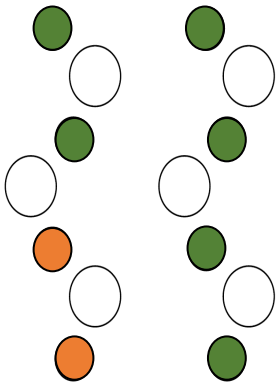

$E_{Model} = 3.090\ eV, \quad E_{DFT} = 3.095\ eV$

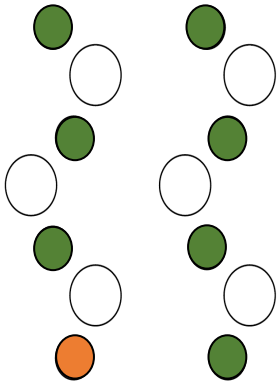

$E_{Model} = 1.940\ eV, \quad E_{DFT} = 1.944\ eV$

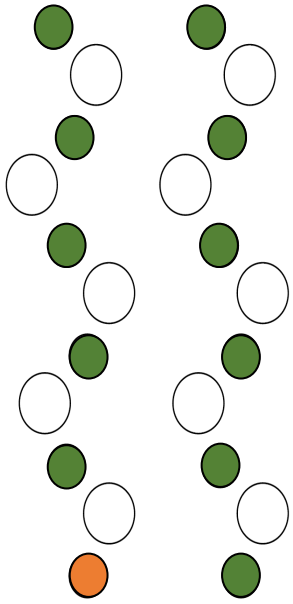

$E_{Model} = 1.939\ eV, \quad E_{DFT} = 1.889\ eV$

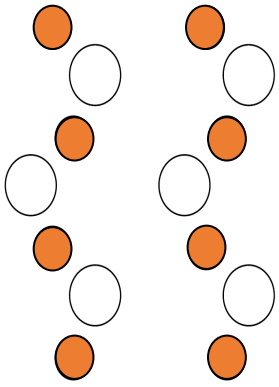

$E_{Model} = 9.874\ eV, \quad E_{DFT} = 9.861\ eV$

Appendix B

(110) Surface Configurations

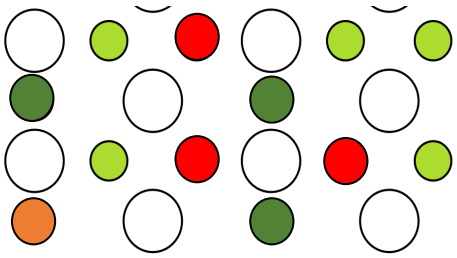

$E_{Model} = 9.816\ eV, \quad E_{DFT} = 9.978\ eV$

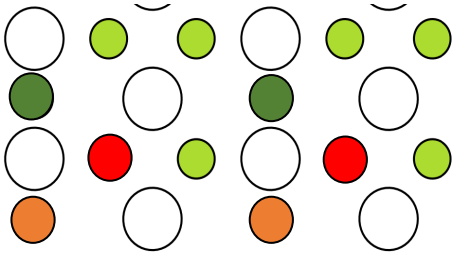

$E_{Model} = 9.963\ eV, \quad E_{DFT} = 10.147\ eV$

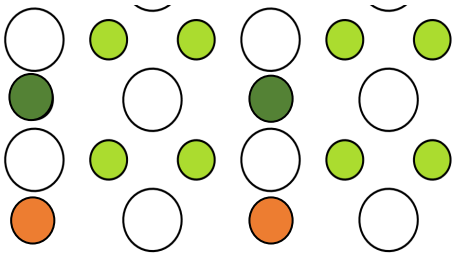

$E_{Model} = 4.802\ eV, \quad E_{DFT} = 4.862\ eV$

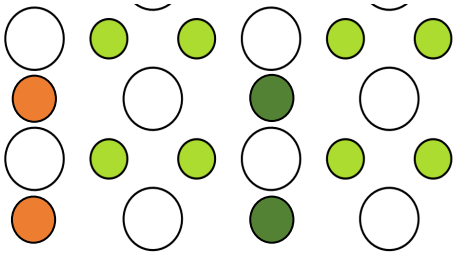

$E_{Model} = 4.492\ eV, \quad E_{DFT} = 4.532\ eV$

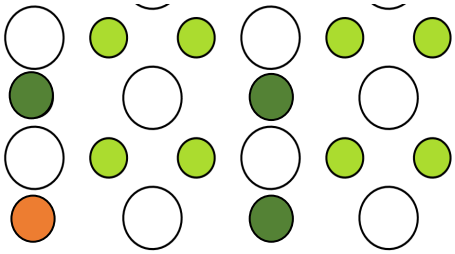

$E_{Model} = 2.401\ eV, \quad E_{DFT} = 2.491\ eV$

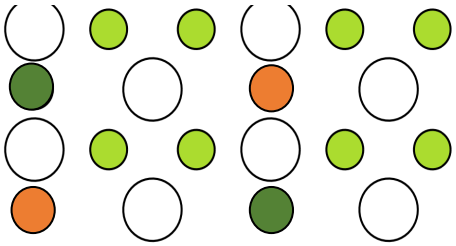

$E_{Model} = 4.803\ eV, \quad E_{DFT} = 4.915\ eV$

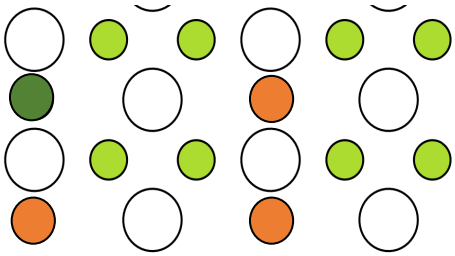

$E_{Model} = 6.894\ eV, \quad E_{DFT} = 6.882\ eV$

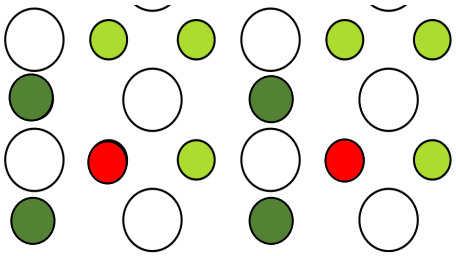

$E_{Model} = 5.772\ eV, \quad E_{DFT} = 5.852\ eV$

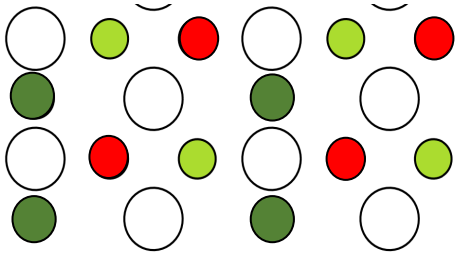

$E_{Model} = 12.802\ eV, \quad E_{DFT} = 12.840\ eV$

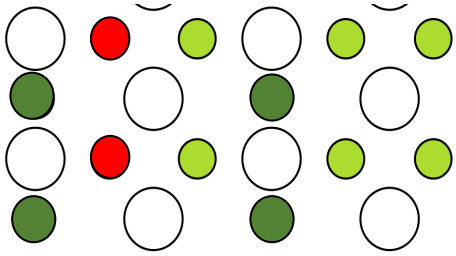

$E_{Model} = 4.785\ eV, \quad E_{DFT} = 4.890\ eV$

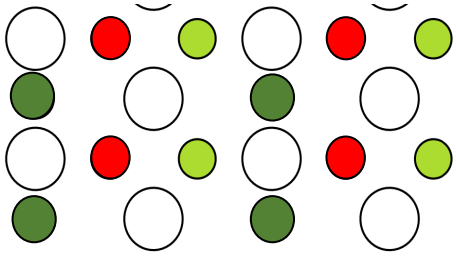

$E_{Model} = 9.391\ eV, \quad E_{DFT} = 9.211\ eV$

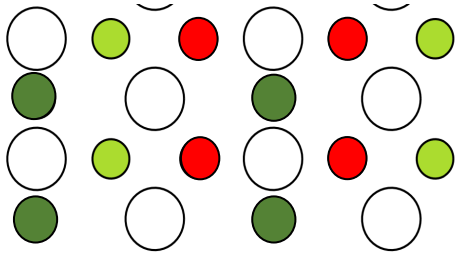

$E_{Model} = 10.339\ eV, \quad E_{DFT} = 10.325\ eV$

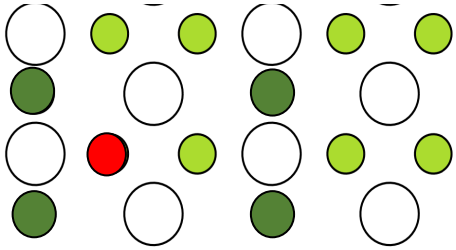

$E_{Model} = 2.932\ eV, \quad E_{DFT} = 3.072\ eV$

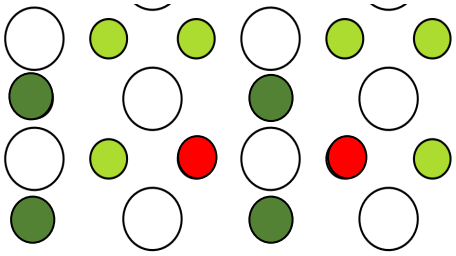

$E_{Model} = 6.165\ eV, \quad E_{DFT} = 6.148\ eV$

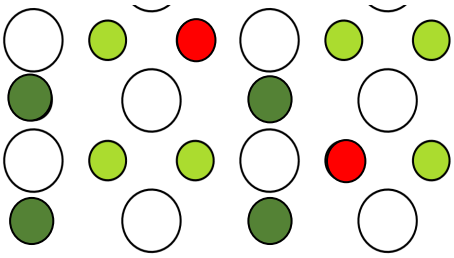

$E_{Model} = 5.949\ eV, \quad E_{DFT} = 6.114\ eV$

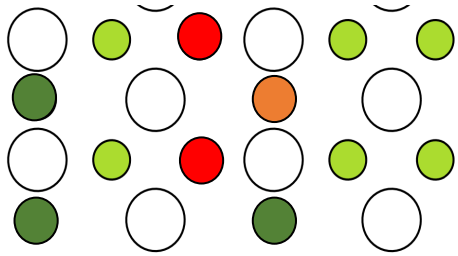

$E_{Model} = 6.857\ eV, \quad E_{DFT} = 7.094\ eV$

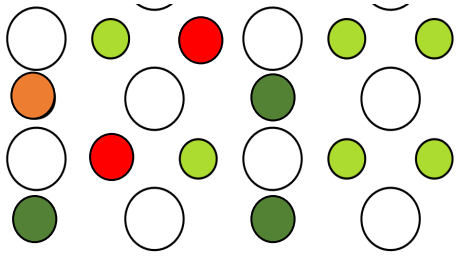

$E_{Model} = 7.629\ eV, \quad E_{DFT} = 7.341\ eV$

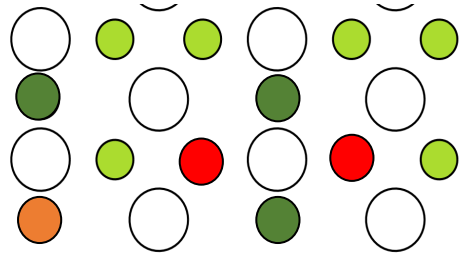

$E_{Model} = 8.356\ eV, \quad E_{DFT} = 8.179\ eV$

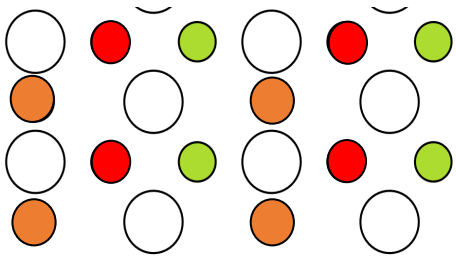

$E_{Model} = 15.430\ eV, \quad E_{DFT} = 15.60\ eV$

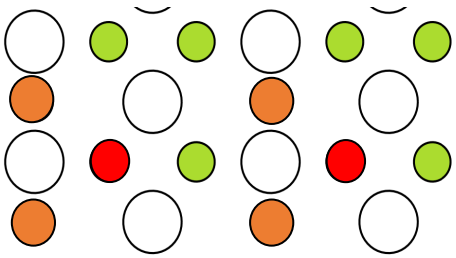

$E_{Model} = 13.386\ eV, \quad E_{DFT} = 13.500\ eV$

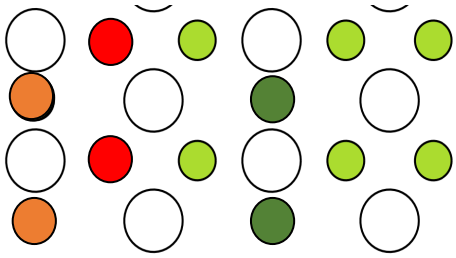

$E_{Model} = 8.134\ eV, \quad E_{DFT} = 7.960\ eV$

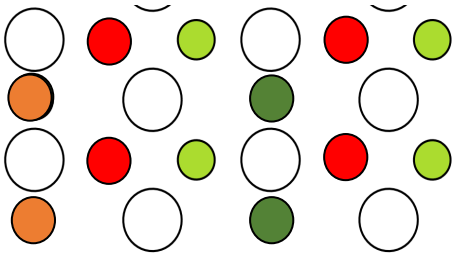

$E_{Model} = 12.410\ eV, \quad E_{DFT} = 12.386\ eV$

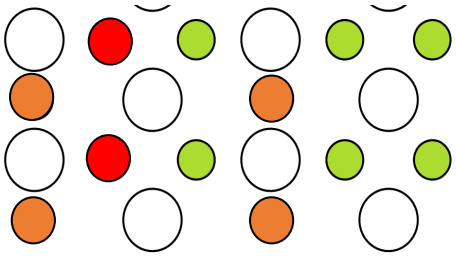

$E_{Model} = 12.297\ eV, \quad E_{DFT} = 12.126\ eV$

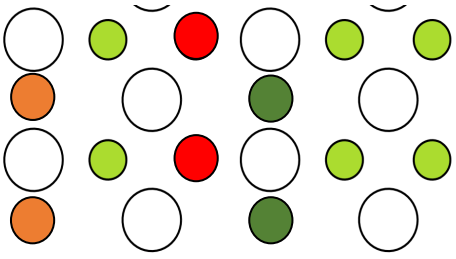

$E_{Model} = 8.949\ eV, \quad E_{DFT} = 8.924\ eV$

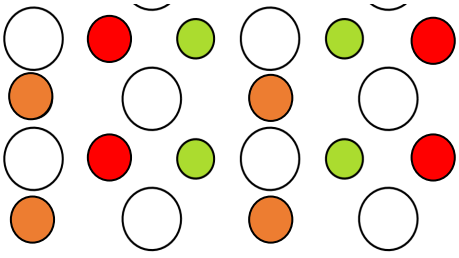

$E_{Model} = 12.543\ eV, \quad E_{DFT} = 12.553\ eV$

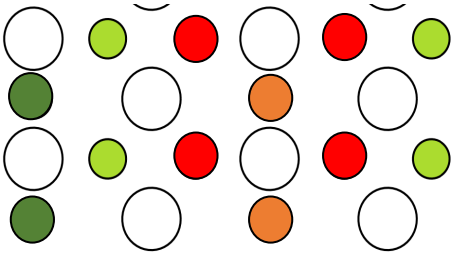

$E_{Model} = 14.174\ eV, \quad E_{DFT} = 14.172\ eV$

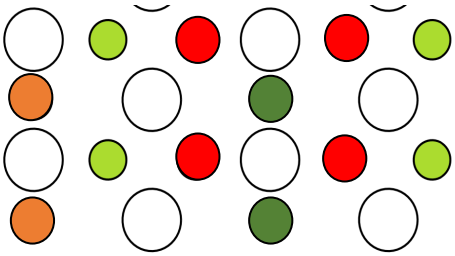

$E_{Model} = 10.547\ eV, \quad E_{DFT} = 10.090\ eV$

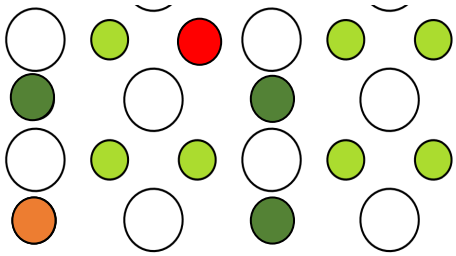

$E_{Model} = 7.078\ eV, \quad E_{DFT} = 7.122\ eV$

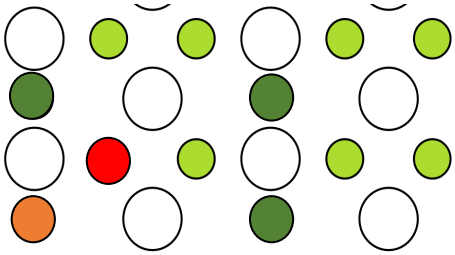

$E_{Model} = 10.608\ eV, \quad E_{DFT} = 10.381\ eV$

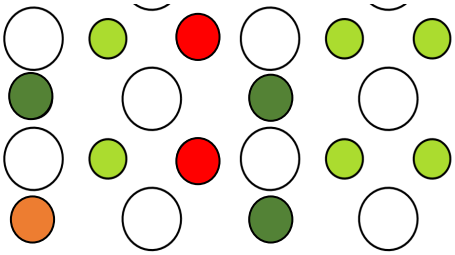

$E_{Model} = 7.078\ eV, \quad E_{DFT} = 7.122\ eV$

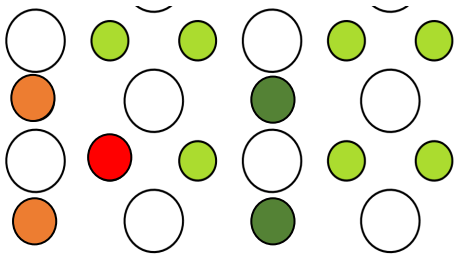

$E_{Model} = 6.852\ eV, \quad E_{DFT} = 6.839\ eV$

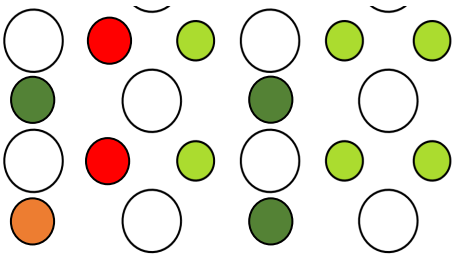

$E_{Model} = 7.068\ eV, \quad E_{DFT} = 7.094\ eV$

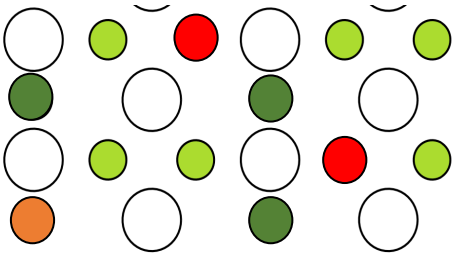

$E_{Model} = 8.053\ eV, \quad E_{DFT} = 8.081\ eV$

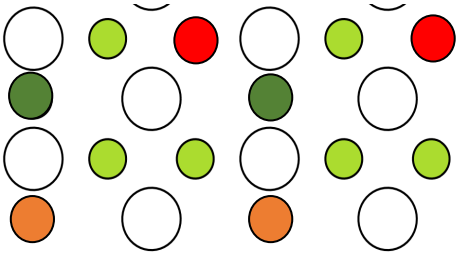

$E_{Model} = 10.218\ eV, \quad E_{DFT} = 9.960\ eV$

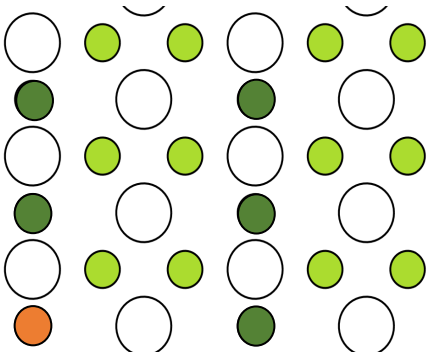

$E_{Model} = 1.929\ eV, \quad E_{DFT} = 1.908\ eV$

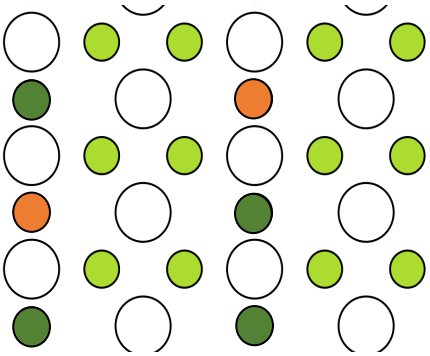

$E_{Model} = 3.858\ eV, \quad E_{DFT} = 3.758\ eV$

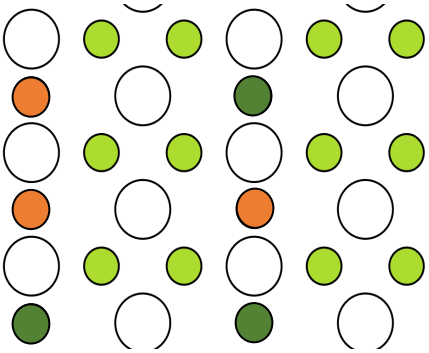

$E_{Model} = 5.690\ eV, \quad E_{DFT} = 5.619\ eV$

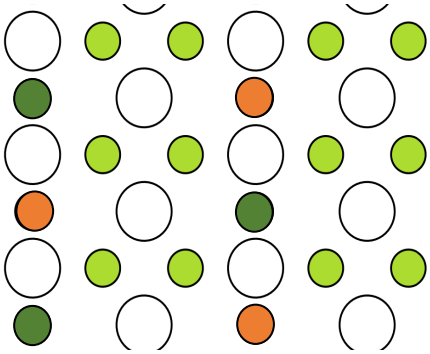

$E_{Model} = 5.690\ eV, \quad E_{DFT} = 5.685\ eV$

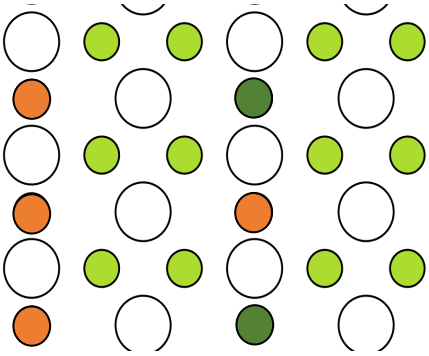

$E_{Model} = 7.423\ eV, \quad E_{DFT} = 7.232\ eV$

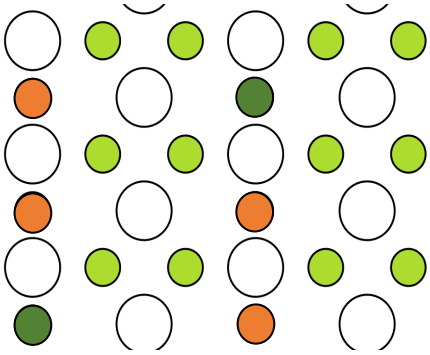

$E_{Model} = 7.521 eV, \quad E_{DFT} = 7.613\ eV$

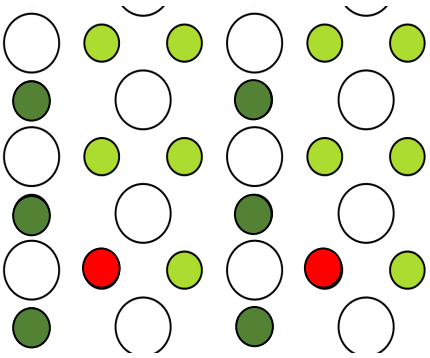

$E_{Model} = 2.886\ eV, \quad E_{DFT} = 2.818\ eV$

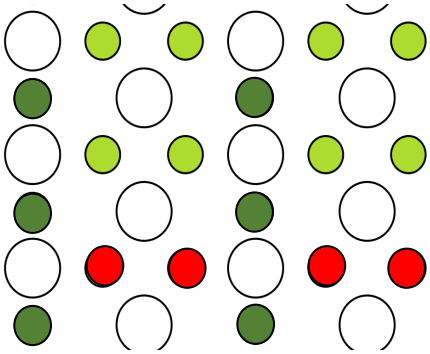

$E_{Model} = 4.589\ eV, \quad E_{DFT} = 4.617\ eV$

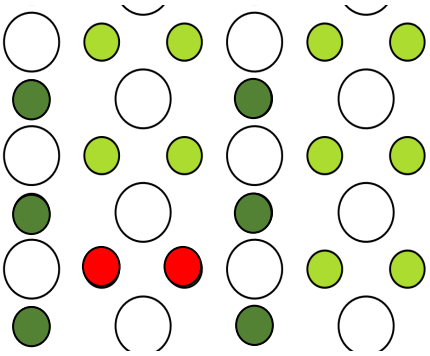

$E_{Model} = 4.025\ eV, \quad E_{DFT} = 3.863\ eV$

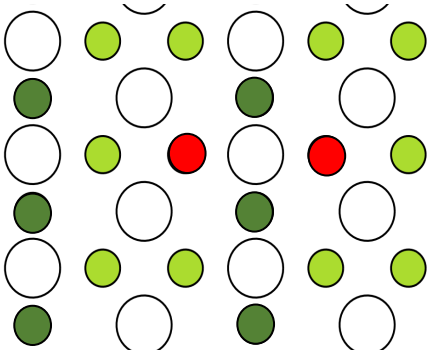

$E_{Model} = 6.247\ eV, \quad E_{DFT} = 6.237\ eV$

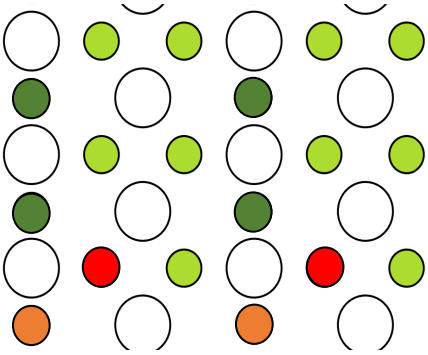

$E_{Model} = 4.069\ eV, \quad E_{DFT} = 4.237\ eV$

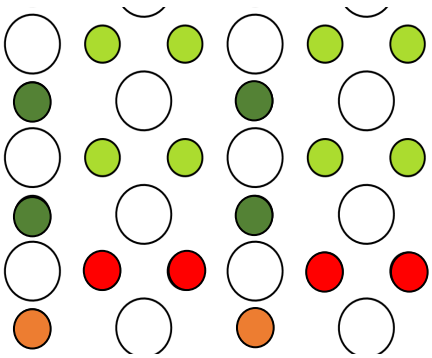

$E_{Model} = 5.545\ eV, \quad E_{DFT} = 5.441\ eV$

Appendix C

(101) Pd-doped surface

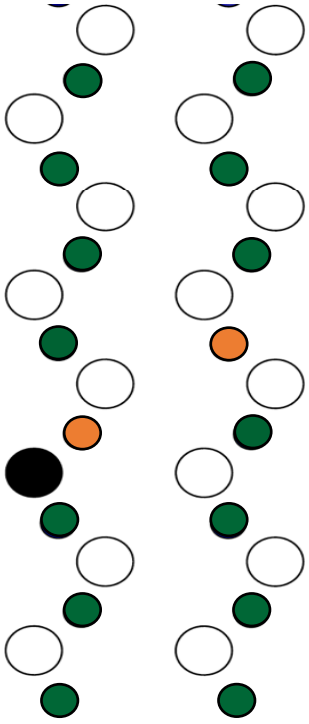

$E_{Model} = 3.639\ eV, \quad E_{DFT} = 3.559\ eV$

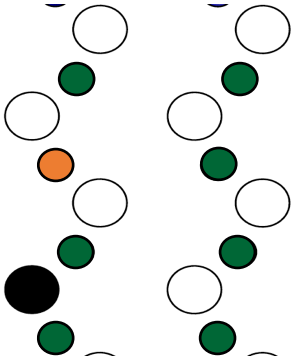

$E_{Model} = 1.930\ eV, \quad E_{DFT} = 1.948\ eV$

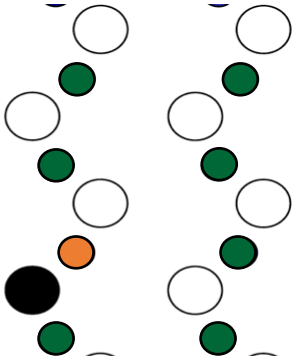

$E_{Model} = 1.442\ eV, \quad E_{DFT} = 1.383\ eV$

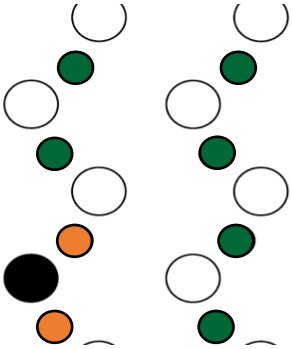

$E_{Model} = 1.576\ eV, \quad E_{DFT} = 1.571\ eV$

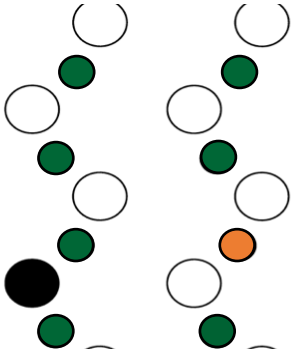

$E_{Model} = 1.930\ eV, \quad E_{DFT} = 1.912\ eV$

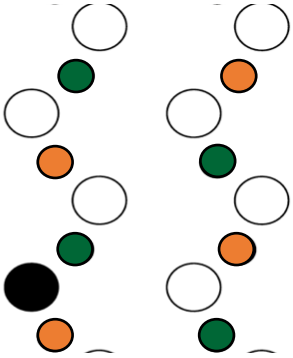

$E_{Model} = 3.490\ eV, \quad E_{DFT} = 3.515\ eV$

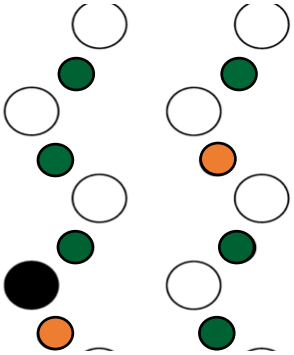

$E_{Model} = 2.598\ eV, \quad E_{DFT} = 2.488\ eV$

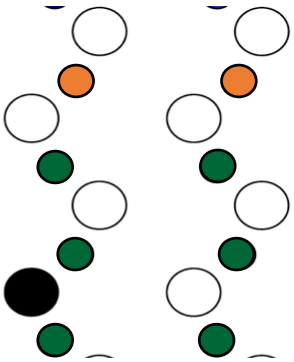

$E_{Model} = 3.539\ eV, \quad E_{DFT} = 3.435\ eV$

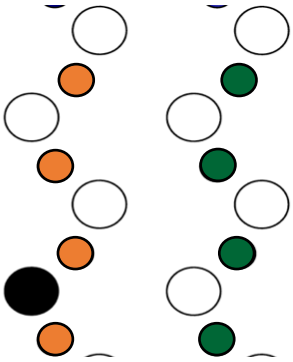

$E_{Model} = 7.275\ eV, \quad E_{DFT} = 7.267\ eV$

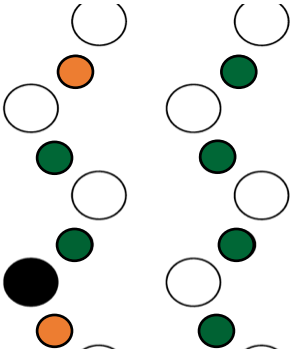

$E_{Model} = 3.283\ eV, \quad E_{DFT} = 3.339\ eV$

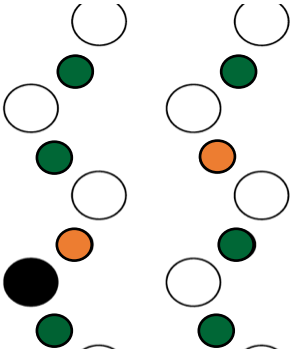

$E_{Model} = 3.215\ eV, \quad E_{DFT} = 3.292\ eV$

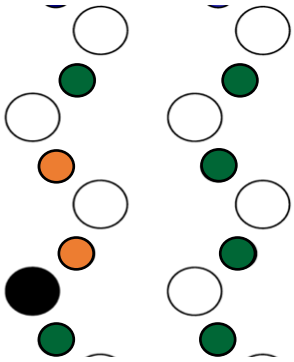

$E_{Model} = 2.598\ eV, \quad E_{DFT} = 2.708\ eV$

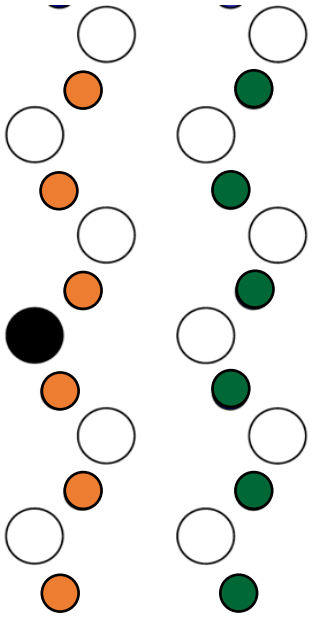

$E_{Model} = 5.550\ eV, \quad E_{DFT} = 5.585\ eV$

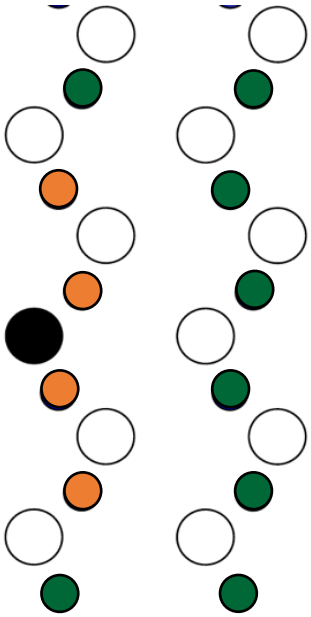

$E_{Model} = 4.102\ eV, \quad E_{DFT} = 3.990\ eV$

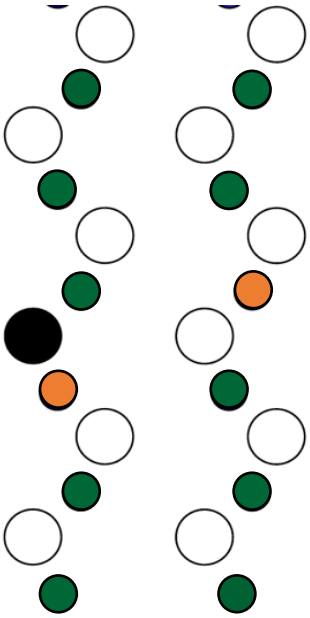

$E_{Model} = 2.417\ eV, \quad E_{DFT} = 2.421\ eV$

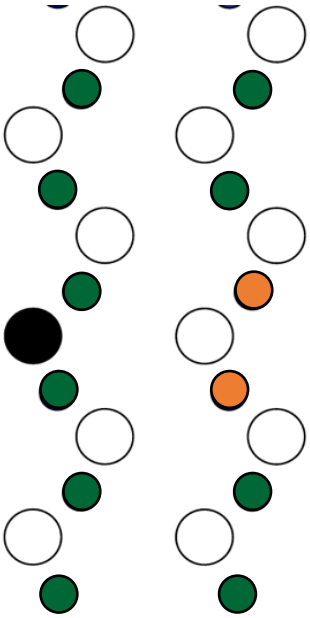

$E_{Model} = 2.912\ eV, \quad E_{DFT} = 2.969\ eV$

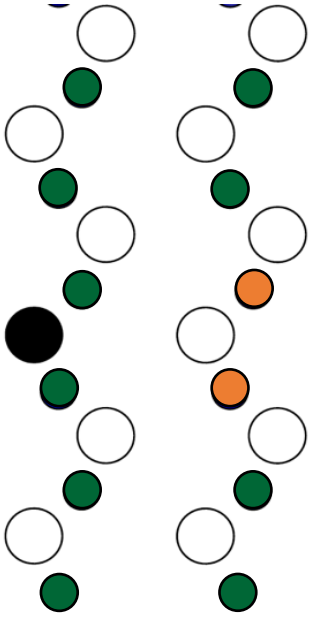

$E_{Model} = 2.912\ eV, \quad E_{DFT} = 2.969\ eV$

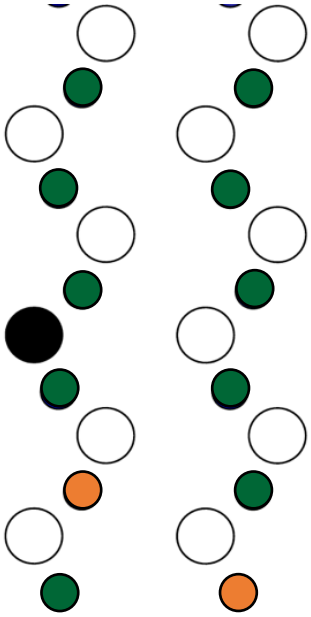

$E_{Model} = 3.858\ eV, \quad E_{DFT} = 3.758\ eV$

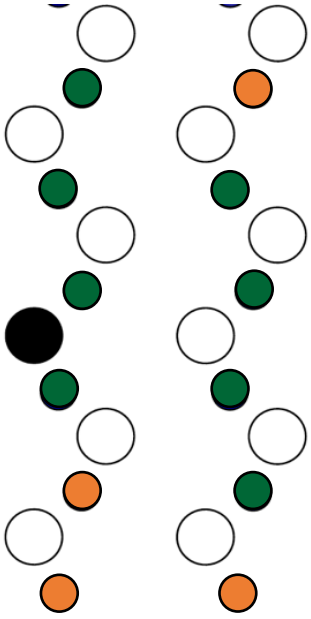

$E_{Model} = 5.690\ eV, \quad E_{DFT} = 5.619\ eV$

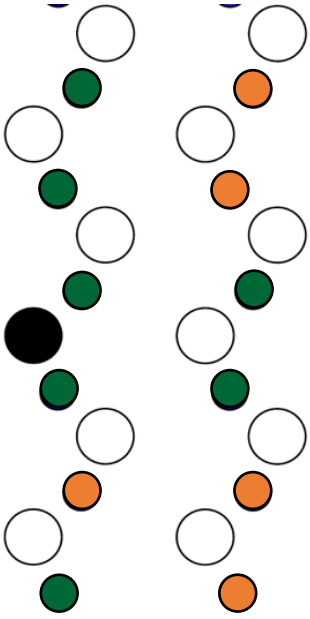

$E_{Model} = 6.060\ eV, \quad E_{DFT} = 6.308\ eV$

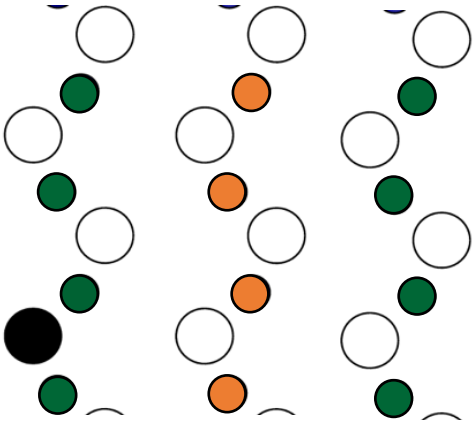

$E_{Model} = 3.490\ eV, \quad E_{DFT} = 3.443\ eV$

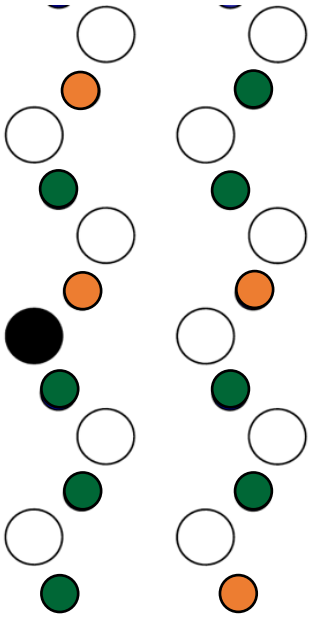

$E_{Model} = 7.638\ eV, \quad E_{DFT} = 7.497\ eV$

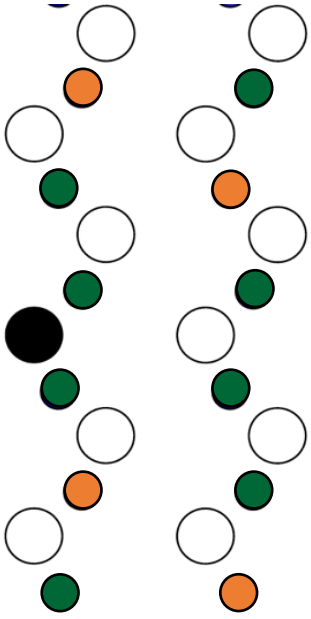

$E_{Model} = 8.081\ eV, \quad E_{DFT} = 7.843\ eV$

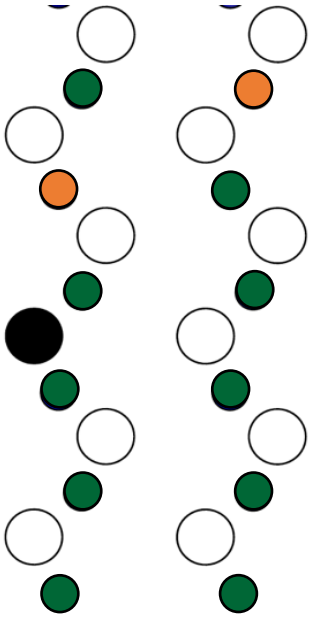

$E_{Model} = 3.940\ eV, \quad E_{DFT} = 4.016\ eV$

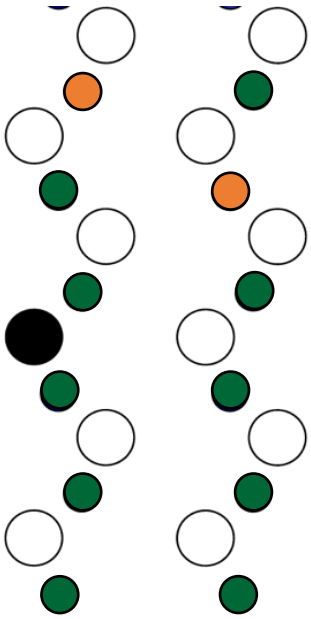

$E_{Model} = 4.130\ eV, \quad E_{DFT} = 4.161\ eV$

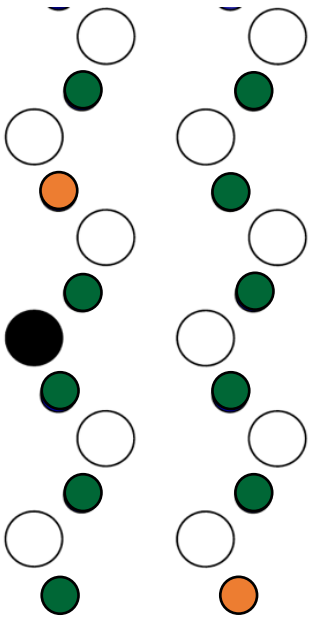

$E_{Model} = 3.858\ eV, \quad E_{DFT} = 3.758\ eV$

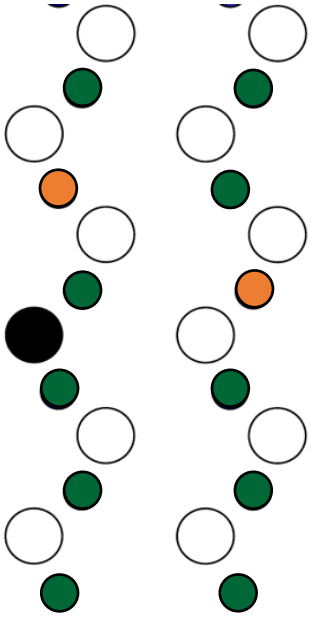

$E_{Model} = 4.101\ eV, \quad E_{DFT} = 4.112\ eV$

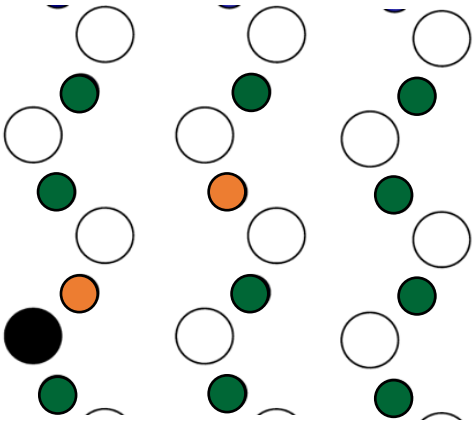

$E_{Model} = 4.514\ eV, \quad E_{DFT} = 4.431\ eV$